Project No. 10-905

Heat Transfer Salts for Nuclear Reactor Systems – Chemistry Control, Corrosion Mitigation, and Modeling

Reactor Concepts RD&D

Dr. Mark Anderson
University of Wisconsin, Madison

In collaboration with:
Pacific Northwest National Laboratory
University of California, Berkeley

Brian Robinson, Federal POC
Michael McKellar, Technical POC

NEUP Nuclear Energy University Programs
U.S. Department of Energy

Heat Transfer Salts for Nuclear Reactor Systems - chemistry control, corrosion mitigation and modeling
CFP-10-100

Dr. Mark Anderson, Dr. Kumar Sridharan, Dr. Dane Morgan , Dr. Per Peterson, Dr. Pattrick Calderoni, Mr. Randall Scheele , Dr. Andrew Casella, Dr. Bruce McNamara, Brian Kelleher , Robert Sellers, Tony (Guiqiu) Zheng, Tommy Cisneros, Oday Albakri, Nick Kuwahara, Jun Yang, Maxwell Strassman, Arjun Kalra, William Ryan, David Pfotenhauer, Brad Motl, Paul Brooks

UNIVERSITY OF WISCONSIN-MADISON, UNIVERSITY OF CALIFORNIA - BERKELEY, PACIFIC NORTHWEST NATIONAL LABORATORY

Executive Summary

The concept of a molten salt reactor has existed for nearly sixty years. Previously all work was done during a large collaborative effort at Oak Ridge National Laboratory, culminating in a research reactor which operated for 15,000 hours without major error. This technical success has garnished interest in modern, high temperature, reactor schemes.

Research using molten fluoride salts for nuclear applications requires a steady supply of high grade molten salts. There is no bulk supplier of research grade fluoride salts in the world, so a facility which could provide all the salt needed for testing at the University of Wisconsin had to be produced. Two salt purification devices were made for this purpose, a large scale purifier, and a small scale purifier, each designed to clean the salts from impurities and reduce their corrosion potential. As of now, the small scale has performed with flibe salt, hydrogen, and hydrogen fluoride, yielding clean salt. This salt is currently being used in corrosion testing facilities at the Massachusetts Institute of Technology and the University of Wisconsin.

Working with the beryllium based salts requires extensive safety measures and health monitoring to prevent the development of acute or chronic beryllium disease, two pulmonary diseases created by an allergic reaction to beryllium in the lungs. Extensive health monitoring, engineering controls, and environment monitoring had to be set up with the University of Wisconsin department of Environment, Health and Safety. The hydrogen fluoride required for purification was also an extreme health hazard requiring thoughtful planning and execution. These dangers have made research a slow and tedious process. Simple processes, such as chemical handling and clean-up can take large amounts of ingenuity and time.

Other work has complemented the experimental research at Wisconsin to advance high temperature reactor goals. Modeling work has been performed in house to re-evaluate thermophysical properties of flibe and flinak. Pacific Northwest National Laboratories has focused on evaluating the fluorinating gas nitrogen trifluoride as a potential salt purification agent. Work there was performed on removing hydroxides and oxides from flinak salt under controlled conditions. Lastly, the University of California Berkeley has spent considerable time designing and simulating reactor components with fluoride salts at high temperatures.

Despite the hurdles presented by the innate chemical hazards, considerable progress has been made. The stage has been set to perform new research on salt chemical control which could advance the fluoride salt cooled reactor concept towards commercialization. What were previously thought of as chemical undesirable, but nuclear certified, alloys have been shown to be theoretically compatible with fluoride salts at high temperatures. This preliminary report has been prepared to communicate the construction of the basic infrastructure required for flibe, as well as suggest original research to performed at the University of Wisconsin. Simultaneously, the contents of this report can serve as a detailed, but introductory guide to allow anyone to learn the fundamentals of chemistry, engineering, and safety required to work with flibe salt.

Table of Contents

List of Tables

List of Figures

Chapter 1

Molten Fluoride Salts for Nuclear Power

1.1 History and Applications of Molten Salts

Molten salts have found uses in a wide variety of industrial processes due to their unique characteristics at high temperatures. In 1886 Charles Martin Hall and Paul Heroult independently discovered that alumina (Al_2O_3) could be dissolved into molten Na_3AlF_6 salt. This salt and alumina mixture could be electrolyzed at a manageable temperature of around 1000°C, instead of alumina's melting point of 2072°C. The Hall-Heroult process, which is still used today, allowed the first commercial production of aluminum metal—now the most widely used non-ferrous metal.

During the 1920's molten salt heat baths became a widely accepted way to treat tools and automotive parts. Using both nitrate based and chloride based salts, these baths are able to harden, carburize, quench, and clean steels uniformly, quickly, without cracking or surface oxidation. Typical quench temperatures are between 150-595°C.

The onset of The Cold War prompted the United States to pursue long range bombers which could fly uninterrupted for several days or weeks using only nuclear power. The project, called the Aircraft Reactor Experiment (ARE), was taken by Oak Ridge National Laboratory (ORNL). The on-board reactor was required to operate at temperatures of 870°C to provide superheated gas for the turbines which would generate thrust [1]. It was feared that the narrow fuel elements necessary for the ARE would not maintain their structural integrity at these temperatures [2]. To bypass this problem, Ed Bettis and Ray Briant of Oak Ridge National Laboratory proposed to dissolve the fissile material into a liquid coolant, thus avoiding traditional, solid, metal clad ceramic fuel [1].

Molten fluoride salts of the alkali metals and alkaline earths were found to be suitable liquid coolants due to their stability at high temperatures and radiation fluxes coupled with high solu-

Figure 1.1: The two of the experimental reactors used for the ARE. The Heat Transfer Reactor Experiment 1 (HTRE-1) is on the right, the HTRE-3 on the left.

bility of uranium tetrafluoride fuel in this environment. However, molten fluorides were found to be corrosive to many types of common structural alloys [3]. To prevent corrosion, the nickel-molybdenum based alloy Hastelloy-N, which is now owned by Haynes International Inc, was created for use in the ARE [4]. This alloy's chemical composition rendered it inert to the salts corrosion pathways. Additionally, the salt was chemically controlled, lowering corrosion rates even further. Chemical control was achieved by sparging, or bubbling, anhydrous hydrogen fluoride and hydrogen gas through the liquid salt to remove oxide, metallic, and uranic corrosion agents [5]. The success of both active and passive corrosion control techniques allowed three reactors, the Heat Transfer Reactor Experiment 1 (HTRE-1), HTRE-2, and HTRE-3, to operate continuously using a mixture of NaF-ZrF_4-UF_4 at 2,500 kW for 100 hours at a peak temperature of 870°C. Two of these reactors are shown in figure 1.1.

1.2 The Molten Salt Reactor Experiment

As the United States intercontinental ballistic missile program continued to progress, the feasibility of a flying nuclear reactor was questioned. The heavy lead shielding required to protect pilots from reactor's radiation was a constant problem. Additionally, there were always worries about

an unexpected crash and the resultant contamination. These difficulties caused the program to be scrapped [2]. However, Alvin Weinberg suggested that the ARE technology be used to construct a civilian power reactor. Following a review from a Atomic Energy Commission Task Force it was determined that the Molten Salt Reactor concept had the highest probability of achieving technical feasibility and was given funding [6].

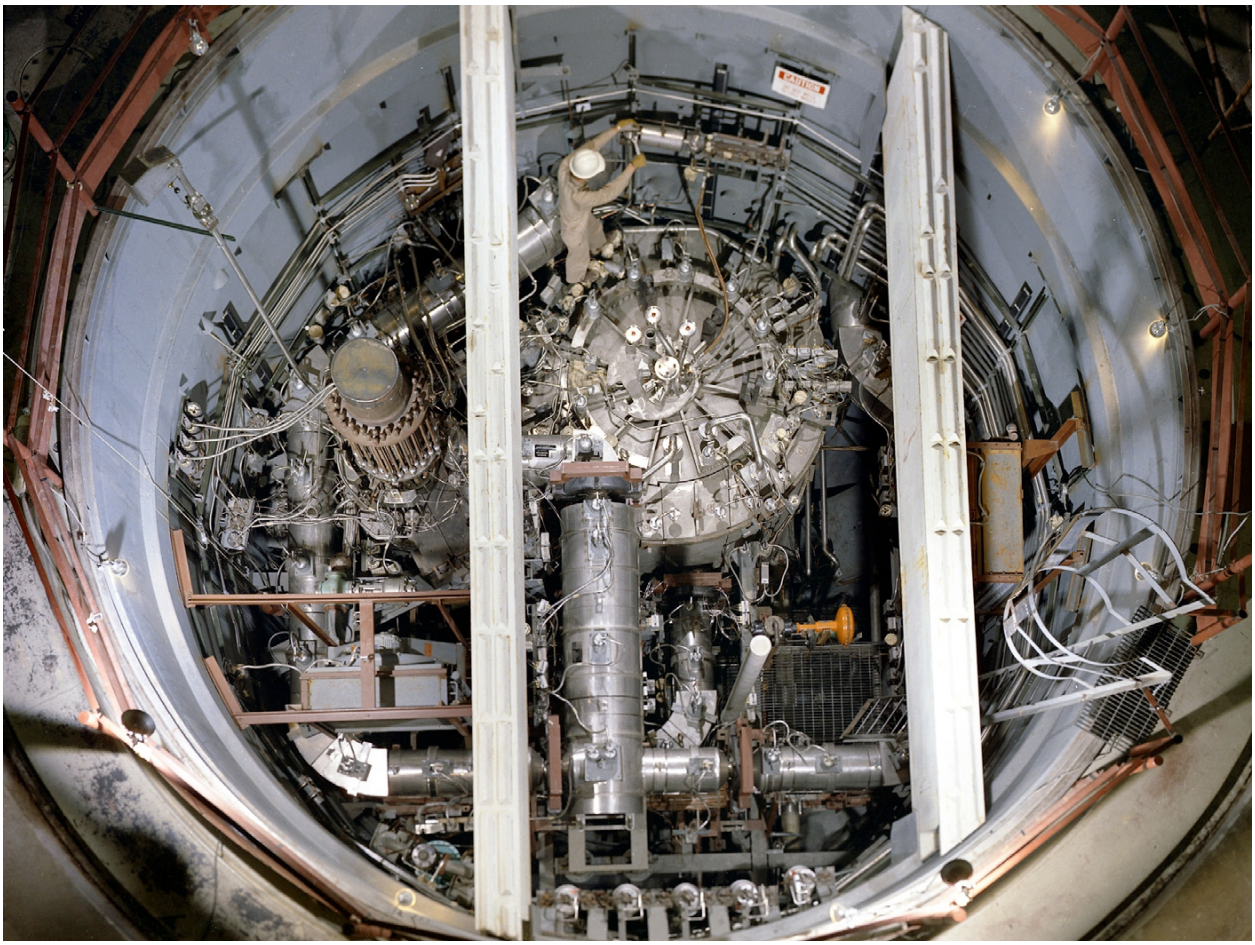

Figure 1.2: A top down view of the molten salt reactor experiment.

Design and construction of 8 MW_{th}, prototype civilian nuclear power plant, deemed the Molten Salt Reactor Experiment (MSRE), began in 1960 and criticality was achieved in 1965 [1]. The MSRE ran critical for 15,424 hours without any major issues. The reactor used a fuel-coolant salt mixture, referred to just as fuel salt, of LiF-BeF_2 (flibe), ZrF_4, and UF_4 circulating at temperatures

of around 650°C [7, 8]. The fuel salt flowed throughout the reactor components, and only became critical in a multi-channel graphite core [7]. Heat was exchanged with a fuel-less salt, also known as coolant salt, loop which was then was cooled by air.

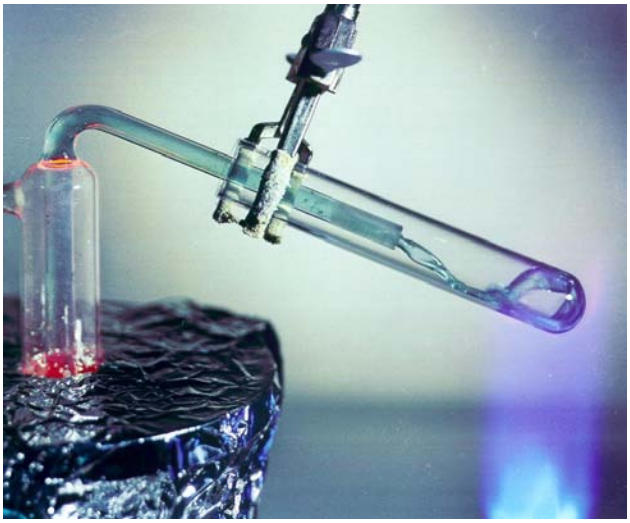

Figure 1.3: Molten flibe flowing through glass tubing. The blueish tint is from dissolved UF_4 which is naturally green in color.

One of the most unique operations during the reactor's operation was the removal of all the the $^{235}UF_4$ from the fuel salt. Over four days, gaseous fluorine was sparged through the molten fuel salt, converting all UF_4 into the volatile fluoride UF_6 which then bubbled out of the salt and was reclaimed [1]. After this, $^{233}UF_4$ was dissolved into the reactor which was then restarted by the discoverer of ^{233}U, Glenn Seaborg [1]. The use of $^{233}UF_4$ fuel demonstrated the ability of the reactor to run on $^{232}ThF_4$ which could be bred into $^{233}UF_4$ during nuclear operations.

After the demonstration of the breeder concept, effort was put towards designing a molten salt breeder reactor. Unfortunately, the project slowly tapered off until 1978 as funding was diverted to the liquid metal breeder reactor program, which had been in progress for several years prior to the MSRE [1, 2].

1.3 Generation IV Systems: The Fluoride Salt Cooled High Temperature Reactor

Recently, work on the generation IV nuclear power plants has revitalized interest in molten fluoride salts as a nuclear reactor coolant [9]. The generation IV initiative was created to analyze each high temperature reactor type, determining its ability to be commercialized, investigate any large gaps in research, and most importantly, estimate its maximum operating temperature. Operating temperature is one of the most decisive factors in economics; a higher temperature reactor can produce energy more efficiently than a lower temperature reactor. Pressurized water cooled reactors currently operate around 315°C, with pressure limits severely retarding improvements in this number [10]. To improve on the current reactor fleet, a new coolant is needed which will not experience this problem. This heat transfer fluid will have to be chemically and radiolytically stable at temperatures of around 800°C, have a low melting point and high boiling point, large specific heat and thermal conductivity, a lower vapor pressure than that of water, and be compatible with high temperature alloys [11].

Table 1.1: Advanced nuclear reactor heat transfer fluid properties. The salts are LiF-NaF-KF (46.5-11.5-42 mol%) and LiF-BeF_2 (66-34 mol%) by composition [12].

Fluid	Melting Point (K)	Boiling Point (K)	Density (kg m^{-3})	Specific Heat Capacity (J kg^{-1} K^{-1})	Viscosity (Pa s)	Thermal Conductivity (W m^{-1} K^{-1})	ρc_P (J m^{-3} K^{-1})
LiF-BeF_2	733	1703	1940	2414	5.6×10^{-3}	1	4.68×10^{6}
LiF-NaF-KF	727	1843	2020	1883	2.9×10^{-3}	0.92	3.80×10^{6}
H_2O	273	100	1000	4184	1.0×10^{-3}	0.6	4.18×10^{6}
He (7.5MPa)	-	373	3.8	5505	4.2×10^{-5}	0.29	2.09×10^{4}
Na	370.8	1156	820	1230	2.3×10^{-4}	62	1.01×10^{6}

As shown in Table 1.1, no ideal fluid exists for the job. Helium, although chemically inert, would have to be pressurized to raise its volumetric heat capacity within two orders of magnitude within other proposed fluids. Water has a very high volumetric heat capacity, but it would have to have to be pressurized beyond the current 2250 PSI to obtain the temperatures required [10].

Sodium has been used in a handful of reactors successfully, has half the melting boil of salts and low vapor pressure, but is chemically reactive with water vapor and oxygen in the atmosphere. Salts have been shown to have great high temperature stability, high volumetric heat capacity, but their melting point is higher than other candidates, and their chemical compatibility with alloys at high temperature is of concern. Determining which one of these heat transfer fluids can most easily be used in a commercial plant is not straight forward. It was proposed that salts be used to exchanged heat with the primary coolant, using their heat to produce hydrogen, in a next generation power plant [13].

Another nuclear proposal for molten salts, called the Fluoride Salt-Cooled High-Temperature Reactor (FHR), has been conceptualized [14, 15]. The FHR design is a joint initiative by the Massachusetts Institute of Technology (MIT), University of California - Berkeley (UCB) and the University of Wisconsin - Madison (UW). The design combines passively safe pool-type reactor designs, Brayton power cycles, high temperature coated particle fuel (TRISO), and molten salt coolant. It offers several advantages to current next generation nuclear power designs such as: failure temperatures approaching 1600°C, smaller plumbing diameters, heat conduction to ground during beyond design basis accidents, and a high outlet temperature for process heat [16]. However, no molten salt nuclear power plant has ever been constructed with just salt; all new control techniques would be needed to designed and tested.

Chapter 2

Fluoride Salt Properties and Chemistry

2.1 Selection of Salt for Reactor Use

Many combinations of salts were tested throughout the aircraft reactor experiment and the molten salt reactor experiment to find the best salt for use in a reactor [17]. Salts were studied on their melting point, heat transfer properties, fuel solubility, vapor pressure, viscosity, nuclear stability, and chemical compatibility with nickel based alloys at high temperature [18, 19]. It was found that of all the fluorides, combinations the alkalis, beryllium, and zirconium offered some of the best properties [20]. Out of these LiF, BeF_2, and NaF had the lowest melting points [18]. From this group, BeF_2 had the lowest neutron cross section and was selected as part of the base [18]. In fact, BeF_2 was investigated as a lone coolant with a melting point of 554°C, but was found too viscous [19]. It was obvious that salt needed better flow characteristics. In order to achieve these low viscosities, enriched ^{7}LiF was selected [21]. To create good neutronic properties the natural lithium in the LiF would have to be enriched from 92.5% ^{7}Li to 99.99%. With these properties in mind, the binary system LiF-BeF_2 was found to have the most suitable properties for a fluoride salt cooled nuclear reactor [19]. It was used as the fuel carrier, coolant salt, and the flush salt for cleaning reactor components and piping before operations [8]. A detailed evaluation of salts for reactor use is given by Williams et al. in "Assessment of Candidate Molten Salt Coolants for the Advanced High-Temperature Reactor".

2.2 Assorted Thermophysical Properties of Flibe

The melting point of a fluoride salt depends greatly on its components and its mixtures. Shown in Figure 2.1, the LiF-BeF_2 system as pure LiF yields a melting point of 845°C. Adding around 33

mol % of BeF_2 brings the salt to the commonly used off eutectic at 459°C. The addition of more BeF_2 drops the melting point until the eutectic point at 356°C. Upon further addition of BeF_2 the melting point climbs until it reaches 554°C, the melting point of BeF_2.

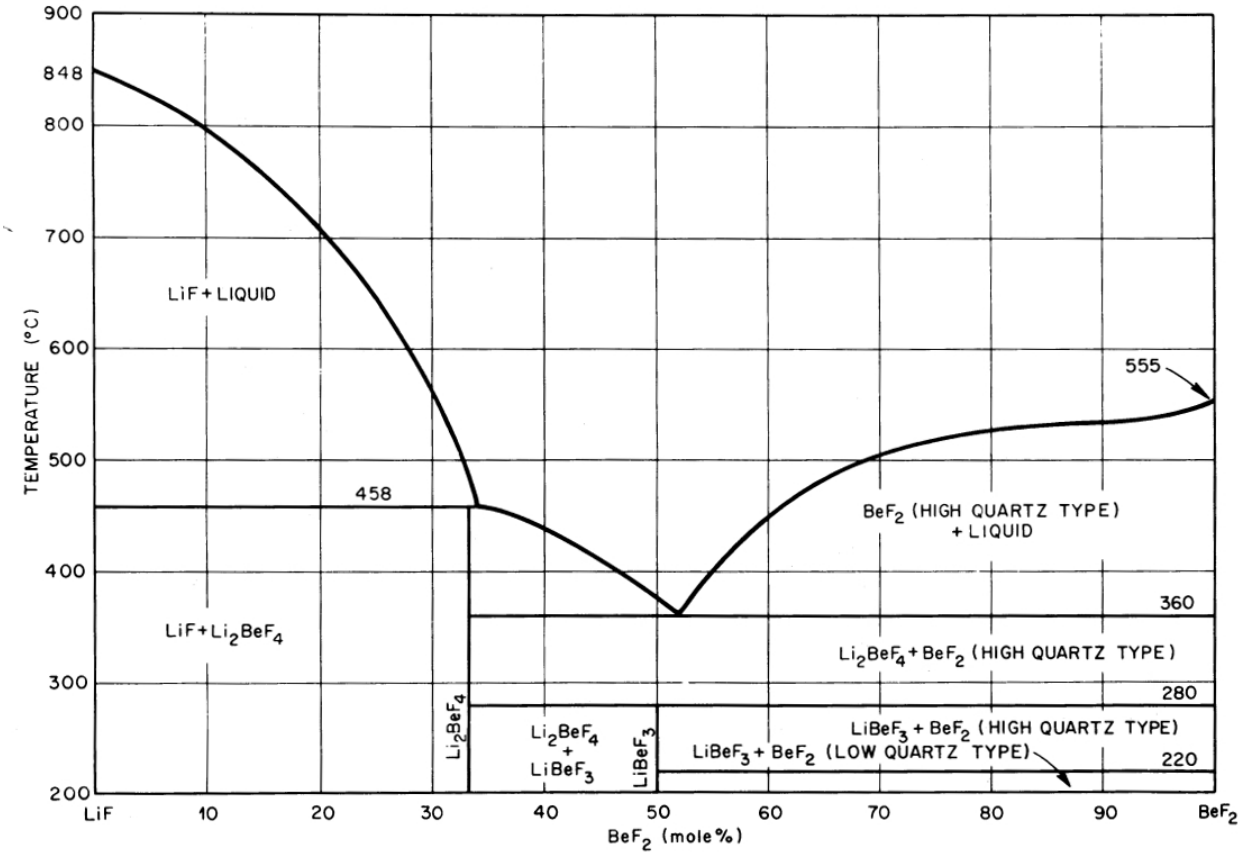

Figure 2.1: The system LiF-BeF_2 [18].

Viscosities are highly dependent on the BeF_2 concentration, as shown in Figure 2.2, due to the bridging of beryllium and fluorine ions as Be-F-Be chains [22, 23]. At the point of 69 mole% LiF, 31 mole% BeF_2 the mixture has a viscosity of 7.5×10^{-3} Pa s at 600°C but has a melting point of 505°C, roughly 150°C higher than the eutectic [18]. On the other hand, a composition closer to the eutectic point can be picked such as 50 mole% LiF, 50 mole% BeF_2 with a melting point of 356°C [18]. Unfortunately, this composition has a viscosity of 22.2×10^{-3} Pa s at 600°C, nearly three times that of the previous mixture. The off-eutectic of 66 mole% LiF, 34 mole% BeF_2 or

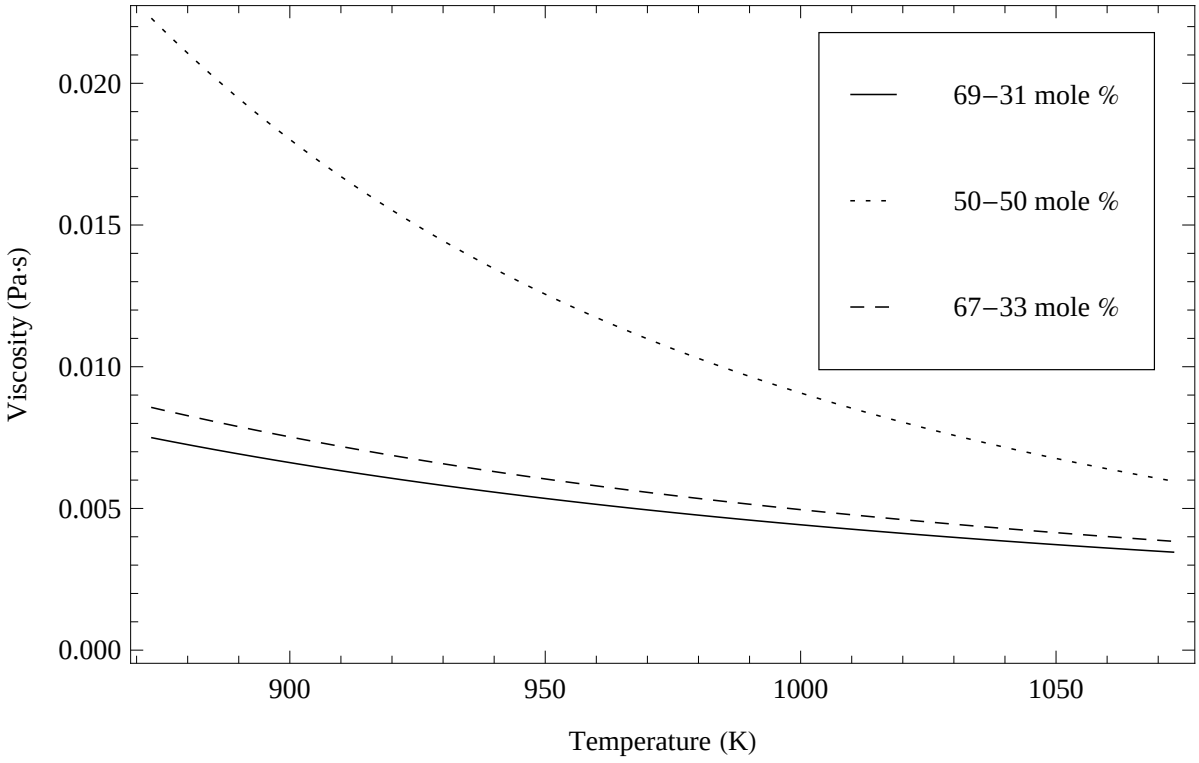

Figure 2.2: Viscosities of three LiF-BeF_2 compositions.

Li_2BeF_4 was eventually chosen as a compromise with a melting point of 459°C and a viscosity of 8.6×10^{-3} Pa s.

The mixture LiF-BeF_2 also has decent vapor pressure properties, ranging from around 1 mmHg at 20 mol % BeF_2 to 10 mm Hg at 100 mol % BeF_2 [17]. Only at temperatures greater than 1000°C do pressures climb to around an atmosphere [17]. Despite low vapor pressures, a purge gas must be kept flowing to prevent excessive accumulation on surfaces [17]. A 5 psig helium cover was used at the MSRE, with 40 psig planned for a next generation molten salt reactor [17]. Other salts, such as ZrF_4 containing salts, can have large problems with vapor pressures. Zirconium tetrafluoride sublimes at around 600°C, which can cause huge problems in a molten system [17]. A alkali fluoride is required to donate fluorine ions to it in order for it to stop this behavior. Even after being complexed by fluorine ions, ZrF_4 containing salts tend to have large vapor pressures which must be dealt with accordingly. In the ARE, which used NaF-ZrF_4 carrier salt, white ZrF_4

was found above the liquid salt in large quantities. To get rid of the deposits, or snow, traps were designed to stop this vapor from depositing on surfaces. Unlike BeF_2, these deposits can't be melted back into the salt–trying to do so would sublime them again, causing deposition on other surfaces.

2.3 Thermodynamics and Corrosion Mechanisms of Fluoride Salts

Corrosion of alloys by molten fluoride salts is fundamentally different than corrosion caused by high temperature air or water oxidation [22, 24]. Many standard alloys rely on the oxygen in air and in water to create a stable CrO, NiO, or Al_2O_3 protective film on the surface of the metal. Even, metals in the presence of gaseous fluorine compounds can make a passivated fluoride layer composed of CuF_2, FeF_2, or NiF_2. However, these oxide and fluoride layers are soluble in fluoride based salts and will readily dissolve exposing fresh metal. These freshly exposed metals can be corroded in a variety of ways, but the corrosion ultimately dominated by thermodynamics and dissolution kinetics.

2.3.1 Lewis Acid and Base Chemistry, Salt Stability, and Pure Salt Chemistry

To examine the thermodynamic behavior of molten salts, the basic salt components must be analyzed first. As alkali fluoride salts are melted, the thermal energy of each atom is high enough to overcome the coulomb forces holding the atoms together. This allows salts to disassociate into ions. For example, LiF forms into

$$LiF \rightarrow Li^+ + F^- \tag{2.1}$$

at its melting point. Once the salt's ions are free to move, the salt becomes a conductor of electricity. Other salts, such as BeF_2 and ZrF_4 do not behave this way [22, 25]. For instance, molten

BeF_2 is non-ionic, despite the fact that the Be—F bond is considered largely ionic. Upon melting it forms glassy networks of chained Be and F atoms [25]. This fact is the ultimate cause of the BeF_2 high viscosity. The high vapor pressure of ZrF_4 is also related to its non-ionic melting. These physical properties were altered through the use of Lewis acid and base chemistry.

A Lewis acid is simply a substance which can accept lone electrons from a Lewis base, thus creating an electron pair. An example of a Lewis acid is the molecule BeF_2. Examining its dot diagram

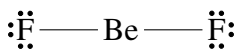

it can be seen that although both fluorine atoms are satisfying the octet rule, the beryllium atom only has two pairs of electrons. To satisfy the octet rule it needs two more pairs. At standard temperatures there would be no way for it to receive more fluorine atoms. However, in the presence of molten lithium fluoride, or another alkali fluoride, it can receive two extra fluorines in the reaction

$$BeF_2 + 2Li^+ + 2F^- \rightarrow BeF_4^{-2} + 2Li^+. \tag{2.2}$$

In terms of a dot diagram this appears as

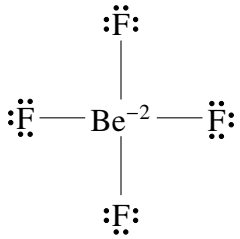

During this reaction the beryllium completes an octet through the Lewis base F^-, but at the same time becomes an ion. Through the BeF_4^{-2} ion formation the glassy BeF_2 network can be broken, thus decreasing the viscosity. Thus it comes at no surprise that the mixture LiF-BeF_2 (66-34 mol%) has the lowest viscosity per mole BeF_2 as all BeF_2 are in the form of BeF_4^{-2}. Additionally, completion of octets on all atoms makes a more stable compound, resulting in a more

thermodynamically compatible salt mixture. Despite ZrF_4 satisfying the octet rule it still forms a coordination complex with an alkali fluoride such as potassium fluoride through the reaction

$$ZrF_4 + 2K^+ + 2F^- \rightarrow ZrF_6^{-2} + 2K^+. \tag{2.3}$$

In terms of a dot diagram this appears as

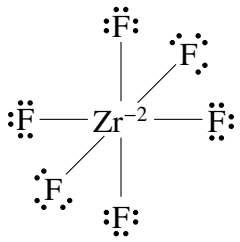

forming coordination complex with a total of 48 electrons [26]. The ZrF_6^{-2} reduces the vapor pressure of the ZrF_4 molecule and reduces the corrosion potential of the salt as a whole [22].

The salt LiF-NaF-KF (46.5-11.5-42 mol%) follows the same coordination complex based rules, however it is entirely composed of alkali fluorides, all of which are unable to pull in disassociated fluorine ions and capture them. These free fluorines are not tied down and can move easily through the salt. Mobile fluorides make flinak more corrosive, a fact which has been observed [22].

No matter what form free fluorines are in they are still free to move if they find more thermodynamically stable conditions. This ionic nature of the salt is the main contributor to the complex corrosion chemistry.

2.3.2 Redox Potential

The ionic character of the salt lends its chemistry to be measured by a voltage, or redox potential. The redox potential is a electric measurement of the tendency for the ionic molten salt to acquire or lose electrons when a new element is introduced. This voltage is defined by the Nernst Equation as

$$E = E^\circ - \frac{RT}{nF} \ln(Q) \tag{2.4}$$

where E° is the standard cell potential at the temperature of interest, R is the universal gas constant, T is the temperature, n is the number of moles of electrons transferred in the cell reaction, F is the Faraday constant, and Q is called the reaction quotient, an indicator of relative concentrations of all species involved in the reaction. When a salt is reducing it craves electrons and will gain them from any other species through a reduction-oxidation reaction, or redox reaction. This is different from a Lewis acid base reaction, as shown in Section 2.3.1, in that the oxidation state of the species involved must change. A good example of a redox reaction is the reaction between hydrogen gas and fluorine gas resulting in hydrogen fluoride

$$H_2 + F_2 \rightarrow HF. \tag{2.5}$$

which can be written in terms of half cell reactions. The oxidation half reaction being

$$H_2 \rightarrow 2H^+ + 2e^-, \tag{2.6}$$

with the reduction reaction occurring simultaneously

$$F_2 + 2e^- \rightarrow 2F^-. \tag{2.7}$$

These two reactions can be added together to create the total reaction shown in Eq. 2.5. In these reactions the oxidation state of the H_2 and F_2 are zero by definition. As the reaction occurs, H_2 becomes oxidized to a oxidation state of +1 from 0, or loses electrons, where as F_2 becomes reduced to an oxidation state of -1 from 0, or gains electrons. Understanding the nature of a half cell reaction is key to understanding the chemistry of a molten salt, where ions, molecules, gases, and metals all interact simultaneously.

A great use for the redox potential lies in the the reaction quotient, which is directly related to

the equilibrium constant of the reaction, explained in Section 2.3.3.

$$\lim_{t \to +\infty} Q = K_{\text{eq}} \tag{2.8}$$

where t is time. As the concentrations of reactants and products reaches equilibrium, $Q = K_{\text{eq}}$.

2.3.3 Chemical Equilibrium and Fluorine Potential

Many reactions which occur in molten fluoride salts are reversible. A reversible reaction is a reaction which results in a mixture of products and reactants–it never reaches full completion on either side. For example the reaction

$$aA + bB \rightleftharpoons cC + dD \tag{2.9}$$

has an equilibrium constant, K_{eq} which can be defined as

$$K_{\text{eq}} = \frac{[C]^c[D]^d}{[A]^a[B]^b}. \tag{2.10}$$

Bracketed constants are activities, a, or partial pressures, p. The activities of each species which are defined as

$$a = \gamma m \tag{2.11}$$

where γ is the activity coefficient, a dimensionless indicator to account of the thermodynamics of a mixture, and m is the molality in moles solute per mass solvent. Activity is interchangeable with partial pressure in the case of a gas product or reactant. The exponents in Eq. 2.10 stand for the molar coefficients [27]. When the equilibrium constant is less than one, the reaction is reactant favored. This is because the activities, and therefore the concentrations, are higher in the denominator than in the numerator. Conversely, when the equilibrium constant is greater than one

the reaction is considered product favored. Additionally, the equilibrium constant is dependent on temperature–a reaction can reverse depending on temperature. Putting together these concepts, it can be seen that salt equilibrium, and therefore corrosion, is not a on or off issue, it never is completely stopped, only curtailed. Metal ions of containment vessels will always exist in a salt to some degree depending on an equilibrium constant.

The equilibrium constant can be related to the concept of Gibbs free energy through the relation

$$\Delta G^0 = -RT \ln(K_{\text{eq}}), \tag{2.12}$$

or

$$K_{\text{eq}} = \exp\left(\frac{\Delta G^0}{-RT}\right). \tag{2.13}$$

A Gibbs free energy is just a measure of the energy in a chemical system able to do work. In the case of chemical reactions a Gibb's free energy can be applied to determine if that reaction is thermodynamically possible. Applied to a element or molecule, it is a measure of that substance's ability to perform chemical reactions. Since the anion of the molten salt is the main cause of the of thermodynamic corrosion of container materials, the chemical potential is based off of it. In the case of fluoride salts the anion is F^-, but is also typically expressed as diatomic fluorine, F_2. Diatomic fluoride is chemically just $2F^-$, as shown in Eq. 2.7, hence the fluorine potential. This fluorine potential can be expressed as

$$\Delta \overline{G}_{\text{F}_2} = RT \ln p_{F_2}, \tag{2.14}$$

where $\overline{G}_{\text{F}_2}$ is the Gibbs free energy of F_2, R is the gas constant, T is the temperature, and p_{F_2} is the partial pressure of free fluorine ions in the salt [28]. Once again, the partial pressure of fluorine ions is an abstract concept, but chemically the only difference between F_2 and $2F^-$ is the charge driven mobility.

Fluorine potential based structural metal corrosion is strongly related to the free energy of formation of the the corresponding metal fluoride. Fluoridation reactions with more negative free energy of formation indicate that metal is more prone to attack in fluoride salt than metals with a less negative energy of formation at any fluorine potential. By examining the Gibbs free energy

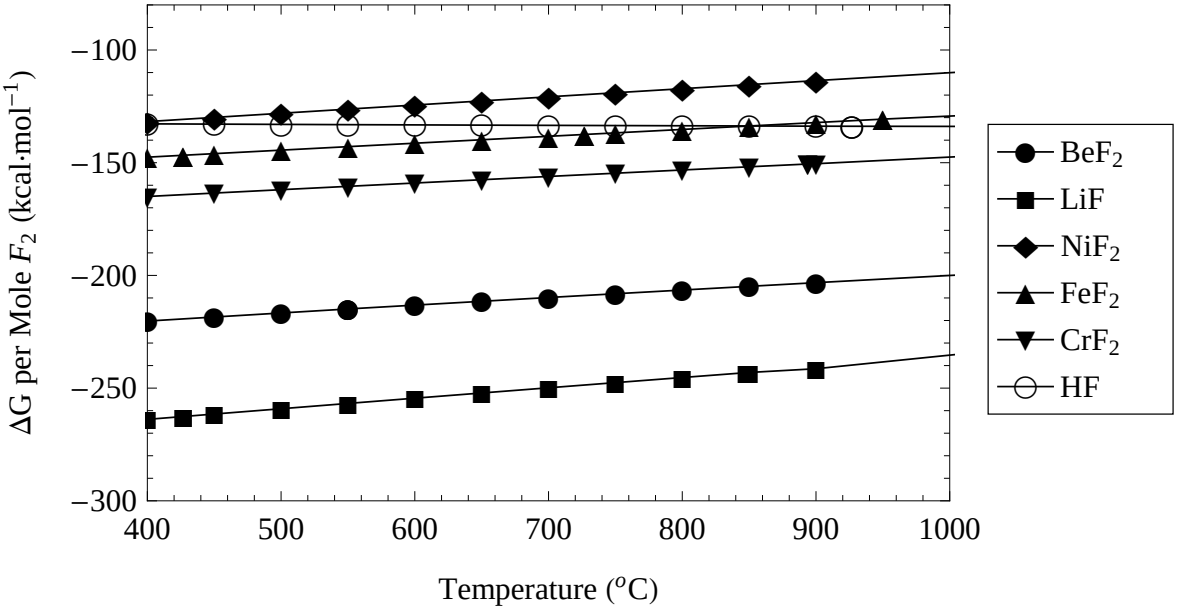

Figure 2.3: Gibbs energies of formation for assorted fluorides as a function of temperature. Other interesting fluoride compounds have been excluded for clarity.

of formation of the metal fluorides per mole fluorine, a series can be made which ranks each metals nobility. It has been found that in molten fluoride salts the tendency for common alloying constituents to be attacked increased in the following order: W, Mo, Ni, Co, Fe, Nb, Cr, Mn, Ti, Zr, Al, with Al being the most dissolution prone and tungsten being the most noble [24, 29]. Hydrogen, even though chemically 'metallic' is usually left out of this series because it does not have a definitive placement. As shown in Figure 2.3, depending on the temperature, hydrogen can be more noble or less noble than iron, but always less noble than nickel. This is part of the explanation for the addition of the hydrogen during the chemical purification process, as detailed in Section 2.5.2. Fluorine ions, at molten salt temperatures, are more attracted to the hydrogen

in the salt as compared to the nickel. Their presence reduces nickel corrosion, but as mentioned before, never eliminates it due to the equilibrium constants.

While the Gibbs free energy of formation for the metal fluorides will control the tendency for the metal to be corroded, the fluorine potential controls the actual concentration of metal fluorides in the salt. Most corrosion resistant alloys depend on suitable ratio of Cr, Fe, Mo, and Ni to provide structural rigidity and oxidation resistance at high temperature. Out of these main alloying constituents, fluoride salts tend to primarily attack chromium through grain boundary dissolution due to its highly negative Gibbs free energy of formation [24]. This process can be explored through the corrosion reaction

$$\mathrm{Cr} + 2\mathrm{F}^- + 2\mathrm{H}^+ \rightleftharpoons \mathrm{Cr}^{2+} + 2\mathrm{F}^- + \mathrm{H}_2, \tag{2.15}$$

which is usually just simplified for convenience as

$$\mathrm{Cr} + 2\mathrm{HF} \rightleftharpoons \mathrm{CrF}_2 + \mathrm{H}_2. \tag{2.16}$$

By using Eqs. 2.10 and 2.13 an equilibrium expression for Eq. 2.16 can be formed as

$$\frac{p_{\mathrm{H}_2} a_{\mathrm{CrF}_2}}{p_{\mathrm{HF}}^2} = \exp\left(\frac{\Delta G^0_{\mathrm{CrF}_2} - 2\Delta G^0_{\mathrm{HF}}}{-RT}\right). \tag{2.17}$$

The partial pressure and Gibbs free energy of hydrogen fluoride can be cleverly eliminated by using the reaction

$$\mathrm{H}_2 + 2\mathrm{F}^- \rightleftharpoons 2\mathrm{H}^+ + 2\mathrm{F}^- + 2\mathrm{e}^-, \tag{2.18}$$

which, as mentioned before, is commonly expressed as

$$\frac{1}{2}\mathrm{H}_2 + \frac{1}{2}\mathrm{F}_2 \rightleftharpoons \mathrm{HF}. \tag{2.19}$$

Through the use of Eqs. 2.10 and 2.13 there exists an equilibrium for this reaction

$$K_{\text{eq}} = \frac{p_{\text{HF}}}{\sqrt{p_{H_2}} + \sqrt{p_{F_2}}} = \exp\left(\frac{\Delta G^0_{\text{HF}}}{-RT}\right). \tag{2.20}$$

Which can be manipulated to solve for the fluorine potential

$$\Delta\overline{G}_{\text{F}_2} = RT \ln p_{F_2} = 2RT \ln\left(p_{\text{HF}} / \sqrt{p_{H_2}}\right) + 2\Delta G^0_{\text{HF}} \tag{2.21}$$

Eliminating the partial pressures of HF and H_2 using Eq. 2.21 with 2.17 yields the results

$$RT \ln\left(a_{\text{CrF}_2}\right) = \Delta\overline{G}_{\text{F}_2} - \Delta G^0_{\text{CrF}_2}. \tag{2.22}$$

Solving for the activity, or concentration shown in Eq. 2.11, its found that

$$a_{\text{CrF}_2} = \exp\left(\frac{\Delta\overline{G}_{\text{F}_2} - \Delta G^0_{\text{CrF}_2}}{RT}\right). \tag{2.23}$$

Therefore, it can be seen that the concentration of dissolved metal fluorides is only dependent on the temperature, the fluorine potential, and the Gibbs free energy of formation of the fluoride. Figure 2.4 shows the effect fluorine potential has on the ability to form metal fluorides. Linearly decreasing fluorine potential logarithmically reduces the thermodynamic ability to form metal fluorides. Therefore, in order to prevent excessive corrosion of alloys, the fluorine potential should be as negative as reasonably possible without reducing the salt itself. The only thing needed to make a reducing salt is to introduce a chemical species which predominately ties up the ability for the fluorine ions to perform work on other elements.

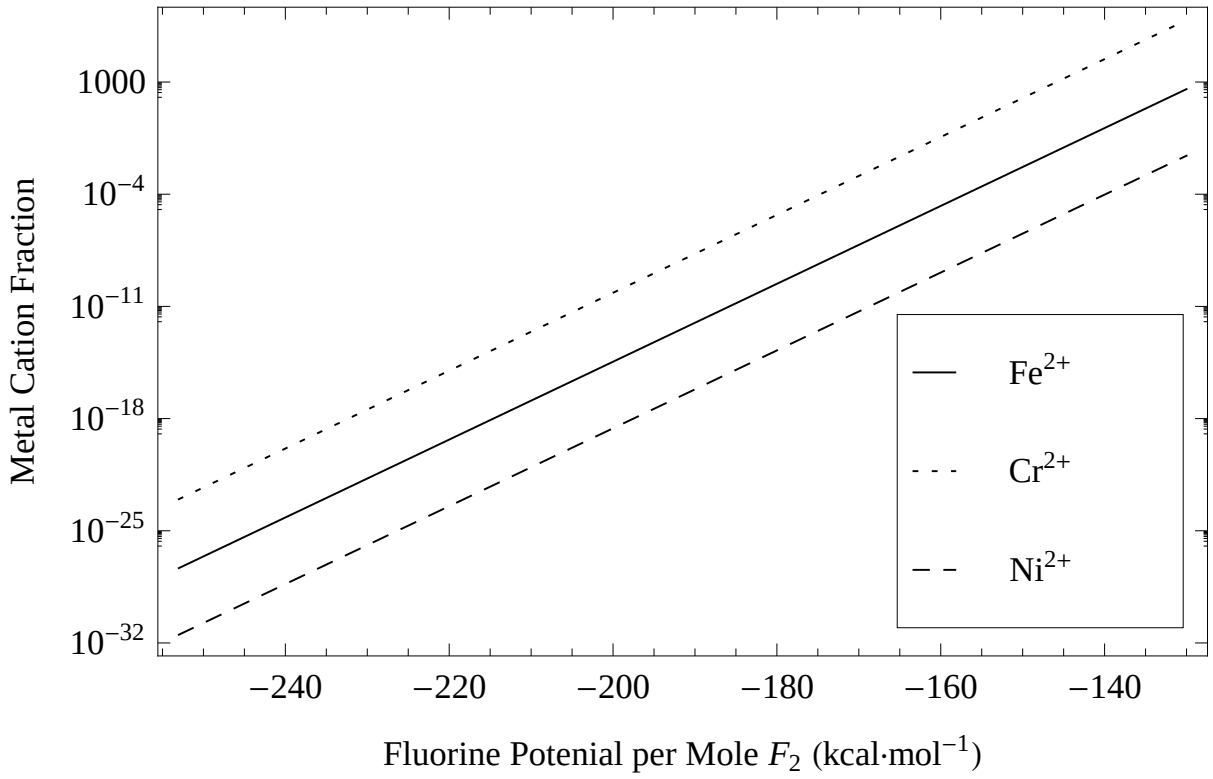

Figure 2.4: A plot of fluorine potentials vs metal ion concentration at 900K. The differences in activity at different temperatures is due to the difference in Gibbs free energies of formation.

2.3.4 Measured Solubilities of Cr, Fe, and Ni in Flibe

To gauge the relationship of fluorine potential and metal fluorides in flibe, a series of tests were performed where the fluorine potential was set using a controlled ratio of hydrogen fluoride to hydrogen while exposed to chromium, iron, and nickel in LiF-BeF_2 (62-38 mol%) [30]. After a sufficient time, the salt would equilibrium with the metals and gas, creating a dissolved concentration of the metal. This concentration was measured and an equilibrium constant was extracted. Different gas ratios were used over multiple temperatures for error reduction. Even though the salt use was not LiF-BeF_2 (66-34 mol%), it was assumed to be valid for general engineering purposes

with LiF-BeF_2 (66-34 mol%). Data was gathered for a reaction of interest, such as

$$FeF_2 + H_2 \rightleftharpoons Fe + 2HF, \tag{2.24}$$

by defining an equilibrium constant, K_N where

$$K_N = K_{eq}\gamma_{FeF_2} = \frac{p_{HF}^2}{p_{H_2} m_{FeF_2}}. \tag{2.25}$$

The quantity m_{FeF_2} is the concentration of iron fluoride in the salt as a mole fraction.

It was found that nickel was the most noble out of the three major alloying elements, a fact which was already understood through the nickel fluoride Gibbs free energy of formation. Quantitatively it was discovered that for a given fluorine potential, nickel was roughly 1000 times more corrosion resistant than iron and roughly 100000 times more corrosion resistant than chromium. The results are displayed as a function of temperature in Table 2.1. The general trend for a given

Table 2.1: Values of K_N in atmospheres for Cr, Fe, and Ni at various temperatures [30].

Temperature (°C)	500	550	600	650	700	750	800	850
Cr	-	-	-	-	-	1.92×10^{-4}	4.42×10^{-4}	1.19×10^{-3}
Fe	-	-	1.33×10^{-1}	-	5.28×10^{-1}	-	1.88	-
Ni	5.04×10^{3}	9.90×10^{3}	1.73×10^{4}	-	-	-	-	-

hydrogen to hydrogen fluoride ratio is as K_N increases, the amount of metal allowed to exist in the salt decreases. Small K_N are undesirable for innate chemical inertness. Additionally, the salt becomes less corrosive as temperatures increase. The constants measured by Blood are invaluable for determining the ratio of hydrogen fluoride to hydrogen which could be allowed in a purification or reactor operation scenario.

2.3.5 Relationship of Fluorine Potential, Redox Potential, and Chemical Equilibrium

The thermodynamic behavior of molten salt has been defined through various means and metrics, which can be very confusing to the initiate, but it should be noted that these are all fundamentally different ways of explaining the same fact.

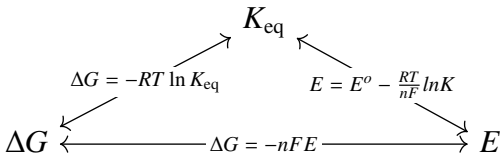

In different situations it becomes convenient to use different schools of thought to establish points, although all expressions are equally as valid. For instance, with multiple elements it is easiest to picture the salt as system in constant search for equilibrium. In this case it would be best to picture the salt through the equilibrium constant K_{eq}. For raw measurements of a salt's corrosivity, it would prudent to use the redox potential. If calculations need to be done on the thermodynamic equilibrium of a metal species in a salt, fluorine potential would be the best option.

2.3.6 Summary of Equilibrium

Molten salt thermodynamics are best thought of as a salt's constant pursuit of equilibrium with itself and its surroundings. This can be explained from the bottom up. Melting the raw component LiF without it contacting other elements or molecules forms the ions Li^+ and F^-. This system is in complete chemical equilibrium with itself and satisfies the octet rule. Adding BeF_2 allows the salt to find a new equilibrium as shown in Section 2.3.1 in Eq. 2.6, through the formation of the coordination complex of BeF_4^{-2}, further satisfying the octet rule. This is a final, thermodynamically stable equilibrium of the flibe raw salt.

Placing the newly formed flibe into a nickel container now forces the ionic molten salt to search for new six way equilibrium between BeF_2, BeF_4^{-2}, Li^+, Ni, Ni^{2+}, and F^-. This equilibrium can

be calculated through the data provided by Blood. Lastly, adding a sacrificial 'redox agent', such as zirconium metal to the salt will force a new equilibrium. Corrosion experiments are best for multiple metal systems. Results from experiments show that the fluorine ions will exchange and establish an equilibrium with Zr^{4+} and Ni^{2+} which heavily favors the formation of Zr^{4+}, leaving the nickel largely unaffected.

Through these mechanisms it can be seen that salt corrosion is a complex, but balanced, zoo of elements, molecules, and ions which are constantly searching for a more stable equilibrium. They are allowed to find this equilibrium due to their ionic and mobile nature. In order to engineer with these salts, the thermodynamic properties cannot be overlooked.

2.4 Impurity Driven Corrosion

Although fluoride salt corrosion is extensively controlled by thermodynamic based corrosion, impurities of various types can have effects on corrosion which must be eliminated. Initial impurities, such as oxide layers and water vapor, spend themselves up, thermodynamic based corrosion dominates and the corrosion rate slows. However, leaks, purge gas contamination, and exposure to atmosphere can cause an continuous source of contamination. As shown in Figure 2.5, this effect can be dramatic, creating an initial corrosion rate of around 6 mm yr^{-1}. After impurities were used up after 500 hours, corrosion slowed to roughly 1 mm yr^{-1} Removing these impurities is paramount in order to preserving the integrity of container materials. There are several key impurities which must be managed in order to reduce this effect: water, oxides, and sulfides.

2.4.1 Water Hydrolysis Reactions

If beryllium fluoride or zirconium tetrafluoride salts come in contact with water vapor at high temperature, hydrolysis occurs which releases hydrogen fluoride gas and leaves oxygen containing molecules behind [31]. The key water equations are outlined by Shaffer. The spectator ions,

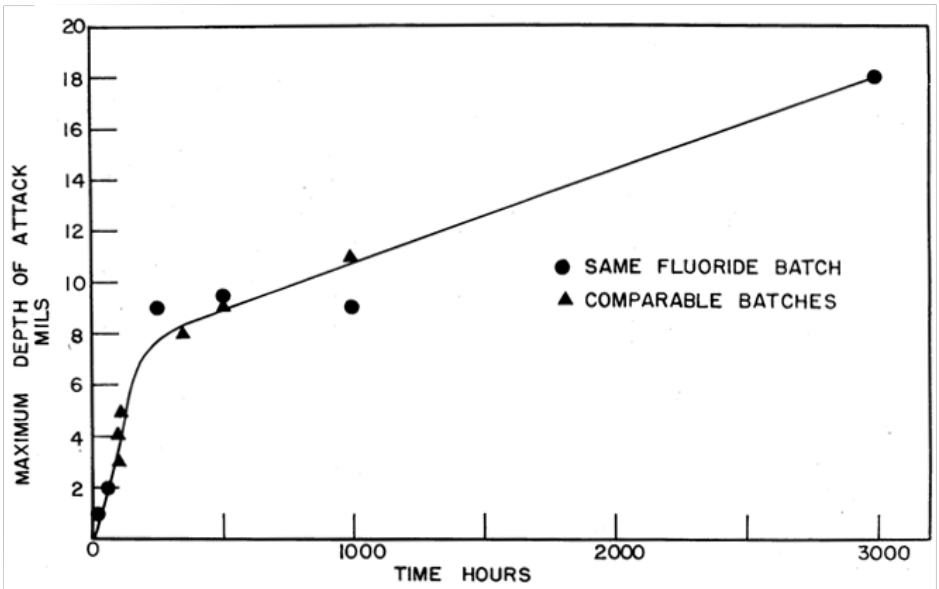

Figure 2.5: A time dependent plot of corrosion depth by fluorides in Inconel[3].

beryllium and zirconium, are left out for simplicity.

$$H_2O + 2F^- \rightleftharpoons O^{2-} + 2HF \tag{2.26}$$

$$H_2O + F^- \rightleftharpoons OH^- + HF \tag{2.27}$$

$$M^\circ + xHF^- \rightleftharpoons \frac{x}{2}H_2 + MF_x \tag{2.28}$$

Where M is any metal in the exposed alloy, and x is the oxidation state of the metal M. In order to produce corrosion, these reactions must all work together.

By introducing water into a beryllium fluoride or zirconium tetrafluoride containing salt, a fluoride ion can react with it producing an insoluble oxide or hydroxide and hydrogen fluoride, as shown in Eqs. 2.26-2.27. The hydrogen fluoride can dissolve in the salt or come out at as gas. Regardless of the mechanism, the lack of hydrogen in the presence of hydrogen fluoride will create

changes in the fluorine potential, as explained by Eq. 2.21. Additionally, removal of one mole of beryllium fluoride or zirconium fluoride causes the loss of fluorine ion complexing, introducing up to four or six new free fluorine ions. Both of these chemical changes can lead to the attack of metals which are exposed to the molten salt, converting them into metal difluorides, shown in Eq. 2.28. The metal difluorides can then dissolve into the salt, exposing more bare metal [5, 30]. The battle against water and oxygen in the salt was recognized as one of the most important parts of chemical control, and is key to preventing excessive corrosion. It should be noted that none of this applies to alkaki fluoride compounds, such as those found in flinak salt, which are impervious to this type of attack due to the high stability of their ionic bonds.

2.4.2 Sulfur Corrosion Reactions

Another key impurity is sulfur. Although nickel-based alloys are considered the best alloys for use with molten salts due to their superior corrosion resistance to the F^- ion, they are not able to withstand sulfur at high temperatures. In the production facilities for salt at ORNL there were several instances of sulfide based corrosion on nickel and copper based components [32]. The chemical corrosion process, as determined by ORNL, begins with sulfates, which are present in the salt [32]. At a temperature range of 500°C to 800°C, these sulfates decompose according to

$$SO_4^{-2} \rightarrow SO_3 + O^{2-}. \tag{2.29}$$

When the newly formed sulfur trioxide exists at low partial pressures it is able to decompose into sulfur dioxide,

$$SO_3 \rightarrow SO_2 + \frac{1}{2}O_2. \tag{2.30}$$

All three of these sulfur compounds are able to attack nickel and convert it to nickel sulfide and nickel oxide,

$$SO_4^{-2} + 4Ni \rightarrow 3NiO + NiS + O^{2-}, \tag{2.31}$$

$$SO_3 + 4Ni \rightarrow 3NiO + NiS, \tag{2.32}$$

$$SO_2 + 3Ni \rightarrow 2NiO + NiS. \tag{2.33}$$

These reactions are also able of producing non-stoichiometric compounds of nickel and sulfur, which have been left out from this discussion. In the presence of hydrogen gas, all the sulfur compounds can be converted into hydrogen sulfide,

$$SO_4^{-2} + 4H_2 \rightarrow O^{2-} + H_2S + 3H_2O, \tag{2.34}$$

$$SO_3 + 4H_2 \rightarrow H_2S + 2H_2O, \tag{2.35}$$

$$SO_2 + 3H_2 \rightarrow H_2S + 2H_2O. \tag{2.36}$$

This hydrogen sulfide can react with nickel through the reaction,

$$H_2S + Ni \rightleftharpoons NiS + H_2 \tag{2.37}$$

ultimately causing accelerated degradation of the nickel. The reversible nature of this reaction indicates that corrosion by formation of nickel sulfide can be stopped by adding the proper partial

pressure of hydrogen to the mix.

2.4.3 Galvanic Corrosion

Everything in contact with a ionic molten salt can interact through the electromotive force. If a metal species is allowed to dissolve into the solution through poor control of corrosion potential, its ions can move through the salt towards the species with the greatest standard potential cell. In corrosion tests conducted at the University of Wisconsin with LiF-NaF-KF (46.5-11.5-42 mol%) and 316 stainless steel crucibles it was found that chromium was dissolved and then plated onto graphite, forming chrome carbide compounds[33]. Other tests with flinak showed zirconium plating on samples [33]. Behavior like this is galvanic can be avoided by keeping metallic constituents in the salt to a minimum and by reducing the amount of different metals in contact with the salt.

2.5 Corrosion Control

A commercial FHR must have proper corrosion control in order to insure a long operational lifetime. Corrosion control must inhibit impurity and thermodynamic corrosion through the use of two systems: passive and active chemistry control. A passive chemistry control system can be implemented by using noble construction materials like pure nickel, salts with less free fluorine ions, and redox couples which 'buffer' the salt. Active chemistry control systems can be employed through a chemical treatment process, whether online or offline. Both these processes must create a chemical equilibrium and eliminate impurities which could corrode infrastructure, absorb neutrons, or change the heat transfer characteristics of the salt. Usually, salts were chemically treated first and then used in passively controlled systems, requiring minimal active control introduction [8]. These chemical treatments had to work on a large scale with industrial grade chemicals which could contain significant amounts of impurities. Fortunately, a joint batch production and purification process was developed and documented in great detail during the ARE and MSRE

[5, 8, 18, 34, 35]. Acceptable limits for impurities in a fluoride salt, created by these programs, are shown in Table 2.2.

Table 2.2: The maximum allowable concentration standards for the Molten-Salt Reactor Experiment's fluoride salts [35].

Impurity	Weight Percent	Parts Per Million
Water	0.1	1000
Cu	0.005	50
Fe	0.01	100
Ni	0.0025	25
S	0.025	250
Cr	0.0025	25
Al	0.015	150
Si	0.01	100
B	0.0005	5
Na	0.05	500
Ca	0.01	100
Mg	0.01	100
K	0.01	100
Li (Natural)	0.005	50
Zr (Natural)	0.025	250
Cd	0.001	10
Rare Earths (Total)	0.001	10

A few of these impurities can be removed by the sparging of a mixture of hydrogen fluoride and hydrogen through the molten fluoride salt. Other impurities can be handled through the introduction of a metallic reducing agent. Through these two methods, impurities can be either volatilized or precipitated in the form of insoluble particles. Volatilized impurities are removed through the effluent stream, while insoluble particles are removed by decantation and filtration [5].

2.5.1 Controlling Fluorine Potential

Fluorine potential of a salt, and therefore the thermodynamic corrosion, can be controlled through the the introduction of any reduction-oxidation agent. Three main controllers are: HF-H_2 gas or hydrofluorination, metal additions or redox agents, and dissolved metals with multiple oxidation

states or redox buffers [28].

As discussed in Section 2.3.3, hydrogen and hydrogen fluoride establish an equilibrium with fluorine in the salt through sparging, which can be seen through the gas reaction

$$\frac{1}{2}\mathrm{H_2} + \frac{1}{2}\mathrm{F_2} \rightleftharpoons \mathrm{HF}. \tag{2.38}$$

Therefore, the fluorine potential model can be used to establish an equilibrium as

$$K_{\mathrm{eq}} = \frac{p_{\mathrm{HF}}}{\sqrt{p_{H_2}} + \sqrt{p_{F_2}}} = \exp\left(\frac{\Delta G^0_{\mathrm{HF}}}{-RT}\right). \tag{2.39}$$

Just as before, solving for the fluorine potential yields

$$\Delta\overline{G}_{\mathrm{F_2}} = RT \ln p_{F_2} = 2RT \ln\left(p_{\mathrm{HF}}/\sqrt{p_{H_2}}\right) + 2\Delta G^0_{\mathrm{HF}} \tag{2.40}$$

Therefore, by keeping the salt in contact with the proper mixture of hydrogen and hydrogen fluoride gas for a long enough time, a wide range of fluorine potentials can be obtained. Fluorine potentials achievable for common hydrofluorination ratios are shown in Figure 2.6. Decreasing the amount of hydrogen in the mix will decrease the magnitude of the fluorine potential, while increasing it will slowly increase the magnitude. Values that have been used before are anywhere from 1:3 to 1:10 giving ranges of $\Delta\overline{G}_{\mathrm{F_2}} = -136.5, -140.5$ kcal mol^{-1}. By exposing salt to this ratio of gases the fluorine potential of it will come into equilibrium and adopt this fluorine potential simply by diffusion of gases and ions.

The fluorine potential can also be controlled by the addition of suitable metallic reducing agent. For flibe, beryllium and zirconium were commonly used although lithium could work as well. The reaction of beryllium with free fluorine is

$$\mathrm{Be} + \mathrm{F_2} = \mathrm{BeF_2}. \tag{2.41}$$

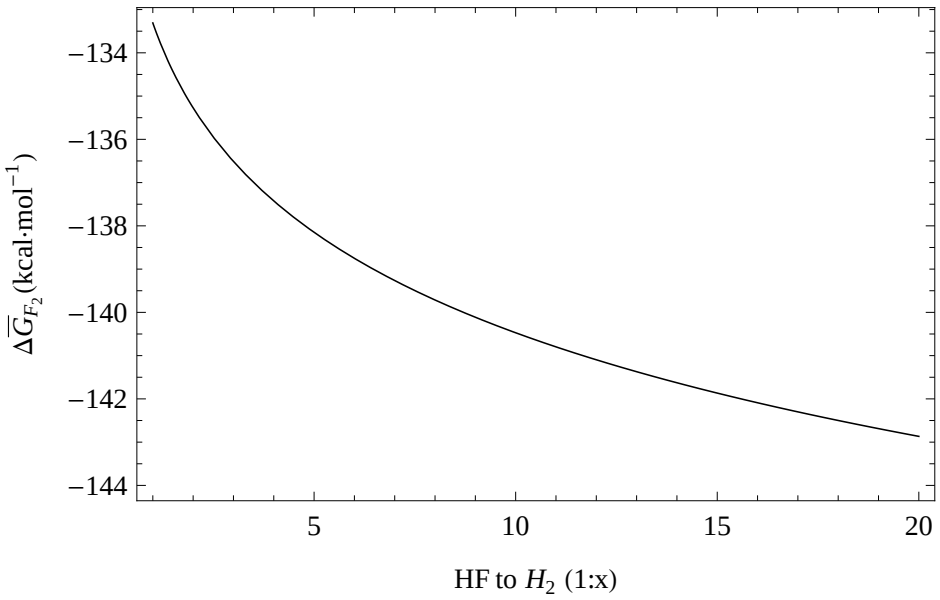

Figure 2.6: A plot of fluorine potentials due to varying ratios of H_2 to HF, where x is the ratio of hydrogen with hydrogen fluoride fixed to one.

The law of mass action in this case depends on the activity coefficient of BeF_2 in flibe:

$$\frac{a_{\mathrm{BeF_2}}}{p_{\mathrm{F_2}}} = \exp\left(\frac{\Delta G^0_{\mathrm{BeF_2}}}{-RT}\right). \tag{2.42}$$

The fluorine potential can then be solved for as

$$\Delta\overline{G}_{\mathrm{F_2}} = RT \ln p_{F_2} = RT \ln\left(a_{\mathrm{BeF_2}}\right) + \Delta G^0_{\mathrm{BeF_2}}. \tag{2.43}$$

At 900K, $\Delta G^0_{\mathrm{BeF_2}} = -209.2$ kcal mol^{-1} as determined from literature [28]. The activity coefficient, $a_{\mathrm{BeF_2}}$, is a product of the molar percent BeF_2 in the flibe solution as well as the activity coefficient of this component in flibe [28]. At 33 mol % BeF_2 and it is found that $a_2 = 0.026$ yielding a fluorine potential of $\Delta\overline{G}_{\mathrm{F_2}} = -215.7$ kcal mol^{-1}.

2.5.2 The Hydrofluorination Process

The hydrofluorination process was the key step to making salts which were compatible with their containers. The goal of the process was to rid the salt of impurities through volatilization, recantation, and filtration as well as set the fluorine potential to a reasonable level. The hydrofluorination process and the fluoride salt plant at ORNL was highly successful. At the end of its lifetime it had produced 132000 lbs. of salt, of which 26000 lbs. went to the molten salt reactor experiment.

Before hydrofluorination even began, salts where weighed and mixed in their individual component form. From there they were moved into a suitable, corrosion resistant container, and melted. Upon melting, a sparge of helium and hydrogen was introduced into the salt at a relatively high flow rate [34]. This gas removed carbon as well as some water. More recently, pure helium was used also for entrainment gas by for fluoride salts by Calderoni at 530°C with success [36]. Argon was also deemed suitable by Ambrosek with chloride salts [37]. The only requirement is that the sparge gas be inert and have low oxygen and water content. To assure this, the fluoride salt processing plant at ORNL had many molecular sieves which would filter out any water from supplied inert gasses [5]. These sieves rotated; while some were filtering, the others would be regenerating [5]. Maximum water vapor concentrations were specified at 18 ppm and normally did not exceed 5 ppm [5]. Modern laboratory gasses are available in high purity form, reducing the need for filtration. After initial entrainment, salt was treated by the hydrofluorination process.

The MSRE's hydrofluorination process evolved over the course of the program. In the beginning of the program, just hydrogen fluoride was used [18]. While the hydrogen fluoride worked to remove oxide impurities from the melted salt by reversing the water hydrolysis Eqs. 2.26 and 2.27, it also caused fluoridation of the metal in which the reaction occurred in through the impurity corrosion Eq. 2.28. These metal fluorides then dissolved into the salt, causing unwanted contamination. In order to remove these metal impurities from the salt, a treatment which involved alternating hydrogen fluorine and hydrogen gas was used [5]. The reversibility of Eq. 2.28

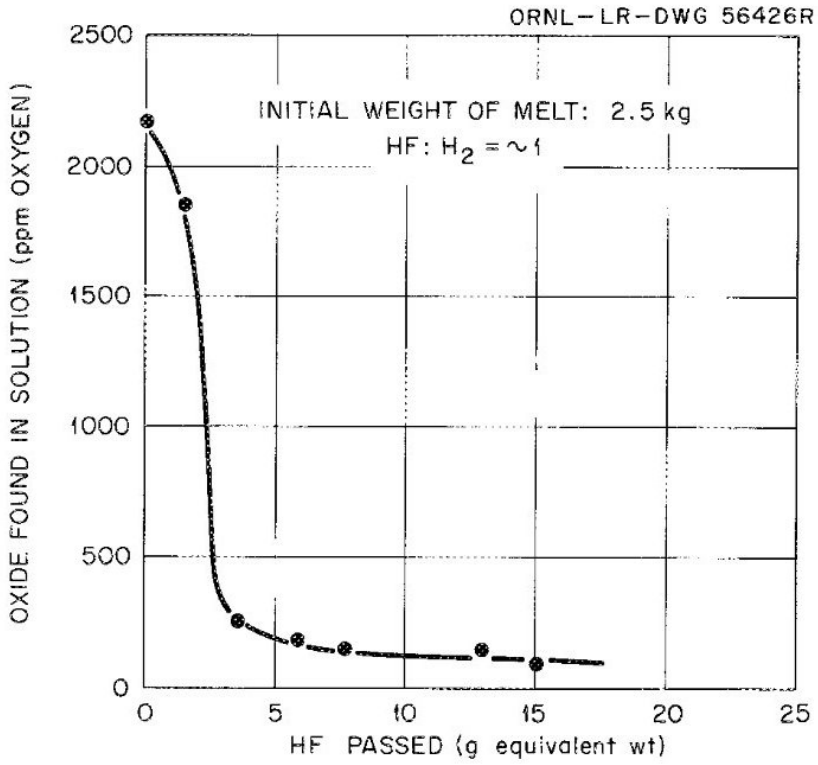

Figure 2.7: Measured oxides in LiF-BeF_2 (63-37 mol%) at 700°C as a function of hydrogen fluoride passed.

caused metals to precipitate out of solution with the salt, reducing contamination. However, the alternate gas treatment method caused the reaction chamber to be continually corroded, dissolved, and reduced, resulting in severe corrosion. It was finally suggested that the hydrogen fluorine and hydrogen be mixed and then sparged [5]. Changing the ratio provided control over vessel corrosion, as shown by Blood in Section 2.3.4. This resulted in minimal corrosion of the reaction vessel provided the correct partial pressures of hydrogen and hydrogen fluoride were used [5]. By using more hydrogen gas in the mixture it would make the environment more reducing. Using less would cause more corrosion, but would speed up the reaction rate. For carbon, which is relatively inert, a ratio of HF:H_2 of 1:3 can be used. Nickel vessels tend to fair better with ratios of 1:5 to 1:10. These ratios were the best skew of equilibrium towards water production while keeping equilibrium towards nickel, rather than nickel fluoride.

2.5.3 Oxide Removal

The fluoride salts of interest LiF-BeF_2 (66-34 mol%) and KF-ZrF_4 (58-42 mol%) are very hygroscopic. Upon melting these untreated salts, absorbed water will react with salts forming oxides [5, 31]. Oxides produced by melting add to the already present oxides and hydroxides in commercially available salt. These oxides were unwanted in a reactor because the would react with the dissolved uranium tetrafluoride salt and produce uranium dioxide which would precipitate out of solution. Additionally, oxides were largely insoluble and could clog components and build scale on surfaces [5]. To prevent this, oxides and hydroxides were converted to water vapor through the reactions shown in Eqs. 2.26 and 2.27. Equilibrium measurements for these reactions have shown the hydrofluorination process to be an effective process which becomes more efficient at lower temperatures [5, 38].

Oxide removal was performed by the hydrogen fluoride in the hydrofluorination process. Standard procedure consisted of sparging the melted fluoride mixture with a 1:5 or 1:10 ratio of anhydrous hydrogen fluoride and hydrogen gas at a rate of around 2.5 L m^{-1} for around 70 hours [5, 34]. Recently, Calderoni used a ratio of 1:11 HF-H_2 at a rate of 0.14 L m^{-1} [36]. The HF-H_2 mixture was also used in an Engineering Test Loop with mild corrosion of the Inconel container with no increase in dissolved metal impurities [39]. However, in all situations, forcing the oxide-hydrogen fluoride reaction to push to completion was considered a losing battle. Towards the end of the reaction, excessive amounts of hydrogen fluoride would have to be used to remove small quantities of oxide [5].

2.5.4 Removal of Sulfur

Just as hydrogen sulfide can corrode nickel through the reversible reaction,

$$H_2SNi \rightleftharpoons NiS + H_2, \tag{2.44}$$

it can be reversed through the introduction of a higher partial pressure of hydrogen.

To prevent the corrosion of the salt reaction chamber, sulfur impurity concentrations must be reduced to below 10 ppm [5]. The sulfur, which comes in commercially available salt, must first be reduced to a sulfide ion and then volatilized as H_2S through a reaction with hydrogen [5]. Beryllium was also found as a suitable candidate for rapidly clearing the sulfate out of the salt.

2.5.5 Metal and Metal Fluoride Removal

Metal and unwanted metal fluorides were removed in a two or three step process in a final phase of the purification process. It was thought that metals could be removed in the first step by melting and filtering component salts before hydrofluorination but oxides ended up clogging the filter. To avoid this problem, filtration was only performed after hydrofluorination, hydrogen sparge, and potentially metal addition [5, 35].

Hydrogen sparge was first step in removing metals. As shown by Blood, the hotter the salt required less hydrogen to produce low levels of dissolved metals; temperatures of 700°C were routinely used [5]. Higher temperatures would further increase reaction rates but at the price of reducing heater lifetime. Reaction completion was easily measured during the hydrogen sparge step. As metal fluorides were reduced to their metallic components, hydrogen would bind with the fluorine to evolve hydrogen fluoride. The concentration of hydrogen fluoride in the effluent stream was directly related to the concentration of iron fluoride remaining in the salt [5].

The second method of reducing metal fluorides was the addition of an active metal such as beryllium or zirconium in the salt [5, 35]. Both of these metals were found to work well to reduce chromium, iron and nickel. Their additions were later halted due to process control limitations [5]. Reactions of metal fluorides with active metals was found to be nonstoichiometric, potentially due to surface coating. Active metals were also found to be suspended in the salt, rather than fully dissolved. This suspension had the potential to clog the filter, which was the last step to reduce

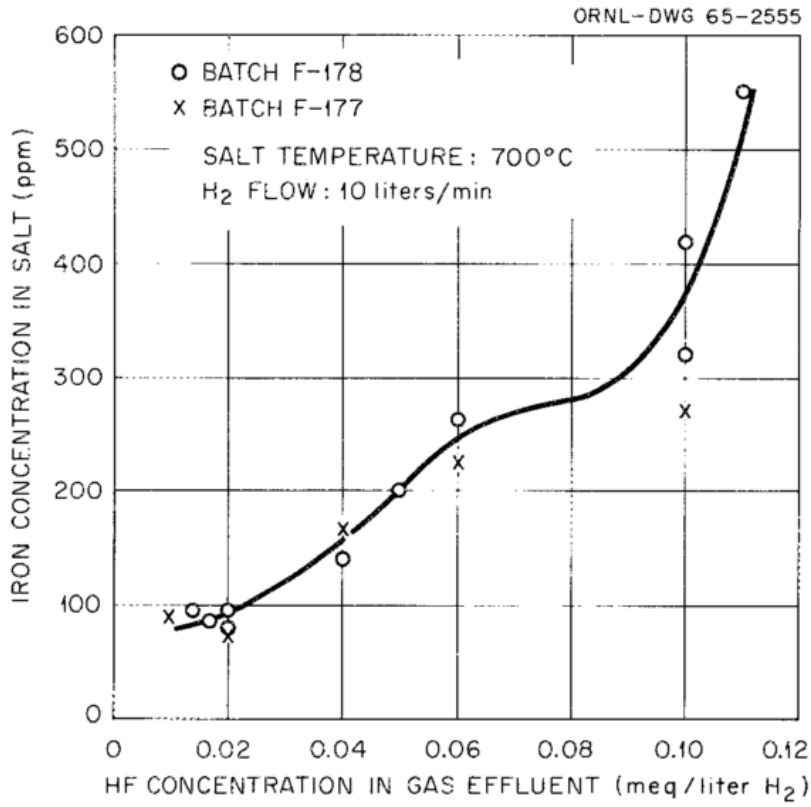

Figure 2.8: Iron concentration as a function of hydrogen fluoride concentration in the effluent stream.

metal impurities. Active metal reduction was eventually only used in processes which required timely reduction of structural metals, or in salt which was severely contaminated with chromium [5].

It is not enough to reduce the metals out of solution, they must be completely removed from the salt, therefore salt filtration was the last step in removing metals. The filtration process involved slowly moving salt through a sintered or other porous type of filter [5, 40]. By slowly moving the salt through the filter, any reduced metals that had settled to the bottom of the reduction vessel would left undisturbed, essentially decanting the salt. Typical filter pore size was around 40 microns, although 20 micron pore sizes were used as well [40]. Metals of construction tested were Monel, nickel, Inconel 600, and 347 stainless steel. Ultimately, Inconel 600 was chosen for large

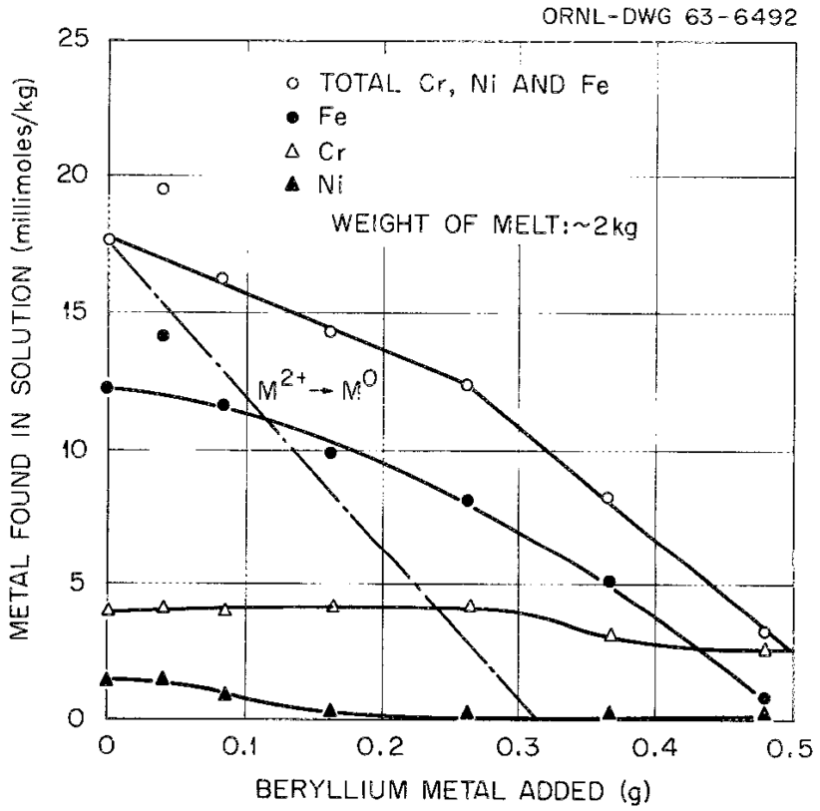

Figure 2.9: Metals concentration as a function of beryllium metal added.

scale batches due to its corrosion resistance and high temperature strength, while nickel was used for small scale [40].

2.6 Past Determination of Salt Composition and Impurities

In order to prevent corrosion, ensure proper heat transfer and fluid properties of the salt, and monitor the health of the MSRE's salt containment vessels, methods which measured the salt composition and its impurities were developed. These methods relied on the strong analytic chemistry division at ORNL and used many experimental methods to gain a full understanding of the salt. Of the most important were determinations of metallic beryllium, lithium, iron, chromium, nickel, as well as oxides, water, and hydroxides. Determinations of these quantities had to be within ppm to weight percent sensitivity with good repeatability [41].

2.6.1 Measurements of Beryllium

Measurements of beryllium in the salt were determined by the photoneutron method [42, 43, 44]. This method used a ^{124} Sb source to provide gamma ray photons of the proper energy to induce the nuclear reaction

$$^{9}\text{Be} + \gamma \rightarrow \text{n} + ^{8}\text{ Be}. \tag{2.45}$$

This reaction created a neutron which could be thermalized and counted with a boron trifluoride neutron detector. The results were calibrated by using a sample of known beryllium concentration. The photoneutron technique was done on a bench top with shielding of only four inches of lead, had excellent accuracy, repeatability, and was quick [42]. High concentrations of other elements, including Li and Na, did not affect the beryllium measurement [42]. The main drawback was that the source had to be irradiated into ^{124} Sb from ^{123} Sb. An isotopically pure source of ^{124} Sb cost $3150, including irradiation, in 1959 [42]. The source then decayed and was only good for two half-lives or 120 days. Results of testing with fluoride salts, as compared to chemical methods are shown in Figure 2.3 [42].

Table 2.3: A comparison of the photoneutron technique of beryllium fluoride salts, oxides, and alloys with chemical techniques.

	Be Content (%)			
Sample Composition	Photo-Neutron		Other Method	
$LiF\text{-}BeF_2\text{-}ZrF_4$	6.94	6.9	6.91	
$LiF\text{-}BeF_2\text{-}ZrF_4\text{-}ThF_4$	6.66	6.63	6.87	
BeO-MgO	19.2	19.4	19.4	19.5
$BeO\text{-}MgO\text{-}ThO_2$	30.4	30	30.1	
Be-Cu alloy	2.04	2.06	N/A	

2.6.2 Structural Metal Analysis

Structural metal analysis were done by a variety of wet chemical techniques. Many different techniques were used for determination throughout the years, with their techniques listed in Analytical Chemistry Division Annual Progress Reports. Out of structural metals, many sources indicate that chromium was determined amperometrically, iron through a O-Phenanthroline spectrophotometric method, and nickel through a Dimethylglyoxime spectrophotometric method [45, 46, 47].

2.6.3 Oxide Analysis

Oxide analysis between 100-5000ppm was found to be one of the most difficult analysis to perform on the salt [48]. No method existed until it was discovered that the reaction between BrF_3 and metal oxides created oxygen gas. However, high temperature reactions were difficult due to the high vapor pressure of BrF_3. It was found that the vapor pressure could be circumvented by introducing BrF_3 into molten KF at around 500°C [48]. To analyze oxide concentration in a salt, a sample was added directly to this molten mixture and oxygen gas was measured through chemical methods. Later improvements by Eklund et al. used a glovebox O_2 meter to more accurately measure oxygen made [49]. Bromine trifluoride does decompose violently on contact with water, so great care must be taken when handling it. Since it is used for reaction with oxygen in the salt it would be in a glove box, and therefore this problem would not present itself.

2.7 Previous Corrosion Testing

Corrosion testing was one of the most important studies done to produce a functioning molten salt reactor. Many alloys were tested in clean salt, dirty salt, coolant salt, fuel salt, and at different temperatures. A lengthy list of salt tests without uranium tetrafluoride was compiled by Williams and Toth [17, 22]. The large majority of alloys tested without uranium were nickel based, using

Alloy-N and Inconel, but some testing was done with 316SS. [50, 51]. Uranium tetrafluoride and thorium tetrafluoride bearing salts were the most focused upon. Many-year corrosion tests were performed using these salts with a large amount of alloys, such as Inconel, Alloy-N, 316SS, 304SS and iron based alloys towards the end of the molten salt reactor program [51]. Results were typical: alloys with higher chromium content experienced greater weight loss with no corrosion control [51]. However, alloys with high chromium, such as stainless steels, could be demonstrated to be compatible with with proper chemical control [50, 51].

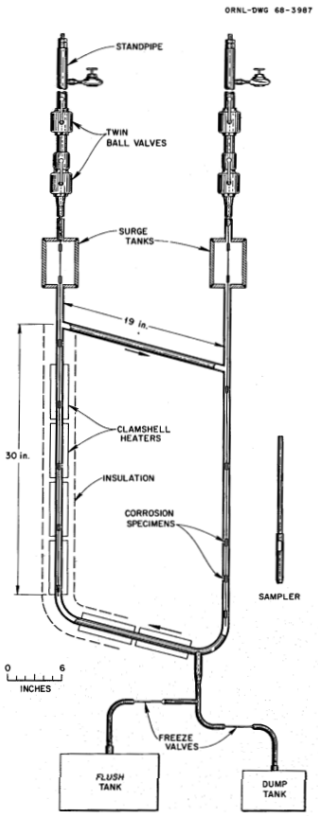

Figure 2.10: A drawing of the typical dynamic corrosion test loop.

Many of these tests were carried out in forced and natural circulation tests containing metallic coupons which would be analyzed later [50, 51]. Tests were carefully designed to prevent any impurity related corrosion. Sample removal systems were designed so that removal could be done through two ball valves and a sliding teflon seal to prevent contamination. In preparation for

corrosion tests the entire system was flushed with clean salt, which absorbed oxides on the surface of the tubing, and then discarded. During tests, a 5 psig atmosphere of helium was kept overhead in order to push contaminants out. By accounting for all of these variables the corrosion depth could be evaluated as a function of salt, alloy, time, and temperature, allowing for a fine tuning of the molten salt reactor's design parameters. If a new fluoride salt cooled reactor is to be built, new corrosion tests will have to be performed with new materials which did not exist during the molten salt reactor program.

Some corrosion testing has been performed with fluoride based salts at the University of Wisconsin to gain more corrosion data and salt experience. Several types of corrosion tests have been designed, each with varying degrees of attention towards impurities and salt chemistry [24, 33, 37].

Olson tested the alloys Hastelloy-N, Hastelloy-X, Haynes-230, and Inconel-617, Incoloy-800H, Ni-201, and Nb1Zr in LiF-NaF-KF [24]. Salt was procured from Electrochemical Systems Inc. near Oak Ridge Tennessee where it was purified using the standard hydrofluorination treatment. Graphite test crucibles and alloy coupon samples were loaded in a glovebox at around 600°C. Sealing was done by TIG welding the graphite's metallic outer shell in an inert atmosphere glovebox. Results found that Ni-201 performed the best while the other alloys ranked in weight loss from least to greatest were Hastelloy-N, Hastelloy-X, Incoloy-800H, Inconel 617, and Haynes 230. All alloys were observed to have their chromium preferentially attacked.

Sellers undertook static corrosion tests of both 316 stainless steel and Hastelloy N alloys at the University of Wisconsin [33]. Tests were performed in 6" tall stainless steel, schedule 10, 2.5" pipe crucibles, without a graphite container [33]. Bottoms and tops for each pipe segment were constructed from laser cut, quarter-inch thick, 316 stainless steel. A stainless steel ring was welded both tops and bottoms to serve as holders for the test coupon rods. Each coupon rod was cut into six inch lengths from quarter-inch diameter, 316 stainless steel rod. Three, half-inch wide, straight cuts were milled at regular intervals perpendicular to the length of the rod. One inch by half inch stainless steel coupons, as well as two inch by half inch Poco AXF5Q graphite coupons obtained

from ORNL, were milled and polished to a mirror finish. Each coupon was labeled according to its material, crucible, and location on its coupon rod. The coupons were attached to the coupon rods using 316 stainless steel wire in order according to Table 2.4.

Table 2.4: Test matrix for the static corrosion tests of flinak salt on 316 stainless steel and Hastelloy N.

Crucible	Crucible Material	Coupon 1	Coupon 2	Coupon 3	Add-In
1	316 SS	Hastelloy N	Hastelloy N	Hastelloy N	N/A
2	316 SS	316 SS	316 SS	316 SS	N/A
3	316 SS	Hastelloy N	Graphite	Hastelloy N	N/A
4	316 SS	316 SS	Graphite	316 SS	N/A
5	316 SS	316 SS	Graphite	Hastelloy N	N/A
6	316 SS	316 SS	Graphite	316 SS	Zirconium
7	316 SS	Hastelloy N	Graphite	Hastelloy N	Zirconium
8	316 SS	316 SS	316 SS	316 SS	Zirconium
9	316 SS	Hastelloy N	Hastelloy N	Hastelloy N	Zirconium

A circular bottom lid was then welded onto a pipe segment. This was done for nine crucibles. Each crucible was the outfitted with its coupon rod and coupons, and then loaded with around 512 g of unpurified flinak salt. Finally, the crucibles were outfitted with a top, which was then welded on, securing the salt, coupon rods, and inert atmosphere. Upon completion, each crucible was removed from the glove box and put into a high temperature oven where it baked at 850°C for 500, 1000, or 2000 hours.

After the baking period, the crucibles were removed from the oven at a temperature of 550°C and immediately flipped upside down. This forced the liquid salt to flow to the top of the container, exposing the sample coupons for easy removal. After cooling, the coupon rods were removed and the crucibles were cut in half to show cross sections of the salt. It was found that visible that the salt in samples 1-5 were much darker than the samples in 6-9. This was due to the addition of zirconium reducing agent in crucibles 6-9.

(a) Cruicble one. (b) Cruicble two. (c) Cruicble three.

Figure 2.11: Cross sections of static test crucibles 3, 5, and 7. Color differences indicate different levels of contaminants which is directly proportional to corrosion.

For analysis coupons were then removed from the coupon rods and cleaned in an ultra sonic bath of which contained one molar aluminum nitrate solution. The aluminum nitrate solution dissolves flinak better than water or other solvents. Once the coupons were clean, they were weighed and dimensioned [33]. SEM images were taken of the sample surfaces followed by cross sectional images. All samples were evaluated for their chemical composition as a function of depth by EDS.

A wide array of interactions were recorded. Certain crucibles were found with dissolved graphite, other crucibles were found with graphite coated with chromium, other crucibles had a layer of zirconium metal alloyed on their samples [33]. Ultimately it was deduced that zirconium could make a huge difference on corrosion with stainless steel, but the amount added must be carefully adjusted for the volume of salt. Additionally, the time it took for zirconium to act was still long enough for certain samples to corrode. Salt would need to be clean before being introduced to an environment with a redox agent in order to minimize corrosion.

The most recent tests at the University of Wisconsin have all been performed in nickel vessels. By using nickel vessels the fluoride ion is largely unaffected, allowing the samples to experience a more unaltered corrosion rate. This is in stark contrast to the stainless steel crucibles previous used, where the fluoride was tied up with the chromium from the vessel itself. The vessel used is

shown in Figure 2.12. The design used a welded stainless steel container for structural stability

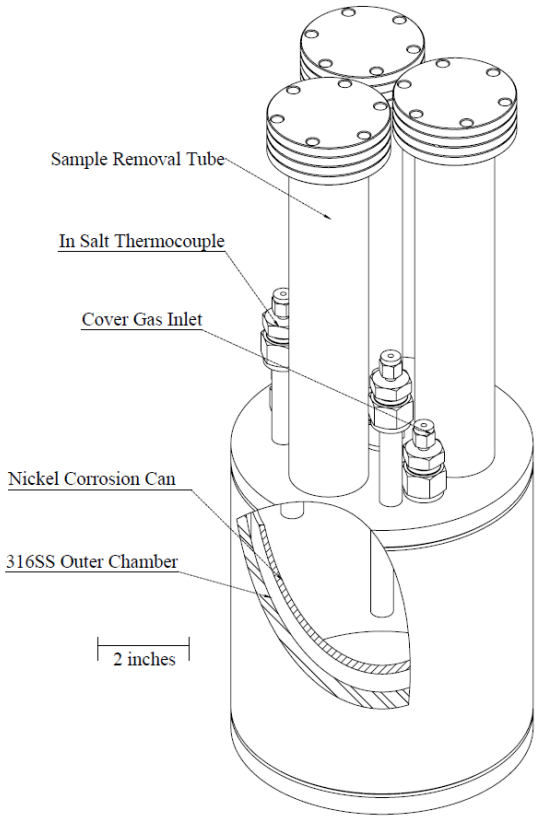

Figure 2.12: The most recent static corrosion test experiment.

while including a nickel vessel on the inside for salt housing. Coupons could be hung and dipped into the salt through three conflat vacuum ports located on the top. This also allowed the samples to be removed periodically at different time periods for analysis. Samples could also be placed on the salt and gas interface. A nitrogen purge was kept on for the duration of the corrosion tests to keep water vapor out during sample removal and usher any off gas from the container. Salts arrived with considerable water and were not purified for this test. The only cleaning action performed was a slow baking and sparge process, designed to drive off as much water as possible from the salt components before melting. The results of the tests were inconclusive for these reasons.

2.8 Hazards

Although fluoride salts are very stable components by themselves, their interaction with the environment can produce chemicals which are detrimental to human life. It is well documented that repeated exposure to vapors or dust from processing beryllium or beryllium containing compounds, such as BeF_2, could cause the onset of Chronic Beryllium Disease (CBD), or more rarely, Acute Beryllium Disease (ABD) [52, 53, 54, 55, 56]. In fact, the phenomena is so well documented that the United States Government produced the Code of Federal Regulations 10CFR850 'Chronic Beryllium Disease Prevention Program' to protect the worker.

Another main hazard, hydrogen fluoride, is a known pulmonary irritant in gaseous form, and in liquidous form a skin and eye irritant [57]. This chemical can be encountered during salt purification, or if certain salts contain large amounts of water, during melting. Its uncontrolled presence will cause severe corrosion. It is one of the few chemicals incompatible with glass and can readily attack nearly all metals. Understanding of these chemical dangers, their interaction, and potential

Figure 2.13: A glovebox used for melting zirconium fluoride salt with unknown amounts of water. The windows were etched by hydrogen fluoride vapor.

for exposure is key to safely working with any fluoride salt.

2.8.1 Beryllium

Beryllium fluoride, BeF_2 is the beryllium salt of hydrogen fluoride. It appears as a glassy, semi translucent, chip. It is highly hygroscopic and dissolves readily in water, albeit at a slow rate [55]. Its density is 1.986 g cm^{-3}. As supplied to the University of Wisconsin by Materion, it appears speckled with carbon–shown in Figure 2.14. It is is a direct precursor in the manufacture of beryllium metal [55]. This is performed by its reduction with magnesium metal at temperatures around 1300°C by

$$BeF_2(l) + Mg(s) \rightarrow Be(s) + MgF_2(l). \tag{2.46}$$

The beryllium precipitates from this reaction as a pebble; facilities producing beryllium through these means are refered to as 'pebble plants'. Other beryllium halides, such as $BeCl_2$ have the ability to be reduced by metallic agents to yield pure beryllium metal, they do not have the required high boiling points.

The main source of potential danger from beryllium fluoride is through inhalation of small particles or dust. Beryllium and beryllium containing compounds are capable of causing a long term chemical pneumonitis, or CBD.

> "Chronic beryllium disease (CBD) is a granulomatous lung disease that is caused by the body's immune system response (similar to an allergic reaction) to inhaled dust or fumes containing beryllium metal, alloys, beryllium compounds or mixtures, or insoluble beryllium salts. The body's immune system response to beryllium is often called beryllium sensitization. Beryllium sensitization precedes the development of CBD. Sensitization can occur quickly or many years after exposure to beryllium," [52].

CBD ultimately makes it more difficult for the lungs to get oxygen to the bloodstream and body.

Figure 2.14: Picture of as received beryllium fluoride from Materion.

Frequently reported symptoms include one or more of the following: dyspnea (shortness of breath) on exertion, cough, fever, night sweats, and chest pain and, less frequently, arthralgias (neuralgic pain in joints), fatigue, weight loss, or appetite loss [52]. On physical examination, a doctor may find signs of CBD results, such as rales (changes in lung sounds), cyanosis (blue coloration of skin due to lack of oxygen), digital clubbing (fingernail deformity), or lymphadenopathy (enlarged lymph nodes). An X-ray of the lungs may show many small scars. Furthermore, examination of the lung tissue under the microscope may show granulomas, which are signs of damage due to the body's reaction to beryllium [52]. Beryllium fluoride falls under the category of water soluble beryllium salts which, according to Materion:

> "Water-soluble beryllium salts are strong irritants and capable of causing acute inflammatory reactions of the respiratory pathways and chemical pneumonitis upon inhalation. Inhaling particulate containing beryllium may cause a serious, chronic lung disease called Chronic Beryllium Disease (CBD) in some individuals," [53, 54].

Recently, cases have been documented which describe the acute onset of chemical pneumonitis

in two workers who were involved in the melting of beryllium fluoride at a pebble plant. Case one describes a healthy 20 year-old male nonsmoker with 120% (6.34 L) of the predicted functional residual capacity (FVC) at the time of his hiring [56]. Within ten months the worker's lung capacity had decreased to 68% (3.61 L) of the predicted FVC [56]. Case two describes a 25 year-old male smoker with 115% (5.33 L) of the predicted FVC beginning work at the beryllium fluoride furnace. Within two months case two had a lung capacity of 72% (3.36 L) of the predicted of the predicted FVC [56]. Both cases experienced abnormal beryllium blood results after their poor lung performance tests [56]. Prior to both case's decrease in lung performance they experienced new skin rashes which they reported to their health office [56]. Eventually, case one left the plant in 1991 due to CBD; case two followed shortly after in 1992. It should be noted that both cases were exposed to predominately beryllium fluoride vapors, but there also was potential for exposure to beryllium hydroxide, beryllium oxide, beryllium, ammonium beryllium fluoride, and ammonium fluoride. Only the last two would not be found in a reactor containing flibe.

There is no known medical treatment which has been proven to cure chronic beryllium disease [53].

> "Prednisone or other corticosteroids are the most specific treatment currently available. They are directed at suppressing the immunological reaction and can be effective in diminishing signs and symptoms of chronic beryllium disease...Other symptomatic treatment, such as oxygen, inhaled steroids or bronchodilators, may be prescribed by some physicians and can be effective in selected cases," [53].

Beryllium disease has to be prevented before it develops, therefore many diagnostic tools have been developed, one being measurements of sensitivity.

Prior to the development of chronic beryllium disease it is believed patients become sensitized to beryllium, meaning that their body's disease-fighting blood cells, called lymphocytes, react negatively in the presence of beryllium [58]. Individuals sensitized to beryllium are asymptomatic

and not physically impaired. Once sensitization has occurred, it is medically prudent to prevent additional exposure to beryllium as further exposure could accelerate the development of CBD [52]. Beryllium sensitization can potentially be tested for by a blood test called the Beryllium Lymphocyte Proliferation Test (BeLPT). Medical experts believe that the BeLPT will test positive for individuals who have become sensitized to beryllium [58].

> "Studies have shown that practically all individuals with CBD also are sensitized. On the other hand, many individuals that are sensitized to beryllium do not have CBD...[A sensitized] individual is more likely than others to get CBD but the individual may never get CBD or may get a mild case of CBD especially if the individual's exposure was low," [58].

In order to prevent CBD, many strict standards for air quality and cleanliness have been established by industrial hygienists through many years of well documented beryllium exposures. These standards are shown in Table 2.5. The common upper value which is referenced as average

Table 2.5: Airborne beryllium working conditions [59].

	OSHA			California OSHA		NIOSH
	PEL	CEILING	PEAK	PEL	CEILING	REL
Beryllium Concentration (μg m^{-3})	2	5	25	0.2	25	0.5

PEL = Eight-Hour Time Weighted Average Permissible Exposure Limit (OSHA)
OSHA CEILING = Not To Be Exceeded Except For Peak Limit (OSHA)
Cal OSHA CEILING = Not To Be Exceeded At Any Time (California OSHA)
PEAK = 30-Minute Maximum Duration Concentration Above Ceiling Limit (OSHA)
NIOSH = National Institute for Occupational Safety and Health
OSHA = Occupational Safety and Health Administration
REL = Eight-Hour Time Weighted Average Recommended Exposure Limit (NIOSH)

for a eight-hour time weighted average permissible exposure limit is 2 μg m^{-3}. Many beryllium workplaces such as Materion and Lawerence Berkeley National Laboratory keep there airborne concentrations at 0.02 μg m^{-3}. Although these standards are very low, they can be reasonably

achieved, even in locations which machine pure beryllium metal, as shown in Table 2.6. It can bee

Table 2.6: Personal sampling for beryllium exposure at two DOE Sites [52].

Oak Ridge Y-12 Plant	1980 to 1989	1990 to 1996
Number of Samples	148	1448
Estimated Arithmetic Mean Level of Exposure	0.9 μg m^{-3}	0.3 μg m^{-3}
Percent of Samples Less than 2 μg m^{-3}	94%	98%
Rocky Flats Beryllium Machine Shop	1984 to 1985	1986
Number of Samples	99	279
Estimated Arithmetic Mean Level of Exposure	1.19 μg m^{-3}	0.035 μg m^{-3}
Percent of Samples Less than 2 μg m^{-3}	84%	99.6%

seen large percent of air sampling was below 2 μg m^{-3} as time went on. Complimenting the air quality statistics are the numbers detailing the health of the workers at the same plants. Over these years, a large sample size of workers had their health analyzed, shown in Table 2.7. One of the

Table 2.7: Cases of beryllium sensitivity and CBD at two DOE sites[52].

	Rocky Flats	Oak Ridge Y-12
Individuals Examined	6257	1949
Abnormal Be-LPT Number (%)	221 (3.5%)	77 (4%)
Completed Diagnostic Exams	186	33
CBD Number (%)	79 (1.3%)	25 (1.3%)

most important conclusions is that even with the high standard of air quality required by these two locations, roughly 3-4% of people still had abnormal BeLPTs, and 1.3% of people still managed to get chronic beryllium disease. It is important to note that these employees only worked with beryllium and beryllium oxide compounds. No large scale study has been performed on the health effects of constant exposure to beryllium fluoride. As there exists no study to prove that beryllium fluoride's toxicity relative to beryllium, it was treated as beryllium and the same standards were kept. It would be prudent to establish health standards for beryllium fluoride based on air quality and health reports if large amounts are ever used outside the presence of beryllium metal.

Beryllium fluoride is also known to create a dermal response.

> "Soluble beryllium compounds pose a potential for an allergic dermal response. This material poses a potential for contact dermatitis of both the irritation and allergic type. Introduction of this compound into open wounds may result in a severe long-term ulceration," [53].

Negative effects exist due to exposure to the eyes and ingestion, but these are mild and are common to many other fluoride compounds [53, 54]. Therefore, the most care is given to the accident inhalation of beryllium containing compounds.

2.8.2 Anhydrous and Aqueous Hydrogen Fluoride

In contrast to beryllium, anhydrous and aqueous hydrogen fluoride are very acute hazards. Anhydrous hydrogen fluoride is a liquid with a variable concentration gaseous head capable of causing severe, immediate burning. Aqueous hydrogen fluoride exists in the form of up to 70% by weight in water and may not be immediately noticeable after contact. The aqueous version is extremely soluble in concentrations up to 70%, after which it readily produces vapors and is referred to as fuming hydrogen fluoride. Contact with hydrogen fluoride should be avoided at all costs–burns larger than 25 square inches may result in serious injury, amputation, or death. The routes of exposure are through inhalation, skin contact, or swallowing. Permissible air quality levels for a 8 hour work shift is 3 ppm, or 2 mg m^{-3} of hydrogen fluoride, although detection levels have been recorded between 0.04 to 3 ppm [57].

Hydrogen fluoride burns are so severe due to the mobility of the F^- ion which can move through the skin until contact is made with calcium and magnesium in the bones, binding them up and halting important metabolic processes [60]. Without treatment, skin destruction can continue for days eventually leading to permanent damage, disability, or even death. Exposure to concentrated vapors are often immediately noticeable, causing a deep, throbbing pain from destroyed nerve

endings[60]. Regardless of the burn concentration or area immediately medical attention is needed.

To treat an hydrogen fluoride burn several steps must be taken. First, if the area is safe, the victim should be removed from the source of hydrogen fluoride. If the sole route of exposure is through the skin, immediate treatment can begin. The first treatment should be rinsing area for around ten minutes in water. While washing, 911 should be called. If help has not arrived after rinsing, calcium gluconate gel should be applied to the area with a gloved hand. Any personnel who has access to a hydrogen fluoride lab should know where this gel is located and how to apply it. Gel should be applied until help arrives. If the route of exposure is through the lungs, the victim should be moved to fresh air while emergency services should be called. To treat such an exposure, pure oxygen can be administered along with nebulized calcium gluconate at a hospital.

The immediate dangers of hydrogen fluoride should be known by all fluoride salt employees. All unknown liquid which has been in contact with molten salts at high temperature should be treated as it contains hydrogen fluoride. All off gas which has been in contact with, or sparged through, molten salt should be assumed to be acidic unless proven otherwise. Any water which has contacted this off gas should be assumed acidic as well. Salt should never be immediately melted after extensive water contamination, and should be slowly baked off. Neutralizers and pH indicator should be in all labs. Proper PPE, such as a full face respirator and thick rubber gloves should be worn at all times. Before attempting any maneuver where hydrogen fluoride is used, great attention needs to be payed towards the amount of hydrogen fluoride produced, and its resting location. Water can easily, come to fuming concentrations if allowed. Lastly, production greater than 1L of aqueous hydrogen fluoride at any concentration should avoided due to the difficulty of disposal. Handling such a large quantity creates an extreme splash hazard during handling and takes an excessive amount of time to neutralize due to heat production.

Chapter 3

Experimental Design and Operation

3.1 Purpose and Ultimate Use

In order for the University of Wisconsin - Madison to perform corrosion tests on par with those performed at ORNL there must be access to large amounts of pure fluoride salts. There exists no facility in the the world which can provide pure salts at the needed quantity, schedule, and price. Therefore, it had to be built.

3.2 Oak Ridge Fluoride Salt Production Facility

Since there was no commercial source of flibe during the MSRE, all the salt at ORNL had to be produced on site. Between the MSRE and the ARE, 72,000 kg of fluoride salts were produced in batch sizes of about 2 ft^3 from commercially available sources [5]. To fill both the primary and secondary loop of the MSRE, around 200 ft^3 of salt were required [5]. Isotopically pure lithium-7 fluoride was obtained from the Y-12 plant on site. Beryllium fluoride was procured from a major beryllium manufacturer as an intermediary product to beryllium metal [5].

To produce and purify flibe, each constituent was weighed and loaded on a hopper inside of an atmospherically controlled room by a scientist in a plastic fresh air suit. The air inside of the room cycled through a filtration system three times per minute. These extreme safety measures were taken in order to assure that employees would not be exposed to elevated levels of beryllium, which can cause chronic or acute beryllium disease.

The hopper then transferred salt into a 6', 12" OD IPS, stainless steel 304L preliminary treatment vessel lined with 1/8 thick commercially pure, nickel 200. Next, the salt was melted and then sparged with an argon-hydrogen mixture. The heat and gas sparge worked together to remove

water from the salt. This pretreated salt was then moved to the primary chemical reactor, which was of similar construction to the introductory vessel. The rest of the process is detailed in Section

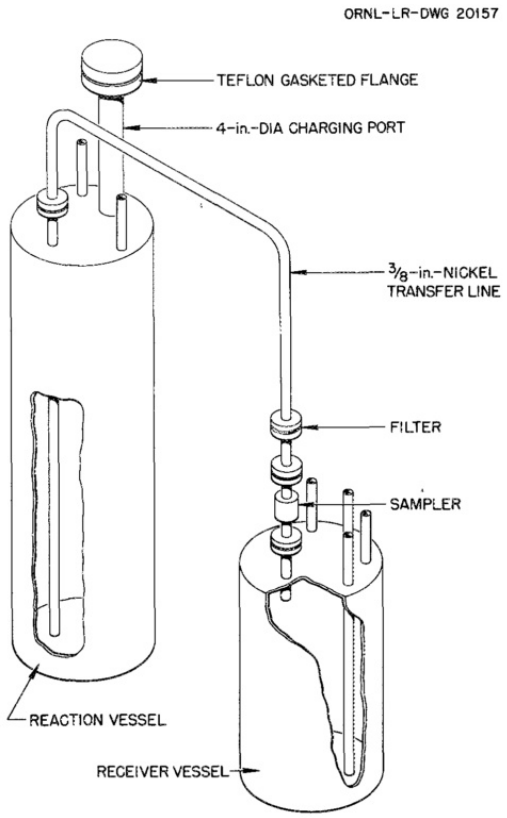

Figure 3.1: The ORNL batch fluoride salt purifier.

2.5 and will not be detailed here.

3.3 Wisconsin Purifier Materials Selection

Many materials were selected for use in the purification unit for their corrosion resistance, strength, electrical conductivity, available form, price, and maximum temperature. These materials are shown in Table 3.1. A large amount of literature on these materials exists. It is not within the scope of this thesis to discuss each one and the properties which allow them to be used.

Unfortunately, Hastelloy-N alloy, and other high temp nickel molybdenum alloys, is not made

Table 3.1: A complete list of materials used to construct the University of Wisconsin fluoride salt purification system.

UNS Number	Trade Name	Max Temperature (°C)	Usage
N02200	Nickel	850	Molten salt containment, high temperature hydrogen fluoride and water vapor.
N04400	Monel	300	Mixtures of water vapor and hydrogen fluoride.
N07750	Inconel X-750	704	High temperature spring.
N06625	Inconel 625	850	Wrap around heaters.
N06003	NiChrome	1200	Trace heating.
S31600	316 Stainless Steel	550	Anhydrous hydrogen fluoride introduction. MSRE canister.
S10xx0	Mild Steel	-	Structural support.
A96105	Extruded Aluminum 6105	-	80/20 support structure.
C71500	Copper Nickel	-	Long term salt storage.
C10100	Pure Copper	-	Heater leads.
-	Braided Graphite	450	Sealing flanges.
-	Mica Sheet	1000	Wrap around heater electrical insulation.
-	Kaowool	1260	Base insulation on trace heaters.
-	Pyrogel XT	650	Outer insulation.
-	Microtherm Board	1000	Rigid insulation board.
-	Microtherm Pour	1000	Insulation in tight locations or complex geometries.
-	Perpluoroalkoxy	260	Flexible, low temperature corrosive gas routing.
-	High Density Polyethylene	110	Carboy scrubbers and containment walls.

in the forms required for use in the purification system. Currently, only thin sheets are available. These sheets would not need meet the strength needs for a purification unit. If thicker gauge sheet, or plate, was produced by Haynes, it might be desirable to use this as a storage medium. A second smaller problem exists: lack of tabulated isochronous stress strain curves for these alloys, in different forms, as stated by the American Society of Mechanical Engineers. Without these numbers, safe and reliable engineering cannot be guaranteed with Hastelloy alloys. Therefore, pure nickel would still be advised for the purification vessel.

3.4 Wisconsin Fluoride Salt Production Facility

The Wisconsin Fluoride Salt Production Facility (WFSPF) was designed to purify salts to MSRE standards while producing batches large enough for experimentation and large scale testing. It has roughly half the capacity of the MSRE purifier. Many of the same features found in the MSRE purification facility were used in the WFSPF such as a negative pressure beryllium room, a nickel purification vessel, high temperature filtration, and a salt storage vessel.

Despite the WFSPF system incorporating many key parts of the MSRE design, a few changes were made. Instead of just lining a stainless steel canister with nickel, the entire purification vessel of the Wisconsin purification vessl is constructed from quarter inch thick nickel. This was done in anticipation of using ultra-corrosive fluorine based gases for salt purification. Instead of using a stainless steel exoskeleton as in the MSRE purification facility, the Wisconsin purification vessel uses pressure matching with a larger stainless steel vessel to remove stress from the nickel canister– this is expounded upon in Section 3.4.4. To melt and cool salt quickly, the MSRE purification used moving ceramic heaters. These heaters were attached to a pulley and counter weight system which would drop away exposing bare metal to cool. The Wisconsin purification system uses electric resistance heaters strapped to the vessel with layers of insulation around the outside. This increases cooling time.

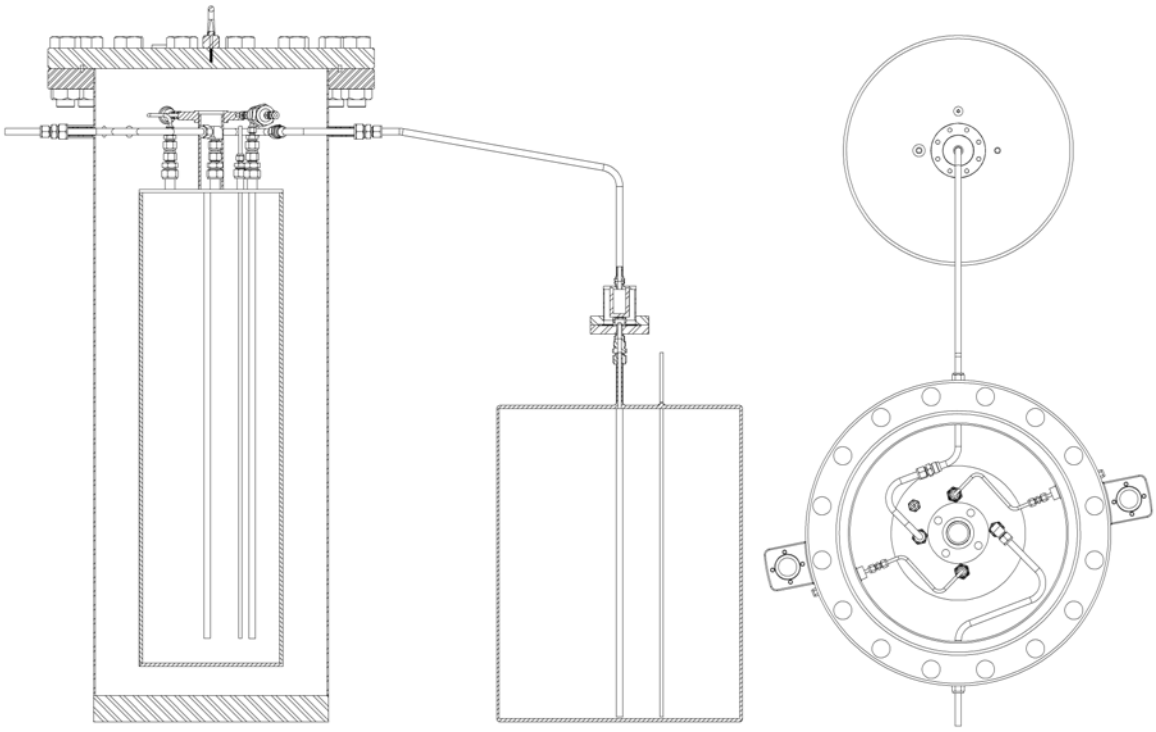

(a) Side view of the purification system with copper nickel recieving vessel and filter.

(b) Top view of the purification system with tube routing visible.

Figure 3.2: The salt vessels for the WFSPF.

3.4.1 Walk-in Fume Hood and Safety Systems

To mitigate the risk associated with with beryllium work, a negative pressure walk-in fume Hood was designed to contain beryllium dust. The room measures roughly 9'× 12' with a 10' tall ceiling. The room is large enough to contain the purification system as well as a full line of corrosion tests. The room's structural support comes from 2"× 2" carbon steel tube. Each tube is anchored into the wall or floor using bolts which go through pre-drilled holes in the tube and into concrete anchors. The load on the anchors is purely shear, allowing them to secure considerable load. To further add to the structural strength and rigidity of the structure's frame, each piece of carbon steel tube was welded at the seams, creating one solid, box entity.

After the frame pieces were bolted to the wall and welded together, cross beams were posi-

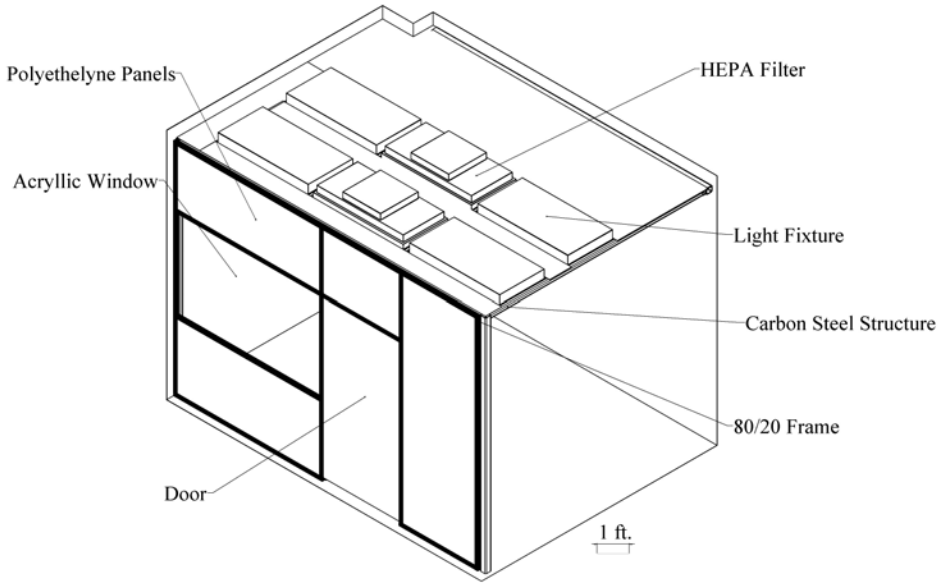

Figure 3.3: A CAD drawing of the walk-in in fume hood.

tioned every 48”, extended to the front of the of the room from the back of the room. These beams added extra structural support, but also served as attachment points for frame boxes. Frame boxes were made by cutting 1”× 1”× 1/8” carbon steel angle and welding them together to form a rectangular resting place for lighting fixtures and HEPA filters. After the positioning of the frame boxes, 0.060” carbon steel sheet was sheared to size and welded into the gaps between frame boxes and the frame to serve as the room. The structure was then painted white.

To complete the front wall of the room 80/20 aluminum was used. 80/20 is a versatile extruded aluminum construction system which uses T-slotted beams and slide in connector parts for attachment and support to other pieces of 80/20. 80/20 comes with diverse accessories which allow for its use in many applications. On top of these, it is lightweight, quick to cut, and requires minimal machining. 80/20 was incorporated into the carbon steel frame through the addition of quarter inch bolt holes drilled through the carbon steel frame. 80/20 was positioned on one side of the frame and bolts were inserted through the other side, into T-slotted nuts in the 80/20. The 80/20’s main purpose was to receive quarter inch thick high density polyethylene (HDPE) and quarter inch thick clear acrylic. These pieces of plastic were thin enough to slide into the T-slots with ease, but

structurally sound enough that they would not crack or bow over time. This was important; seals between the plastic and the 80/20 have to remain tight for the whole operational lifetime in order to prevent the release of beryllium dust.

Figure 3.4: The room in the initial stages. Cross beams were MIG welded.

The sheets of HDPE and acrylic were purchased from local plastic suppliers and cut to size. A piece of 80/20 was placed in between each sheet of plastic to surround it on all four sides. Once all the pieces of 80/20 were bolted into the carbon steel and the plastic was in between pieces of 80/20, connectors were screwed into which joined pieces of 80/20 together at angles. This added strength the 80/20 structure at its joints. To complete the structure, a door was constructed from 80/20 and a quarter inch thick sheet of aluminum. Aluminum was chosen due to its superior strength as compared to plastic; if the door slammed shut or was hit while moving things in it out it would not crack. The aluminum was sanded with an orbital welder to give it a matte look. The whole sheet was then surrounded by 80/20 which was then joined together using connector plates. An aluminum handle was added and was attached to the main 80/20 through the use of heavy duty hinges.

To create strong seals in the room several techniques were used. First, any holes in the structure which existed from pipe and electrical feed-throughs were filled with a gap-sealing spray foam insulation which expanded into the hole and hardened after twenty four hours. To fill in smaller holes silicone caulk was used. Locations that were ideal for this treatment were the interfaces of plastic and aluminum, aluminum and carbon steel, and carbon steel with the wall. The last technique used to create a strong seal was the implementation of gaskets. Panel gaskets, purchased from 80/20, were shoved between the 80/20 and the plastic in order to create a tight seal which was complemented with caulk. These gaskets also served a secondary purpose by eliminating panel rattling.

Figure 3.5: The complete walk in fumehood.

To create a negative pressure with airflow inside of the structure, ductwork was added to the top which connected a large fume fan to the HEPA filters on the inside. The fan is capable of moving 1625 cubic feet of air per minute which then exhausts to the outside of the building. A grated air inlet was installed to the outside of the fume hood, allowing for air inflow and constant movement into the HEPA filters while inside the room, even with the door closed.

3.4.2 Purification Vessel

The purification vessel was constructed out of quarter inch nickel 200/201 sheet which was rolled into a tube 36” tall and 11” in outer diameter. This created a vertical seam between both of the edges. To join these seams, a multi-pass TIG weld was done. Preparation for the weld involved cleaning, polishing, and grinding the meeting edges down to a 45° angle. This provided a crevasse for the introduction of filler material for a weld. Additionally, a copper backing bar with a gas line machined down the center was attached to the back of the weld joint in order to spread the heat from the weld and introduce argon gas to the back of the weld. This insures a more corrosion resistant weld. The root pass is shown in figure 3.6.

Figure 3.6: The root pass of the nickel purification vessel.

Two more passes were put over the root pass to ensure a strong, corrosion resistant joint. After the tube was welded together, a laser cut bottom was attachedagain using three passes to ensure a good seal. At this point, the nickel vessel had the form of a cup. At this point the nickel was chemically treated with Oakite® 33, a pickling solution , to to remove dust, grime, and unwanted metallic build up from machining and welding. After the cleaning, the nickel was washed with

water to remove any remaining acid or contaminants.

Figure 3.7: The nearly completed nickel purification vessel.

After the inside of the vessel was thoroughly cleaned the lid was machined. Six holes were positioned in the top. First, a 1.9” diameter hole was placed in the center of the lid. This would serve as the charging port hole. Next, four 3/4” inch holes were placed in a circular pattern around three inches away from center. These holes would accept a tube stub which would be used to insert a secondary tube for gas sparge, salt transfer, effluent stream, and diagnostics. Finally, a 1/4” inch hole was positioned in between two of the 3/4” holes in order to insert a thermocouple well. To complete the lid, a pair of flanges were machined from a five inch nickel bar. The flanges were ANSI NPS 1.5” in order to accept standard gaskets from numerous high temperature vendors. The flange system was welded on to the 1.5” NPS nickel pipe which was then welded on to the nickel lid along with all the corresponding tube stubs. Lastly, the complete lid was welded to the tube

using three passes.

3.4.3 Small Purification Vessel

A large scale purification was sometimes not needed to provide enough salt for tests. Therefore, a small scale nickel vessel capable of holding a maximum of 1000 g, or 500 g of salt with a splash head, was constructed. The nickel vessel is shown in figure 3.8. The body was constructed out of

Figure 3.8: The small nickel purification vessel used for the purification of the MSRE flibe.

nickel 200/201, 2.5” NPS, schedule 10 pipe, stands 6-3/4” tall with a 3/8” lid and bottom. The lid has four holes: a 1/4” dip tube and thermowell and two 1/2” outer diameter rabbit ears which were used for gas inlets and outlets and for salt inlets and outlets. Half-inch line was chosen in order to prevent clogs from vapor, and they were angled to allow transferred salt to roll in. Both 1/2” tubes were flush with the bottom of the top cap; only the thermowell and dip tube went to the bottom.

Most ports were multipurpose. The dip tube was used for both salt transfer and sparge, the

half inch tubes were used for effluent and transfer. This multipurpose capability required that all swaged on connections were of Monel construction. However, the multipurpose use sometimes allowed the use of non-Monel bodies. For instance, for salt transfers from the MSRE canister, 316 stainless steel fittings were allowed on the half inch tubing, however this same line was sometimes used as an effluent. In the case it was used as effluent, a Monel body was used.

Heating was done by two 4', 240VAC heating tapes. One tape was positioned at the top, the other was placed at the bottom. This can be seen in Figure 3.8. Two trace heat zones made of spiral wrapped nichrome wire were added to the concentric 1/4" line as well as one of the 1/2" lines. One welded thermocouple was used for each zone control. Insulation was standard: one layer of kaowool, followed by two layers of Pyrogel XT; However, the bottom of the small nickel purifier was insulated with two inch microtherm board.

3.4.4 Support Vessel

The purification vessel made out of alloy 200/201 is extremely soft at high temperature and would not be able to withstand any pressure greater than a few PSI without deformation due to its size. To circumvent this problem a 304 stainless steel exoskeleton was positioned around the nickel with the ability to pressurize and vent. If the purification vessel was to pressurize or de-pressurize, the support vessel would respond accordingly through the use of a Dwyer differential pressure gauge and switch . Pressures would be able to be controlled within one PSI without the switches cycling excessively.

To build the stainless steel support vessel, a 48" tall, 18" NPS pipe, TIG welded to a 2.5" thick, 321 stainless steel, waterjet cut bottom. From there, a ANSI B16.5, 150#, NPS 18 slip on flange was tacked on the outside to the pipe, and then two full passes were done on the inside seam of the flange in order to create a strong seal. From there, several holes were drilled around the pipe. The purpose of these holes was for various feedthroughs of tubing for salt, gas, electrical leads,

Figure 3.9: The stainless steel support vessel with the nickel purification vessel in the background for comparsion.

or thermocouple wires. Each one of these feedthroughs was completed with a welded tube stub. Lastly, the lid was tapped and a screw in hoist ring which served as the anchor for lifting of the 200 pound lid. The final product is shown in Figure 3.9.

After completing the purification and receiving vessel heating and thermocouple systems, to be described in Section 3.4.10, the purification vessel was moved into the high bay laboratory with its stainless steel counterpart. The high bay lab has a five ton crane which was used to carefully lift and place the nickel purification vessel inside of its stainless steel shell, shown in figure 3.10.

3.4.5 Storage Vessel

Two storage vessels were produced for storing purified salt. For the first tests runs of the purification experiment the receiving vessel used was constructed out of alloy C71500, a mixture of 70% copper and 30% nickel. Copper is thermodynamically predicted to perform more favorably than nickel in the salt, but copper also has much poorer oxidation resistance. It was thought that if the

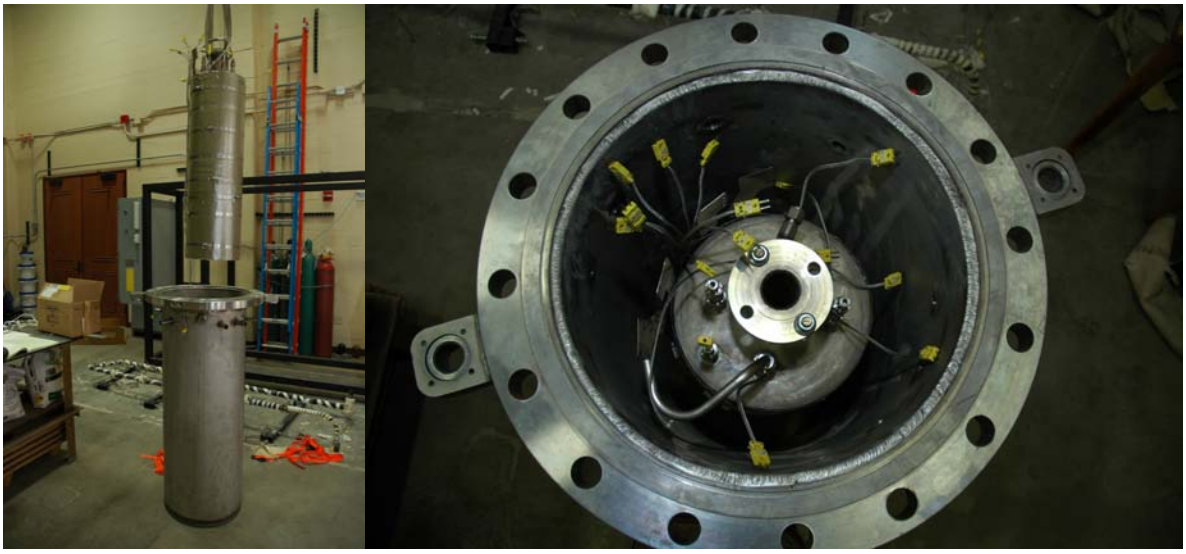

(a) Lifting the purification vessel into position

(b) The purification vessel nested inside of the stainless.

Figure 3.10: The loading process of the purification vessel.

alloy's performance was good it could be used as a cheaper alternative than nickel based alloys for non-critical, high temperature fluoride salt containment.

The container was constructed from a 12-13/16" pipe of C71500 alloy which was topped with two waterjet cut, 1/4" lids. One lid was machined to have three holes for 1/4" NPS C71500 pipe to go through as well as one 1/4" hole. The pipe was selected over tube solely due to size availability; 1/4" NPS corresponds to an outer diameter of 0.540". The three pipe holes were designed for salt receiving, salt transfer, and the effluent stream while the quarter inch hole was used for a thermocouple well. Both lids were welded on using three passes each with C71500 filler.

3.4.6 Salt Filtration

After salt is purified, metals exist in suspension with the salt. These metals can be primarily removed by decantation, but an in line salt filter is also needed to thoroughly clean the salt. The best time to do this is during transfer from the purification vessel to the receiving vessel.

The filter has six components: the bottom flange and cup, the top flange, a nickel gasket, the actual salt filter, a stage, and a Belleville spring. The filter itself is a 2” outer diameter welded cup design made of woven stainless steel mesh filter with a 25 micron rating by Porous Metal Filters. The filter plugs into a groove which is inlayed into the bottom of the welded filter assembly. After

(a) The porous metal filter and other dissasembled components

(b) The assembled filter with VCR® connections exposed.

Figure 3.11: The molten salt filter.

the filter has been plugged in, a Belleville disc spring is placed on top of it, followed by the stage. The stage fits into a groove machined into the blank flange. As the two flanges compress on the gasket placed in between them they simultaneously load the disc spring, keeping the filter in place. All materials were constructed out of 316 or 304 stainless steel except for the gasket which was made out of Inconel X-750.

The filtration unit can be disassembled completely, cleaned, and will also leave behind a thin wafer of the final salt for chemical analysis. Additionally, its VCR connections allow it to be removed directly from its line without removing other tubes.

3.4.7 Effluent Stream and Caustic Scrubbers

Not all of the hydrogen fluoride gas reacts with the salt during the purification process–some of it is absorbed into the salt and some passes through. In some instances, there may be water vapor in this mixture. Hydrogen fluoride can not be directly exhausted through the building and must be disposed of in some way. Initially, three HDPE carboys, shown in Figure 3.12, were set at the

Figure 3.12: The carboy system for removing unwanted hydrogen fluoride.

tail end of the effluent stream to capture the hydrogen fluoride. The first in line was a 9L carboy with two quarter inch Monel Swagelok bulkhead fittings. The last two in line were 20L carboys each with two quarter inch Monel Swagelok bulkhead fittings. The inlet fitting was outfitted with a submerged Monel diptube. Each 20L carboy was filled with approximately 14L of water. It was thought that these final two 20L carboys would be able to absorb the highly water soluble hydrogen fluoride. Upon investigation, it was found that while the water would absorb the hydrogen fluoride, any water in the effluent stream would deposit in the first empty carboy and then saturate itself with hydrogen fluoride, potentially reaching 70% concentration over the course of a purification. At this concentration, the hydrogen fluoride is able to fume off of the liquid. Therefore, it was decided

that the carboys would have a neutralizer in them.

Selection of the hydrogen fluoride neutralizer was difficult. A neutralizer must be able to dissolve in water in concentrations to neutralize all escaping hydrogen fluoride, it must have a heat of reaction which is not capable of melting the HDPE containers, and it must produce relatively safe compounds. Seven molecules were recommended for use by Honeywell Chemicals and are shown in Table 3.2.

Ultimately, three molecules were examined for use: Na_2CO_3, NaOH, and $NaHCO_3$, each neutralizing to form NaF:

$$Na_2CO_3(d) + 2HF(g) = 2NaF(s,d) + H_2O(l) + CO_2(g);\ \Delta H = -18.5\ \text{kcal} \cdot \text{mol}^{-1}\ \text{of HF}, \quad (3.1)$$

$$NaOH(d) + HF(g) = NaF(s,d) + H_2O(l);\ \Delta H = -39.0\ \text{kcal} \cdot \text{mol}^{-1}\ \text{of HF}, \quad (3.2)$$

$$NaHCO_3(d) + HF(g) = NaF(s,d) + H_2O(l) + CO_2(g);\ \Delta H = -7.6\ \text{kcal} \cdot \text{mol}^{-1}\ \text{of HF}. \quad (3.3)$$

The final factor in determining the correct neutralizer to use was the enthalpy of reaction. All of the neutralizing reactions release heat, therefore the reaction in the carboy had to be checked to insure that it would never reach a temperature where it would boil, soften the HDPE, or in a worst case, melt the HDPE. To do this, the hypothetical situation of all the hydrogen fluoride passing through the molten salt without reaction was examined. It should be noted that numbers which are calculated in Section 3.7 will be used without background explanation here.

In the case of a full purification run with 50 kg of flibe roughly 300 moles of hydrogen fluoride will be flown, or 7600 L, at 500 mL min^{-1} maximum. The neutralizer will have to react with all of excess hydrogen fluoride. Depending on the reaction, this would require between a half a mole

Table 3.2: Neutralization agents and their reaction products and hazards as listed from Honeywell Chemicals.

Neutralizer	Water Solubility (g/L)	Reaction Hazards	Product Salt	Product Solubility (g/L)
KOH	1210	High heat of neutralization and dilution.	KF	1020
NaOH	1110	High heat of neutralization and dilution.	NaF	40
Na_2CO_3	215	Rapid release of CO_2 gas.		
$NaHCO_3$	96	Rapid release of CO_2 gas.		
$CaCO_3$	0.013	Slow reaction; Surface passivization.	CaF_2	0.016
CaO	1.19	High heat of neutralization and hydration.		
$Ca(OH)_2$	1.73	High heat of neutralization.		

to a mole of neutralizer per mole hydrogen fluoride. To determine the temperature change caused by the neutralization all that was needed was the heat transfer coefficient, h of the carboys. To find this, a specific volume of hot water was added to the container. By recording its temperature over time, its heat loss could be calculated through knowledge of the volume and specific heat through the equation

$$\Delta Q = mc_p \Delta T. \tag{3.4}$$

This ΔQ was then used to determine h through

$$h = \frac{\Delta Q}{A \Delta T} \tag{3.5}$$

The area, A, was measured as roughly 0.5 m^2, resulting yielding h around 7 $Wm^{-2}k^{-1}$. Through the use of energy balance, a time dependent temperature profile for each neutralizer was made using these worst case conditions, shown in Figure 3.13. The maximum temperature of the HDPE is around 100°C, therefore all neutralizers will work without excessive heating during any flow rate.

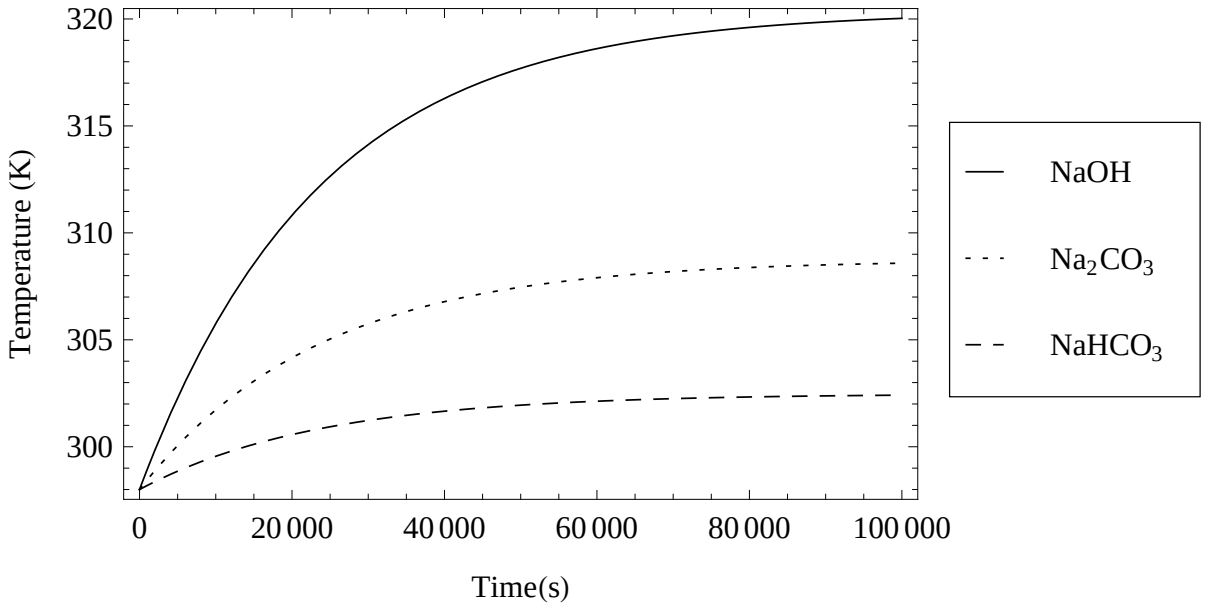

Figure 3.13: Neutralization temperature profiles in the large carboys over time.

Consequently, the final determination for correct neutralizer selection is dependent on dissolution. Sodium bicarbonate has the lowest solubility of all the three listed neutralization agents, therefore it was scraped. The choice between NaOH and Na_2CO_3 is not as obvious. NaOH does produce highly caustic solutions if dissolved to its limit, but is the only neutralizer which can take care of the worst case scenario with one large, 14 L carboy. To decrease the amount of caustic solution needed it was decided on a mix of NaOH and Na_2CO_3, with residual Na_2CO_3 powder on the bottom of the carboy. As the hydrogen fluoride flows, it will react, and stir up the undissolved Na_2CO_3 powder, continuously allowing it to interact with the hydrogen fluoride. In the case that this does not happen, the third carboy will undoubtedly remove all the hydrogen fluoride.

3.4.8 Electronics

The purification experiment requires large amount of electronics to function. Shown in Figure 3.14, the electrical enclosure was the way of organizing, controlling and powering all the equipment which would be used for the salt purification. The core of the box revolves around its heater

control systems. This all done by fourteen DC solid state relays (SSR) and two AC SSRs which are shown on the top row with red wire and in the middle row with blue wire. The first three SSRs are attached to a variable voltage, 150 A power supply which is used to power the three main heater zones on the purification vessel and on the receiving vessel. The following eleven SSRS are hooked up to one of two adjustable DC power supplies and will be used for trace heating on hot salt lines. The last four SSRS are for AC power at 208 V and are used for various heating tasks.

Figure 3.14: The first version of the electrical box. Four more AC SSRs were added after this picture was taken.

The next important ability of the electrical box is the National Instruments interface. Using a compact Rio (cRIO) chassis, modules can be plugged in which support the basic needs of the experiment. For this experiment the following modules are being used: a digital on and off, thermocouple readers, analog output, and analog input. The digital on and off module serves the purpose of activating the switches on the SSRs, which powers the heaters. By using a specific duty cycle the heaters can be cycled on and off which allows for accurate temperature control by a LabVIEW program–in some cases within 0.1°C. Thermocouple readers are the core measurements

of the experiment and will indicate the temperature of salt, heaters, and other critical instruments. These measurements are used in real time to control the heaters. Analog output is used to control gas flow of the reaction as well as salt flow through the use of several mass flow controllers. Lastly, the voltage of several key instruments such as pressure transducers are read through the use of the analog input module.

Other interesting characteristics of the box include three over-temperature controls, which are shown on the left door panel of Figure 3.14. These over-temperature controls use an independent thermocouple and readout to control the SSRs of the three main heat zones. In the event of a thermocouple failure or a condition which causes a heater to stay in the on position in definitely, the over-temperature controller will break the circuit, preventing the heater from firing. On top of the over temperature safety, there exists an emergency stop button which instantly prevents all heaters from functioning. It does this by disconnecting the SSR's common, preventing the flow of electricity on the switch side of the SSR. For added safety, each heater line is fused with a 30 A fuse which will blow in the event of a ground fault.

All wire connections are fed through the electrical enclosure and positioned into a series of numbered terminal blocks. Each heating zone uses a 10 gauge wire for this purpose. From the terminal blocks, wires are connected to their corresponding heating zone or instrument. For NI interfacing, control and read lines are positioned through the use of CAT-6 cable. Each pair of wires, colored and white, is used for a different measurement which is sent outside to a terminal block.

The box is directly attached to the wall next to 208 VAC source with a lever breaker. Additional power is introduced through the use of a backup battery source which puts out 120 VAC and prevents the NI from shutting down during a loss of power.

3.4.9 Gas Delivery System

Accurate and safe gas delivery is paramount in order to assure the purity of the salt is at the desired level. If the ratio of hydrogen to hydrogen fluoride is too low, excessive corrosion can occur during the purification. Three gasses are used during purification, hydrogen, hydrogen fluoride, and argon. All of them ultimately enter the purification vessel through the same tubing. To insure complete safety, all pressurized lines were helium leak tested at around 20 psig using a helium mass spectrometer. As long as levels were at background levels fittings or welds were assumed leak tight.

Argon is introduced at around 20 psig through a CGA 560 fitting using flexible PFA tubing or rigid stainless steel tubing. Due to the inert nature of the gas, no special hazards had to be taken into account. The argon has four tie in points: the argon mass flow controller, the hydrogen fluoride purge inlet, Dwyer valve pressure control, and the carboy purge inlet. All connections were made with 316 stainless steel Swagelok fittings, or in some cases brass Swagelok fittings.

Hydrogen is also introduced at around 20 psig through a CGA 350 fitting using only grounded, stainless steel tubing. No PFA was used in the introductory side of the hydrogen in order to assure that static charge would not build up. As long as the hydrogen lines were leak tight, they were considered inert and non-flammable. After the hydrogen mass flow controller, hydrogen was mixed at a Swagelok tee union with the hydrogen fluoride.

Hydrogen fluoride was introduced at varying pressures without the use of a regulator through a CGA 670 fitting with a PTFE gasket. Below 19.5°C, hydrogen fluoride is a liquid with a vapor pressure of 0.9 psig. To increase this, the liquid can be heated until the desired pressure is reached. As shown in figure 3.15, around 38°C the liquid builds up around 12 psig of pressure, which is a good amount for running with a mass flow controller.

To safely reach these temperatures the hydrogen fluoride bottle was wrapped with silicone heater tape. The tape ran at around 300 W and was able to slowly heat the hydrogen fluoride. The

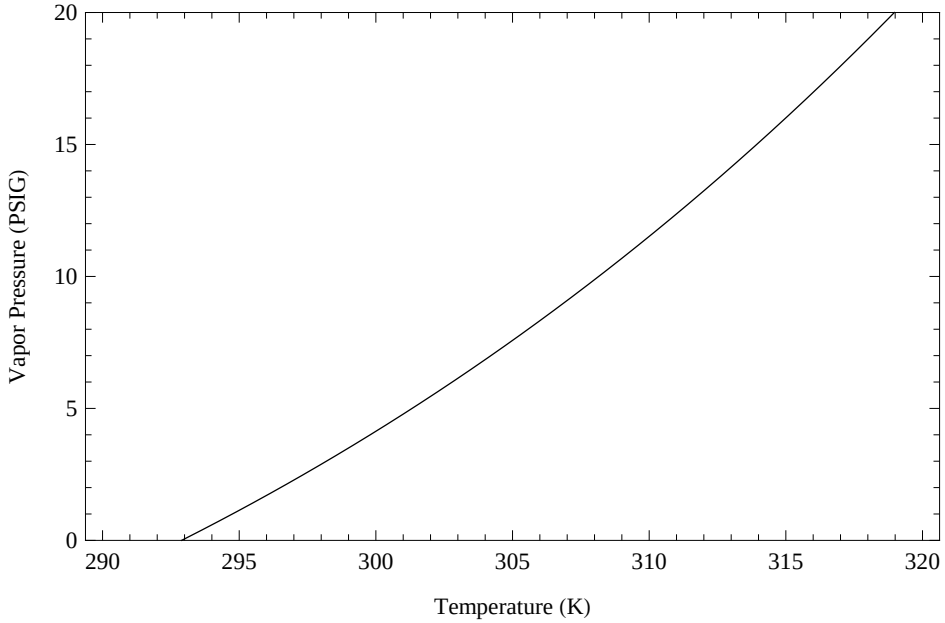

Figure 3.15: Vapor pressure of hydrogen fluoride as a function of temperature.

control this temperature, two thermocouples were taped on: one in the gas space and one on the liquid. To allow the bottle to come to equilibrium, one layer of Kaowool was wrapped around the bottle.

Once the hydrogen fluoride was warmed in the bottle it still had to be carried to the gas mixing point without condensing. If it condensed, it could potentially clog the line causing erratic flow. To keep the hydrogen fluoride in gas phase, light amounts of trace heat were run down the line. Again, one layer of Kaowool was used to prevent hot spots and allow for accurate thermocouple measurements. The whole hydrogen fluoride delivery line was controlled through one thermocouple and kept at 60°C maximum. To insure uniform temperature throughout line, all tubing was traced and insulated identically. In the case of a ground fault, all hydrogen fluoride lines were grounded and the corresponding zones were completed with low blow fuses.

Anhydrous hydrogen fluoride is compatible at delivery temperatures with many standard materials through the formation of a passivization layer. As long as no water is in the stream, nickel based alloys do not have to be used–carbon steel and stainless steel are very suitable. Due to the

excellent corrosion resistance, weldability, availability, and cost, stainless steel was ultimately selected for the delivery line. However, the passivization layer formation does produce hydrogen gas through the reaction

$$HF + Fe = FeF_2 + H_2. \tag{3.6}$$

Normally, this is not a concern as the hydrogen gas will move down the line. In the closed cylinder, this formed gas can build pressure and ultimately cause a rupture. To prevent this, the cylinder should be replaced every one to two years, with routine checkups on its pressure.

To insure no water was in the line before use, an argon purge and vent system was positioned early into the hydrogen fluoride line. Before and after running with hydrogen fluoride, the argon line is opened, pressurizing the entire hydrogen fluoride line. This line is then vented through a PFA line and through the belt driven fan. By pressurizing and venting multiple times, the line can be cleared of any water or hydrogen fluoride. Additionally, this allows for a complete purge by opening the argon line and running the hydrogen fluoride mass flow controller in the open position.

The last piece of safety equipment used to handle hydrogen fluoride is a toxic gas cabinet. The toxic gas cabinet stands around seven feet tall and contains enough room to fit three gas cylinders, or one comfortably. The gas cabinet is seal-able through a door. The outlet of the toxic gas system is attached to the exhaust system, which is in line with the belt driven fan. The fan was able to create significant flow through the cabinet. In the event of an emergency, the toxic gas cabinet could whisk away all of hydrogen fluoride without release into the room.

3.4.10 Heating and Insulation

Heating was performed entirely by electrical resistance heating. Three forms of electric heating were used: wrap around heaters, nichrome wire trace heat, and AC heating ‘tape’.

Wrap around heaters were used to heat large containers. These heaters were laser cut out of

Figure 3.16: The hydrogen fluoride cylinder in the toxic gas cabinet showing the heated, vent, and purge lines. All hydrogen fluoride containing lines were oriented atleast partially vertically so that liquid hydrogen fluoride could drain.

0.020” Inconel 625 alloy to create a long strip of metal with non-negligible resistance. Heaters used for the purification vessel are shown in Figure 3.17. Inconel 625 alloy was chosen for its excellent high temperature oxidation resistance and strength. Depending on the size of the container, multiple zones might be used in order to prevent melting salt from bursting the vessel–to do this salt is melted from the gas space down.

The prevent the heaters from ground faulting, a layer of high temperature, electrically insulating, flexible mica sheet from Cogebi was used on each side of the heater. The mica and heater sandwich was held in place using stainless steel hose clamps. To provide power, a 100VDC-150A power supply was attached to each zone at approximately 55VDC. This voltage was chosen as it was the lowest voltage possible which could achieve the required temperatures. Higher voltages could be used but a shorter heater life would be expected. The final product is shown in Figure

Figure 3.17: Two zone serpentine heaters with resistances around 3.2 Ω and 2.0 Ω producing a total 3000 W.

3.18.

Direct current trace heat zones were built by wrapping two layers of glass insulated Scotch 69 tape over the surface to be heated. This served as a high temperature, form-fitting insulator for small parts or tubes. To apply heating suitable gauge nichrome wire was cut to a resistance of 4.3 Ω which would result in a current of around 7 A at 30 V–a suitable current for long heater life. Styles of wrapping depended on a the shape and size of the object. For long tubes, several sections of straight nichrome strands were used in parallel–short tubes required spiral wrapping. Typical nichrome trace heating is shown in Figure 3.19. It should be noted that all nichrome trace zones with Scotch 69 tape release considerable fumes as they reach temperature. This is because the tape is only rated to 180°C. After reaching high temperature the tape feels like a fiberglass cast and is very brittle. Alterations to the trace heat after this point requires the application of new tape and nichrome.

The last electric resistance heating used was high temperature heating tape. Heating tape re-

Figure 3.18: The purification vessel and the receiving vessel with mica and heaters attached. Thermocouples have been welded on at this point.

quires 120-240 VAC for operation and is available in pre-manufactured lengths between two and sixteen feet. Two zones were used on the small purification vessel as well as the MSRE salt canister. Once again, these heating zones require a delicate touch after operating at high temperatures.

To thermally insulate all of the electrical heaters several strategies were used. Trace heated tubes and freestanding vessels used a mixture of Kaowool and Pyrogel XT. Kaowool is a high temperature, alumina ceramic blanket with a texture similar to wool. It is flexible, formable, cuttable, and wraps easily. Pyrogel XT is a high temperature, silica aerogel, reinforced with glass fibers–it is akin to a dusty mat. Kaowool is rated for much higher temperatures than Pyrogel XT, but has a less desirable thermal conductivity than Pyrogel XT; Therefore, Kaowool is used in one layer on top of heating elements and Pyrogel is used over it for as many layers needed. Depending on the

Figure 3.19: Finished, uninsulated trace heat. The top left shows a welded on thermocouple.

wattage and surface area of the heated object, as little as two layers and as many as five layers of Pryogel XT have been needed.

3.5 Data Acquisition and Control

A Labview cRIO chassis with a several modules was used to record data and control the experiment. For mass flow control a 9263 module was used with four ±10 V analog output channels. Heater zone control used a 9476 module with 32 channels of digital output at 24 V. Thermocouples were measured using two sixteen channel 9213 modules. Lastly, analog voltages were measured with a 9205 module in differential mode, resulting in 16 channels. Each Labview module took input from thermocouples, pressure transducers, mass flow controllers, and gas monitors in order to provide data and control.

The cRIO chassis is able to host and run a Labview program independently from a computer. In fact, all experiments are run as start up executable on the chassis itself. Programs on the cRIO

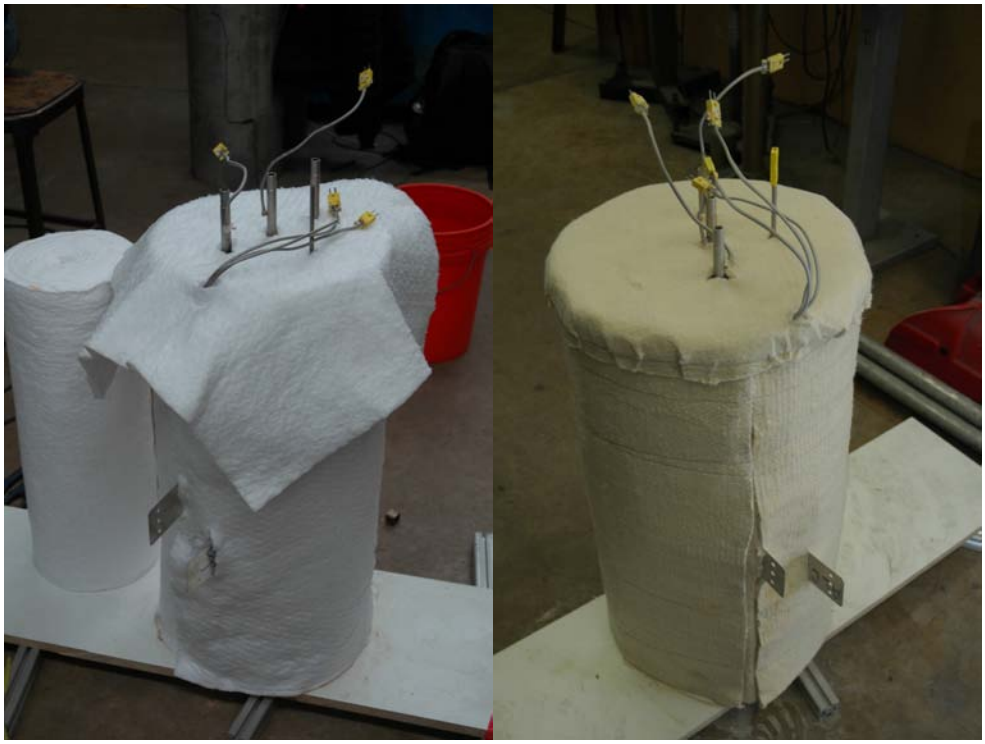

(a) The first Kaowool layer.

(b) Following layers of Pyrogel® XT; Two layers were used.

Figure 3.20: The thermal insulation for the receiving vessel.

chassis are monitored and controlled through a remote panel connection on Labview on a University of Wisconsin computer. To do this, the cRIO chassis was assigned a static IP address with its MAC address and will automatically connect to the same spot in the network after restarts.

3.5.1 Temperature

For all temperature measurements K-type thermocouples were used. These thermocouples come in wire form or prefabricated probes from Omega Engineering. Wire based thermocouple was predominately used. Depending on max temperature different wires were used. For thermocouples in close proximity to a heater, Inconel braided, ceramic, K-type thermocouple wire was used with a maximum temperature around 1200°C. Thermocouples directly in contact high temperature metal

above 100°C used K-type wire with high temperature braided glass insulation rated to 700°C. Lastly, thermocouples in low temperature conditions used polyvinyl based thermocouple wire rated to around 100°C. No thermocouples were allowed to come in direct contact with salt to prevent malfunction due to corrosion.

For the majority of applications, thermocouples were applied through TIG welding using 316 stainless steel filler or nickel filler. This prevented thermocouples from coming loose and allowed for direct heat transfer to the thermocouple. Other techniques secured thermocouples through hose clamps, in thermowells, or by Scotch 69 tape. Connections from attached thermocouples were done through the use of either polyvinyl or ceramic connectors which were lead to the cRIO chassis via polyvinyl, K-type, extension wire.

A major challenge was feeding thermocouple connections through the stainless steel support vessel while preserving seals. Temperatures would get up to around 200-300°C in certain spots in the vessel, so high temperature, braided glass, thermocouple couple wire was required. The braided glass was porous between the braids and could not be used to give a good seal. Therefore, to have a sealed vessel, the wires were striped at a certain point and fed through. The actual feed through apparatus was a 1”, 316 stainless steel, Swagelok cap with 13 pairs of holes drilled through, barely big enough to hold the thermocouple wire. To create electrical isolation between the thermocouple wire and the Swagelok, heat shrink wrap was placed on the wire where it could ground fault. A cylindrical tube was welded on top of the cap which housed the wires and a Delrin cap was machined with identical hole patterns to create a chamber which was filled with epoxy. The dried epoxy completed the seal and secured the wires. In total, two of these feed throughs were made for internal thermocouple measurements.

3.5.2 Pressure

Pressure measurements performed with both analog and digital sensors over the range of 30 inHg vacuum to 15 psig. For digital measurements a PX209-30V15G5V was used with 0-5 V output. This interfaced directly with the 9205 cRIO module. To provide backup for the electronic sensors, PGS-25L-30V/15 analog gauges from Omega Engineering were used on the gas panel and on the storage vessel. These were also useful when pressure changes had to be made without access to a computer.

3.5.3 Mass Flow

A total of three, thermal mass flow controllers were used for gas introduction into the experiment: two Aalborg GFC-17 and one Teledyne-Hastings HFC-202. The first Aalborg GFC-17 was used for argon gas at a maximum flow rate of 2.5 L·m^{-1}. It used a 0-5 VDC input voltage for control and yielded a 4-20 mA output signal to confirm the flow. All interface was through a 15 pin D-subminature located on the side of the flow controller. This D-subminature was wired using Cat-6 Ethernet cable which was in turn wired to the 9205 and 9263 cRIO module. It was constructed of brass and used Buna-N o-rings for seals. The second GFC-17 was used for nitrogen-hydrogen mixtures as well as pure hydrogen at a maximum flow rate of 2.5 L m^{-1}. Its wiring was identical as the first GFC-17. The body was constructed out of 316 stainless steel and contained Kalrez o-rings for seals. Both Aalborg flow controllers had outlets and inlets with 1/4" Swagelok fittings.

The Teledyne-Hastings HFC-202 was made for low pressure and low pressure drop service for use with hydrogen fluoride gas at a maximum flow of 0.5L m^{-1}. The flow controller was made entirely out of stainless steel, gold solder, nickel, and Kalrez, which have all been shown to be completely compatible with anhydrous hydrogen fluoride. However, great care had to be taken to prevent airborne water from entering the flow controller before and after operation which would severely corrode the stainless steel. Almost identically to the GFC-17s, the HFC-202 used a 0-5

V input for control and a 0-5 V output for measurements. All of this was provided through a Cat-6 cable wired through a 9 pin D-subminature, connected to the 9205 and 9263. To more safely handle hydrogen fluoride, the flow controller was outfitted with a orifice which could operate at 7 psig with a 0.5 psi pressure drop. This meant that the hydrogen fluoride pressure would not have to be as high as the other gases and any leaks would be less violent.

3.5.4 Power

Power was provided in five forms: 208 VAC, 120 VAC, 24 VDC, 30 VDC, and variable 0-100 VDC. 208 VAC power was pulled from the electrical box and was wired from the building's power. This was reserved for heating tape power. 120 VAC power was pulled between neutral and one of the legs of the 208 VAC power and was used for three pneumatic actuated valves. A separate, battery supplied 120 VAC power source is on constant standby in case of power outages in critical moments. This 120 VAC is used for the cRIO chassis and computer. 24 VDC was supplied from a small power supply located inside of the electrical enclosure. This was used for powering National Instruments modules and for electronic instruments such as pressure transducers. 30 VDC power came through two variable DC power supplies capable of supplying 25 A. This was only used for trace heat zones. Zones were spread between the two power supplies so that required current would never exceed 25 A. The last power supply was a variable 0-100 VDC, 150 A power supply that was used for the three serpentine heater zones. It was run so that the lowest resistance heater would only run at 30 A–this turned out to be around 54 V.

3.5.5 Salt Weight

Salt weight was measured for the large purification experiment using a 800±0.05kg scale. The entire experiment could sit on top of this scale without adverse effects to the scale. For the small purification vessel, a scale with 34 kg max and 0.1 g accuracy was used in the same configuration.

3.5.6 Effluent Stream Composition

Effluent stream composition was measured using a Pfeiffer GSD 320 corrosion proof mass spectrometer with a 0-300 AMU range. The mass spectrometer is capable of real time scanning measurements of different ion currents at different masses. These currents can be converted into gas concentrations provided the machine is calibrated to the gasses expected. Operation requires a roughing pump to reduce the pressure in the ion chamber so that a built-in turbopump can further reduce the pressure. Once pressure is achieved an inert gas purge must be delivered to the GSD 320 at a pressure between 4-7 bar. The inlet will not open and measure without the inert gas, regardless of the gas being measured. This is to protect the GSD 320 components from corrosion. Lastly, the exhaust port must be connected when in corrosive service, otherwise gases will escape into the room.

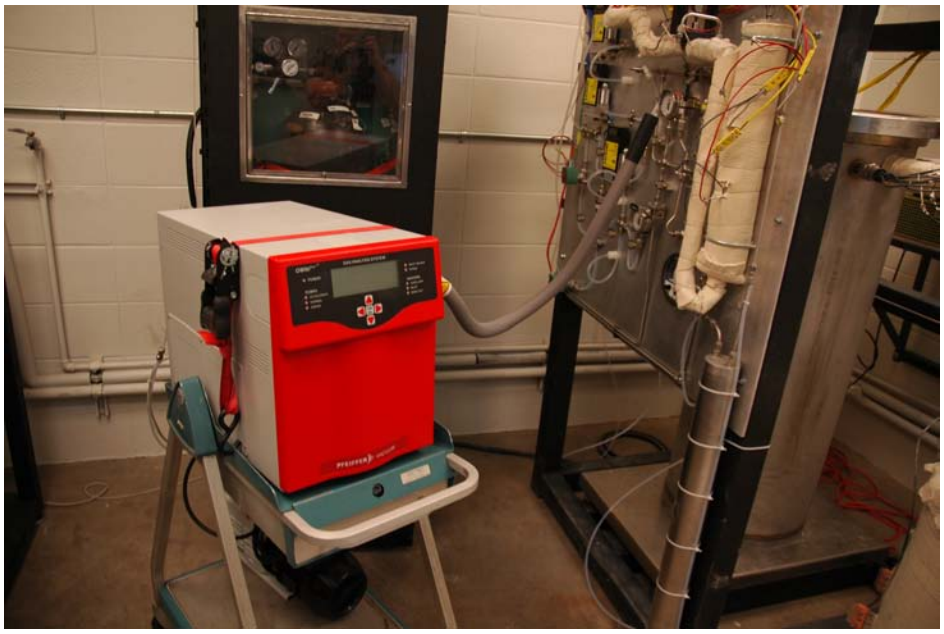

Figure 3.21: The GSD 320 tied into the effluent stream for the large batch purification.

Once the GSD is pumped down, the 1/16” capillary inlet can be attached to a measurement line via a Swagelok. The inlet can be opened through the LCD interface. A light will indicate when the inlet is open. This line can be heated to keep components volatilized. At this point the machine

is ready to measure. All measurements with the GSD 320 are done through Quadera software. Quadera can export directly into tab delimited files which are easily analyzed. Quadera interfaces with the GSD 320 through the University of Wisconsin network on a static IP tied to its MAC address.

3.5.7 Ambient Gas Composition

Keeping track of air quality in the room is key in determining if the experiment is functioning properly. Hydrogen fluoride is of main concern during operations, so two Honeywell Satellite Analog XT units with 0-10 PPM hydrogen fluoride electrochemical sensors were purchased from Honeywell. These units were chosen due to their relatively cheap replacement sensors. Powered by 24 VDC, the sensors produce a 4-20 mA signal proportional to the PPM reading which is read by the 9205 module. Additionally, each sensor has an LCD display for the gas concentration so concentrations can be read while in the room. One sensor was placed in the toxic gas cabinet while the other was positioned on the roof of the room.

3.6 Calibration and Uncertainties

Calibration important for several devices while running the purification experiments: the flow controllers and the mass spectrometer. Flow controller calibration was required in order to accurately control the gas put into the salt. If the gas rate was lower than indicated by the machine, the reaction would not extend to completion, if the rate was too high, the nickel purification vessel would corrode. All flow controllers were calibrated directly from the suppliers after purchasing. The Teledyne-Hastings flow controller was capable of 1% of full scale accuracy while the Aalborg flow controllers had 1.5% of full scale accuracy.

The mass spectrometer has proven to be difficult to calibrate which allows the conversion of the ion current of sampled gas to an actual concentration. To do this, the mass spectrometer

needs to be outfitted with a well mixed gas containing all of the components of interest during a measurement. The calibration gas has to be well known in composition. Usually, these calibration gases are obtained from Airgas, but requirements for a hydrogen fluoride, hydrogen sulfide, water, and hydrogen mix were not possible. Further will require the calibration of the mass spectrometer using the pre-existing flow controllers and their error.

3.7 Purification Operation

The purification process is a three part process. First salt most be weighed, loaded in component form into the purifier, and sealed. The second part involves heating and sparging the salt. This can predominately be performed from any computer connected to the campus network. The third and ultimate task involves moving the salt from the purification vessel and into a receiving vessel. Different parts of this process can involve personal protection equipment, which is outlined in Section 3.7.1.

Loading salt is a one person process. For prompt melt times, salts need to be layered. During the melting process, the layered interfaces will be the first to melt and cause the salt to shift, further encouraging melting. If only one interface is used, this process is severely stunted and full melting could be prolonged. Generally, salt should be layered by introducing a few kilograms of one component, followed by the other component. A list of these layers should be written out in a spreadsheet with proper load masses. To save time, the layers should be loaded to approximately these masses. A running difference can be calculated and added at the end to achieve the proper salt composition. During the loading, full PPE should be used, even for non-beryllium containing salts, as fluoride compounds are slightly toxic to humans.

Once loading is completed both the nickel flange and the stainless steel flange must be properly sealed with a grafoil O-ring. The nickel flange bolts should be coated in high temperature anti-seize and tightened with a basin wrench and a crescent wrench. After tightening, all the inside

thermocouples should be jostled at their head, while the Labview code is running. This insures that any shifting over the heating process will not affect a measurement or control process. Once this is insured, the stainless steel lid can be lifted on with the crane and attached. Due to the large bolts on the stainless steel flange, requiring roughly 500 ft lb of torque, this process is typically done by two people. Bolt tightening should be done in a star pattern in order to evenly distribute the loads. Failures to seal the inner O-ring can lead to catastrophic failure due to hydrogen fluoride corrosion. Once again, this process should be done with full PPE.

Heating and sparging the salt is usually a two person process during the active part. To begin heating, all oxygen must be purged out of the head space in the stainless steel vessel. To do this, the argon gas canister can be opened and the Dwyer switch can be used to pressure the space to around 5 psig and then used to vent. After five times, the atmosphere is sufficiently inert to prevent high temperature oxidation of any of the inner components. Argon also should be used to purge the hydrogen fluoride line. The same pressurization concept applies to this as well. Purging prevents any moisture from reacting with the the hydrogen fluoride and stainless steel delivery line. After purging all valves in the gas cabinet should be set to move hydrogen fluoride into the nickel canister. Next, all power supplies should be started and set on 30 VDC for the nichrome sections and 55 VDC for the wrap around sections. Lastly, the hydrogen and hydrogen fluoride bottle should be open. However, the hydrogen fluoride bottle should only be open one turn. Opening it more than one turn will not cause any more hydrogen fluoride to flow. Two turns is the limit for the valve. At this point the heaters in the canister can be set to 550°C. Any valve which controls outlet flow should be opened so that hot, expanded gas can escape, otherwise a dramatic pressure increase can occur.

Once the salt is melted and at around 550°C the sparge can start. The sparge length and low rate are extremely important to the salt quality. Exact numbers on rate, ratio of hydrogen fluoride to hydrogen, and time are debated. Some have favored short sparges due to production time constraints [5]. Others, such as L.M. Toth, have suggested to take the reaction far beyond its efficient

stopping point. For research purposes, the University of Wisconsin has decided to opt for a longer, less efficient sparge. Number suggested for this are shown in Table 3.3. It can be seen that the pu-

Table 3.3: Standard purification parameters calculated for a 52 kg batch.

Flibe (mols (g))	HF (mols (L))	HF Flow Rate (L m^{-1})	Hydrogen Flow (L m^{-1})	Purification Time (d)
1506 (49545)	311.7 (7637)	0.5	2.5	10.6

rification process is excessively long and would not be desirable for a full scale facility. However, the salt purified in this manner is extremely pure of oxides and water products.

At the end of purification the hydrogen fluoride tank should be allowed to cool, closed, and then the line should be purged with argon to clear out excess hydrogen fluoride. If the receiving vessel was disconnected from the purification vessel in order to avoid snow clogging in the filter, it should be connected at this time. Trace heat should be applied as well as any necessary insulation. Upon connection, the receiving vessel should be flooded with hydrogen to facilitate the removal of any oxide layers. At this point the the receiving vessel should be vented with its continuous flow of hydrogen and heated to around 550°C. Transfer lines will heat much quicker than the receiving vessel and can be started 20 minutes before the planned transfer time. When all lines are hot, the hydrogen purge can cease. The vent line should be left open. To transfer, the vent line on the purification vessel can be closed until and argon can be pushed into the purification vessel using the mass flow controller. The initial number on the scale should be noted and its reduction monitored closely. When the scale indicates that all salt on the inside has been pushed out the process is completed. A cover of argon gas should be kept flowing as all heaters are turned off and the device cools. Failure to do so can create vacuums within the apparatus, which would suck in water from the atmosphere and negate the purification process. After cooling vents can be closed, but the argon should be pressurized and maintained around 5 psig.

3.7.1 Personal Protection Equipment

Besides gloves there are two special types of personal protection equipment required for beryllium and hydrogen fluoride work: a full-face respirator and a Tyvek full body suit. Using this equipment prevents the inhalation of beryllium and hydrogen fluoride during operation and stops clothing contamination which could become airborne at a later time.

Standard Tyvek suits were purchased with elastic cuffs and ankles with a hood. Sizing was judged according employee weight and height. Boot covers were also purchased with elastic ankles to cover shoes. Tyvek is donned by putting on gloves and boot covers first followed by the suit. For added protection, the gloves can be taped to the suit using duct tape. Also, areas vulnerable to ripping, such as armpits and the crotch, can be duct taped to add extra support. Wearing Tyvek can be hot and cause unpreventable, excessive perspiration, especially with taped gloves; short breaks should be taken in order to prevent overexertion.

Figure 3.22: A Wisconsin beryllium worker wearing Tyvek suit, gloves, and a full face respirator.

Respirators come in many sizes and brands which fit faces differently. To determine the correct size and brand a fit test needs to be conducted. All Wisconsin beryllium personnel had a fit test conducted through Wisconsin Occupational Health and Safety. The fit test uses a commercially available respirator size and brand in conjunction with a saline solution vaporizer and detector. A computer program evaluates the leakage of saline solution as the user moves their body and face. At the end of the test a score is produced which leads to a pass or fail. Different respirators should be evaluated until a pass is produced. Beryllium personnel at Wisconsin ended up with 3M 6000 series full face respirators. It is extremely important that respirator wearers be clean shaven along the mold to create a good seal. Mustaches are allowed. A seal can be tested at any time by covering the center exhale port on the respirator while exhaling. The face mask should pressurize and eventually lift off–if it does not a proper seal has not been made.

Each respirator requires two cartridges to filter the air. In general cartridges are qualified by a particulate filter and a gaseous filter. For work with beryllium and hydrogen fluoride a P100/HF combo cartridge is used. It looks like a gray box with a bright yellow and magenta sticker on it. The P100 is designed to filter 99.97% of all solid airborne particulate while the HF combo cartridge is designed to neutralize and filter hydrogen fluoride in concentrations up to 30 ppm. Cartridges can be snapped into the full face respirator on each size. Cartridges have no true expiration date and should only be replaced when breathing becomes difficult due to particulate accumulation.

Removing personal protection equipment should be done methodically. First, gloves should be untaped and removed and disposed of in a contamination trash. Next, the Tyvek full body suit should be removed starting with the hood. Everything should be removed by rolling inside out so clean surfaces are the only part left exposed and dust is trapped within the rolls. Once the Tyvek suit has been rolled to the ankles, feet can be removed from the boot covers through the Tyvek, taking care to step only on a sticky mat or the clean innards of the Tyvek. After both feet are removed the Tyvek can be rolled completely, with the boot covers, and thrown away. All Tyvek is one time use only. After Tyvek removal, the room can be exited and all bare skin should be

washed. The respirator can be removed and stored after washing.

3.7.2 Safeguards

In order to prevent potentially dangerous circumstances safeguards, or engineering controls, were used. There exists two types of safeguards for the fluoride salt purification experiments: physical safeguards and software-based safeguards, of which software greatly outnumbered physical. Physical safeguards used were an emergency button stop on all heater SSRs, fuses on all heating zones, a backup power supply, an emergency pressure relief valve, an electromagnetic lock on the beryllium room door. Software safeguards used Labview code to protect personnel. Code existed which could stop heaters and gas flow in the event of an over pressurization or hydrogen fluoride release.

3.7.3 Beryllium Monitoring

Two forms of beryllium monitoring are used during flibe operations: airborne monitoring and surface monitoring. Both of these measurements are performed before, during, and after each operation and are key to preserving employee health. Ultimately, airborne concentrations are the most important measurement, but surface contamination is measured as it can contribute to airborne measurements if disturbed.

One week before working in a location where there is potential for exposure to airborne beryllium a ‘beryllium operations’ form is completed with a complete description of operations, swipe locations, and personnel working on the task. This form is sent to the Occupational Health and Safety where they prepare the correct number of pumps, pump samples, and swipe samples. All equipment is picked up the day before operations. Each pump sample and swipe sample will have a number on it such as ‘13.1295’. These numbers are then written on the beryllium operations form next to the location or person they will be used with.

Swipe tests come with number vials and a bag of Whatman filter paper. Whenever handling vials or paper, clean gloves should be worn to prevent contamination. To prepare these samples, each vial should be filled half way with deionized water and re-capped before beryllium work starts. Additionally, one piece of filter paper should be wet with deionized water and placed it its vial. This will serve as the control. Once prepared, all vials and filter paper should be kept in a sealable bag until ready to use.

To take a swipe sample, one piece of filter paper should be removed from its bag with clean gloves. The vial with the correct number for the swipe location, as indicated on the beryllium operations form, should be taken at this time. The filter paper can then be wetted with the deionized water in the vial. Any excess water should be discarded. A roughly 10cm by 10cm area should be selected and the wet filter paper should be delicately wiped in a zig-zag fashion across this area. Occasionally, parts of the filter can rub off on a rough surface–this should be avoided. After the first wipe, the filter paper's dirty side should be folded in on itself, trapping its contents and exposing clean surfaces. Using a clean side the surface can be rewiped in the same zig-zag manner and folded in on itself again. This should be done until the filter paper is too small to wipe again. The dirty sample can then be deposited in the vial and capped.

Table 3.4: Swipe sample results done after a MSRE flibe transfer operation at the University of Wisconsin.

Sample Number and Location	Be (μg/100 cm^2)	Li (μg/100 cm^2)
13.9142 - Tube Resting Place After Operation	0.26	9.4
13.9143 - Control Before Operation	<0.025	1
13.9144 - Outside of Door After operation	0.42	120
13.9145 - Top of Stainless Steel After Operation	0.057	6.6
13.9147 - Left Side Floor After Operation	0.72	30
13.9147 - Top of Support Structure After Operation	0.17	3

Whenever working with material that could produce beryllium dust, such as raw beryllium, beryllium fluoride, or containers which have housed molten or solid beryllium containing salts, air

monitoring must be conducted. Airborne samples require the use of a pump and an inline filter. The filters have two capped ends with a paper filter on the inside. The pump resides in a small box with a built in rotameter and Tygon tube.

To use the pump and filter for airborne quality measurements the pump should be secured to at risk personnel through a belt or pant line using the metallic clip on the back. Any personal protection equipment should be worn over the pump. Before zipping up personal protection equipment the pump should be switched on and the time should be recorded on the 'beryllium operations' sheet. The rotameter bead should indicate steady flow of around 1-2 $L \cdot m^{-1}$ and the pump motor should vibrate. It is a good idea to periodically check the pump for vibration. If the pump is not flowing, work should be stopped. Finally, the Tygon tube should be attached on the outside of the personal protection equipment with its alligator clip. After completing operations the pump should be switched off and the current time, as well as the minutes indicated on the LCD, should be recorded.

Table 3.5: Beryllium and lithium concentrations in air were below detectable limits during the flibe transfer, and during room operations after the flibe transfer. Dust is assumed to be pyrogel insulation.

Location and Sample Number	Time (m)	Be ($\mu g\ m^{-3}$)	Li ($\mu g\ m^{-3}$)	Unknown Dust ($\mu g\ m^{-3}$)
13.1949 - MSRE Flibe Transfer	104	<0.06	<0.06	260
13.1950 - HF Line Installation	180	<2.4	<2.4	660

All beryllium containing samples should be returned to the University of Wisconsin Occupational Health and Safety. From there, the samples will be given to the Wisconsin Occupational Health Laboratory (WOHL) where the analysis is performed. Wipe samples are digested by the in-house method EHD METALS METHOD 002 rev.3 which is based one NIOSH 7303. This method involves digestion using a mixture of HNO_3 and HCl acids made up to a 50 mL final volume. An aliquot of the sample is analyzed for metals using the EHD METALS METHOD 400.2 rev.3 which is based on EPA 200.7 and SW846 6010B using an axial/radial inductively coupled argon

plasma optical emission spectrometer (ICP-OES). Samples are not blank corrected. Air samples are collected on mixed cellulose ester filters where are then digested through the same methods as used for the swipes. Flow rate and time are used to determine an average beryllium content in air. Sampling pumps with filter paper cannot determine instantaneous beryllium content.

3.7.4 Clean Up and Disposal

Clean Up of beryllium contaminated items proved to be time consuming but not impossible. The high solubility of BeF_2 in water is key to the removal of it from surfaces. To clean a contaminated surface or object, paper towels were used with 409 cleaner on a surface multiple times, followed by paper towel and water. Each paper towel would be thrown away after each usage. These towels, along with contaminated gloves, Tyvek suits, and other irreclaimable equipment, were double bagged and given to chemical safety trash pickup for disposal. Chemical safety was informed that these bags contained beryllium and disposed of them properly from there. Solid chucks of flibe, within disposal guidelines from chemical safety, could be disposed of by sanitary sewer.

After each cleaning, a swipe test was performed in all pertinent areas. These were done to insure that the surface containment was lower than the limit. If the test came back at higher than the limit, cleaning would be done again. Regardless the measured contamination, Tyvek and respirators were used whenever entering the walk-in fume hood.

Chapter 4

Experimental Results

4.1 Test Run with KF-ZrF_4

The first run with the purification system was done with KF-ZrF_4. Although this salt is not of great interest in comparison to other proven salts, such as flibe, it is relatively non-toxic, so any mistakes or malfunctions could be dealt with little to no precautions. Therefore, it was thought that this salt would be an excellent test run of the purification apparatus. In total, over 20 kg of salt and water containing salt were loaded into the nickel vessel. It was planned that after bake off, which will be discussed in the following paragraphs, that the remaining salt would be around 20 kg.

Thus far, four runs have been performed, each with a total run time of 2-3 days. Each run delivered a new failure which was addressed accordingly. In the first run, the temperature was slowly ramped by 25°C as to remove the water without the production of hydrogen fluoride. Thermodynamics indicated that hydrogen fluoride would be equilibrate at 1 mol % with a baking temperature of 320°C, therefore it was advisable to remove the water before such temperatures were attempted. To do so, baking temperatures were increased to 100°C and held until the effluent stream temperature decreased. The increased heat capacity of water would heat uninsulated lines to around 43°C while water was being removed. As the water content in the gas would decrease, the temperature of these lines would decrease to a few degrees above room temperature. Once the effluent stream temperature decreased, the baking temperature was increased by 25°C and the process was repeated. This yielded a total of 3.5 L of water which was captured inside of a high density polyethylene holding tank.

Run one was terminated when it was found that the temperatures in the head space could approach the max operating temperatures of the thermocouple wire which was used to control the

Table 4.1: An overview of the KF-ZrF_4 (58-42 mol%) runs.

Run	Start Date	Time Operated (d)	Max Temperature (°C)	Notes
1	3/1/2013	3	250	Around 3.5 L of water exhaust. Head temperature unknown.
2	3/25/2013	2	286	First heater failure due to broken wire.
3	3/28/2013	2	373	Second heater failure due to oxide layer. Valve failure directly after run.
4	4/19/2013	3	550	Run ended upon filter clog.

heaters. If the thermocouple wire failed, the automatic control could potentially over power the heaters, causing them to melt. In the down time, two new thermocouple feed throughs were made which had a temperature rating of 700°C.

Run two was slightly more successful than run one. Achieving a top temperature of 286°C over the course of two days, the water content removed was drastically less. This run was terminated after the first heater failure which is discussed in section 4.1.3.

Run three was the first time salt temperature approached the theoretical melting point of KF-ZrF_4. This run terminated upon heater failure as well.

While trying to restart after run three it was found that the high temperature Monel valve was failing to actuate. To circumvent this, a Monel tube bypass was made and a three way valve was used down the effluent line to close or open the stream. The valve failure found before run four is discussed in section 4.1.2.

Run four was the most successful run to date. The heaters functioned at 550°C for nearly a day with no apparent problems. Pressure began to build in the nickel vessel after around a day of running at 550°C, presumably due to snow accumulation; this change lead to the initiation of the transfer and the subsequent clog of the filter shown in section 4.1.5.

4.1.1 Sparge Gases and Salt Composition

The sparge gas used for the KF-ZrF_4 (58-42 mol%) run was chosen as a mix of ultra high purity argon and ultra high purity 95% nitrogen - 5% hydrogen mix. These gases were chosen for their low water content, inert qualities, and in the case of hydrogen, for its reduction potential. Although none of these gases were able to fluorinate the salt, the hydrogen has been shown to inefficiently reduce unwanted metal fluorides and cause them to precipitate out. Additionally, hydrogen can help prevent corrosion in the event hydrogen fluoride is formed.

Salt used for the run was potassium fluoride from Noah Technologies and zirconium tetrafluoride from WHERE. This salt was purchased from there due to the its price which was WHAT PRICE as compared to 250$ a kg from Noah Technologies. The ZrF_4 was found to have unacceptable quantities of in its as purchased form. It was previously measured that the salt was 27.5% water. In order to counteract this water weight, extra ZrF_4 was loaded into the vessel. In total, 23.85kg of salt was loaded for a 20kg batch; 17.23kg of ZrF_4 and 6.61 kg of KF.

4.1.2 Valve Failure

The effluent stream relied extensively on a pneumatic actuated, high temperature, Monel valve. This valve was able to directly control the pressure of the nickel vessel by turning on and off. Before the third start up the KF-ZrF_4 (58-42 mol%) run, the valve was found to be stuck in the closed state. Upon examination of the valve housing, a relief hole was found with dark green corrosion products emanating from it. The valve was disassembled to check for any corrosion.

The all wetted components of the valve were found to show signs of corrosion–the worst being the bellows apparatus. The bellows, shown in figure 4.1 had corroded so severely that the bellows had split. Several pieces of it fell off upon opening. Certain areas of the stem had turned green. This green particulate moved into the valve's body and into the tube after it. Replacement parts have been purchased and will be installed.

Figure 4.1: Failure of the bellows and the valve stem.

Although the cause of the corrosion is not known, it is thought that the combination of the water, ZrF_4 salt, and hydrogen fluoride contributed to the valves failure. In future runs none of the salt components will have as much water in them, hopefully lessening the corrosion.

4.1.3 Heater Leads Oxidation

Each of the nickel vessel's two heating zones had two rabbit ear connection terminals. These rabbit ears were connected to the power supplies through the use of three bolts and two copper blocks on each side, shown in Figure 4.2a. Due to space restrictions these leads had to be cleverly placed. Initially, the two of the lead assemblies were folded and buried in pourable insulation under the transfer line while the other two were allowed to stand freely in air. Heater zone two failed at a heater temperature around 286°C and a current of around 24 A. The cause of the failure was excessive oxidation of the 10 gauge copper wire buried under the insulation at its terminus on the copper blocks. The oxidation cause the wire to weaken and break. Additionally, all off the buried copper had a thick, flaky, black layer coating it, shown in Figure 4.2a.

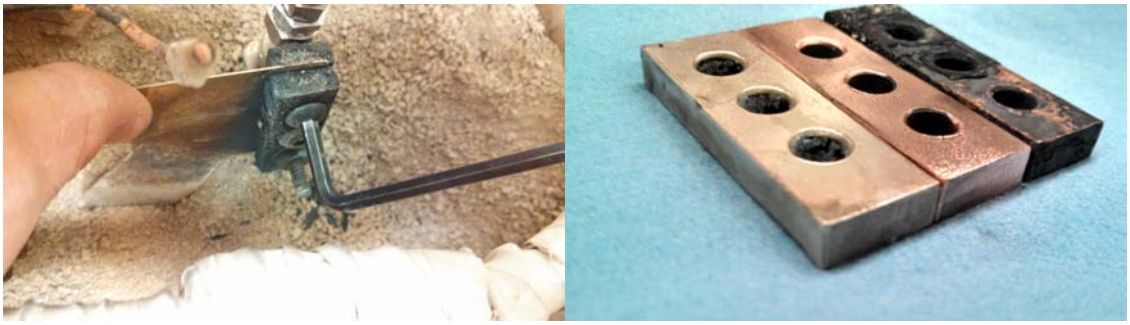

(a) The rabbit ear-copper block heater connectors. The broken power cable is shown in the top left.

(b) Three states of the copper blocks. From left to right: Silver coated, polished copper, heavily oxided copper.

Figure 4.2: Copper block power heater lead assembly.

The copper blocks from heater zone two were removed and re-polished while the broken wire was replaced with two 10 gauge wires which would reduce the temperature of the wire by reducing the current it carried. To prevent the potential failures of heating zone one and two, both assemblies were removed from the pourable insulation. This was done by bending the rabbit ear for zone two into the upright position and placing mica board over the rabbit ear for zone one. This mica served as a dam for any nearby pourable insulation but did not provide direct access to cooling air. The experiment was then restarted and operated for two days at a maximum 373°C when heater zone one failed.

Heater zone one carried a thick oxide layer from the initial run which was not removed while fixing zone two's rabbit ear. During the second run, the pre-existing oxide layer on the blocks grew larger and eventually insulated electrical contact from being made between the copper and the inconel rabbit ears. Repairs were made in excess this time. All copper blocks were removed, polished, cleaned, and then plated with silver through chemical means. It is hoped that the silver will prevent excessive oxidation. Next, all rabbit ears were bent to the upright position, isolated electrically, and exposed thermally through the use of mica dams. The dams were placed so that the rabbit ears could form a direct convection cell with the overhead gas, while containing enough insulation to keep the transfer line hot under trace heat. Lastly, upon the third run, the overhead gas

was pressurized with argon and vented multiple times until the gas composition approached 90% argon. By cooling the heater leads and preventing thick oxides from forming by silver coating and inert atmospheres, the heaters are hoped to work consistently for a minimum of a week.

4.1.4 Effluent Stream Contents

Upon heating the salt past its melting point white powder was observed all the way down to the end of the effluent stream. This powder was easily seen through the translucent PFA lines. The powder was streamlined with the direction of flow and uniform. It was found that more pressure was

Figure 4.3: White snow in the center of PFA lines.

needed to push gas through the effluent line the longer the salt was melted and purged. Depending the the flow rate the pressure in the nickel vessel would be from 0.8 to 1.3 psig. This pressure was created by the constricting inner diameter of the 1/4" tubing as well as the hydrostatic pressure from the water bath scrubbers at the end of the line. After pushing purge gas and salt vapor through the effluent line for roughly forty hours, the pressure in the nickel vessel was found to increase roughly 0.5 PSI. In order to prevent an eventual clog of the effluent line and subsequent pressurization of

the nickel vessel, purging was stopped at this point and transferring was initiated.

4.1.5 Performance of Filtration Unit

The filtration unit used for the KF-ZrF_4 (58-42 mol%) run was constructed from 316 stainless steel housing with a 25 micron, 316 stainless, SinterPore filter from Porous Metal Filters sandwiched inside of it. Its purpose was to filter out any metal or carbon particulate that might be suspended in the salt. This filter design proved leak proof and secure at high temperatures, but did not withstand the environment created by the KF-ZrF_4 salt and ended up clogging before the transferring of the salt even began.

While heating the purification vessel and the receiving vessel up to the operating temperature of 550°C the pressure differential varied a maximum of ±1.5 PSI. As the receiving vessel heated, the gas expanded, increasing the pressure. This excess pressure was vented in order to prevent the receiving vessel from deforming under the stress. It is believed that this pressurization and venting

(a) A comparision of the filter unit before(left) and after(right) snow build-up.

(b) The lid the filter unit showing a large buildup of ZrF_4 snow.

Figure 4.4: Two components of the clogged filter unit.

action helped move ZrF_4, hydrogen fluoride, and potentially KF vapor through the transfer line to the filter unit. Once the mixture was in the filter it was readily able to clog the 25 micron pores through a mixture of deposition and corrosion. The salt deposits are thought to consist of mostly

ZrF_4 deposits moved in vapor phase, commonly referred to as 'snow'. These deposits are shown in figure 4.4a covering roughly half of the filter cup. Figure 4.4a also shows a reddish area which is thought to be corrosion related to hydrogen fluoride vapor. A large portion of this snow was able to move through the filter, coating the end of the filtration unit with roughly a 1/16" layer of salt. This salt was found to continue down the line towards the receiving vessel.

Due to the fact that the salt deposition was largely ZrF_4, the sublimation point of this snow was around 600°C, or roughly 210°C higher than the melting point of KF-ZrF_4. The trace heat on the all of the transfer line had operation temperature of 550 °C, and therefore could not remove the snow through sublimation. Any snow that moves into unwanted locations will have to be dissolved or scraped away.

4.1.6 Cleaning

Cleaning equipment in between runs was extremely important in order to produce high quality salt. If the vessel was not cleaned of untransfered salt, snow, and structural metal impurities would find their way into the next batch of salt. A wide variety of cleaning methods were tried on the KF-ZrF_4 (58-42 mol%) salt and a few with success.

Cleaning of KF-ZrF_4 (58-42 mol%) salt was first tried on the clogged filter. Initially it was hoped that the ZrF_4 salt would dissolve into water. Even though the solubility is very low, 1.32 g/100 mL at room temperature, it was hypothesized that water could be continually flushed to remove the products while providing clean water for dissolution. This did not turn out to be the case; solid white chunks were still left attached to the filter after flushing and ultrasonicating for a day. Next, aluminum nitrate solution was introduced to the clogged filter. This salt produces a pH of around two when concentrated has been used successfully at the University of Wisconsin to dissolve LiF-NaF-KF salt (46.5-11.5-42 mol%). After a day of ultrasonication, the aluminum nitrate failed to initiate strong dissolution, although some salt did become soft and was able to be

scraped away.

After the failures of the water and aluminum nitrate, mineral acid based dissolution was considered. These solutions are harder to handle and have the potential to produce hydrogen fluoride upon their success. First, a solution of around 10% hydrochloric acid was used to attempt to clean the salt off of the stainless steel filter. This method was attempted for roughly fourteen hours with mild success. Overall, the filter had a good shine, and was able to pass water in certain locations unlike before, but salt still clogged the lower half. The next mineral acid tried was a solution of around 7% sulfuric acid. The sulfuric acid immediately made bubbles indicating a reaction. Ultimately, this did not prove successful at removing the salt from the pores. Ammonia solution was also tried, without success. The filter was discarded as uncleanable.

The lack of success cleaning the filter prompted the problem of cleaning out the KF-ZrF_4 salt from the large purification vessel. The dip tube extended around a quarter inch from the bottom, so after a transfer this volume of salt would be left for cleaning. The nickel purification vessel was welded shut except for a few inlets and outlets for salt and gas; abrasively cleaning the salt from the nickel was out of the question without removing it from the stainless steel vessel, removing its heaters, and cutting it open. To gain experience with this a puck of KF-ZrF_4 was melted into a small nickel vessel, two inches in diameter. Running water was directly applied to the solidified salt for roughly a month and a half. It was hypothesized that the running water would constantly refresh the low solubility limit and allow the salt to dissolve. The results from this test are shown in figure 4.5. In the end the salt showed no noticeable signs of dissolving. The salt was poked with a rod and was found to chip away very easily, which is seen in the top half of figure 4.5. If the salt in the nickel vessel could be exposed to water and then chipped out it would be easy to remove. This was not possible, as mentioned before, due to the welded design. A non-aqueous method would have to be used to removed the salt from the nickel vessel without disassembling the purification experiment. A sacrificial salt melt was suggested by L.M. Toth and read about in a paper by Nishimura [61]. A melt of KCl-LiCl is planned which will dilute the ZrF_4 and KF to the

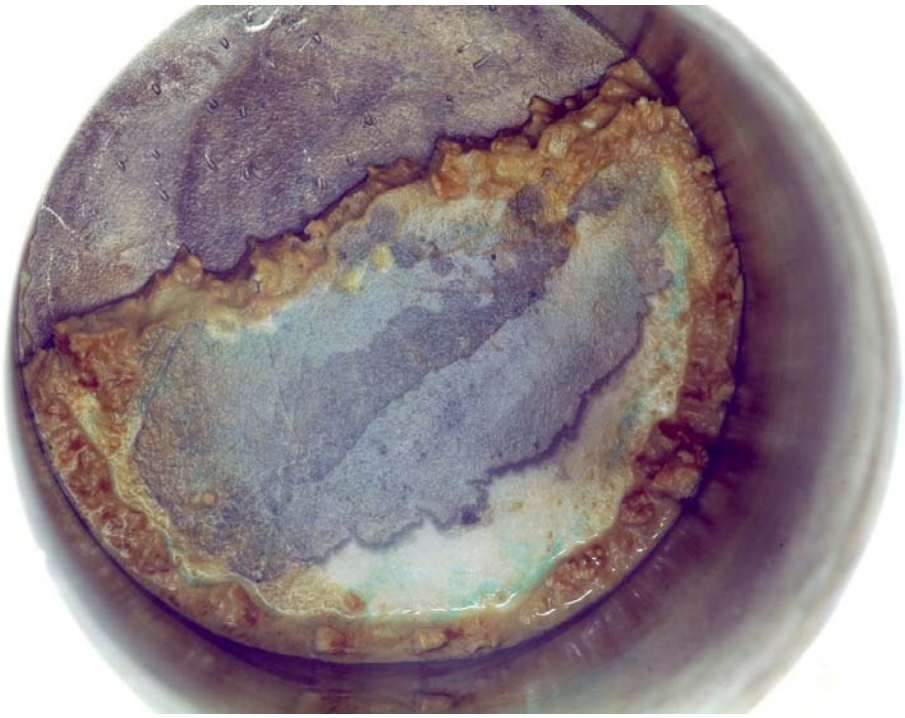

Figure 4.5: The inside of the small nickel vessel looking down at the cracked layer of salt after a month long water bath.

point where it can be pushed out with the melt.

4.2 Purification of MSRE ^{7}LiF-BeF$_2$ (66-34 mol%)

It was decided at the fluoride high temperature salt-cooled reactor workshops that corrosion testing of various materials in flibe would be done in the MIT research reactor in order to evaluate the performance in real nuclear reactor conditions. Natural lithium contains 7.5 atomic percent lithium six which can produce tritium through the reaction

$$^{6}\mathrm{Li} + \mathrm{n} \rightarrow ^{3}\mathrm{H} + ^{4}\mathrm{He}. \tag{4.1}$$

Natural beryllium can produce tritium as well, but at a much lower rate. Tritium is very undesirable for nuclear operations as it hard to confine. To prevent excess tritium production,^{7}Li flibe was

required. The United States does not produce considerable quantities of this any more nor is it available in molecular form, such as ^{7}LiF . The only available ^{7}LiF was in the ^{7}LiF-BeF_2 (66-34 mol%) stored salt from the secondary loop of the MSRE.

Figure 4.6: Molten salt reactor flibe being loaded for shipping with the molten salt reactor building in the background.

Around 350 kg of the secondary loop salt was stored after the decommission of the molten salt reactor. This loop did not contain dissolved fission products or uranium, but was slightly radioactive due to tritium migration through the heat exchanger. Since the reactor operated around forty years ago, this tritium has had around three and a half halflifes of decay, making it safer to handle. Tritium content in the salt is covered in detail in Section 4.2.2. In a final step of commissioning it was agreed that the University of Wisconsin would receive 57.4 kg of the molten salt reactor flibe to re-purify and send to MIT for reactor use only. The salt would be re-purified in order to reduce its fluorine potential after being potentially contaminated by sitting in the basement of the molten salt reactor building for forty years. The main concern was that the salt's fluorine potential had be-

come less negative over the course of its storage and that this would impact corrosion. Impurities found in raw components, such as carbon and sulfur, were assumed to have been removed during the salt's original cleaning.

4.2.1 MSRE Flibe Canister and Initial Sampling

Salt arrived in a 316 stainless steel cylindrical canister with a domed top and bottom. Three female 1/2" NPT half couplings were welded in line on the top dome. Each NPT half coupling hosted a capped 1/2" Swagelok to 1/2" male NPT fitting. A coupling guard was welded coincident with the bottom of the dome to protect the fittings during transport. For stability, a skirt was included on the bottom to give a flat resting space. The total amount of salt was billed at 57.4 kg. All beryllium swipes were below ORNL release criteria.

Upon arrival, a sample was taken through the use of a core drill while in full PPE for the evaluation of tritium and metals content. The actual drilling process was done using a 15" long 1/4" OD tube with a serrated edge which extended to the surface of the solidified salt inside of the can. Great care was taken in prevented the excessive release of dust during drilling. It took multiple attempts to remove enough material for the tests; the flibe was very hard.

4.2.2 Tritium Content

Tritium activity of the ^{7}Li was measured at ORNL on September 3rd, 1999 and analyzed on September 8th, 1999 in two important areas: the salt itself and the sparged gas cold trap during the melting processing. It was found that the 350 kg of secondary loop salt had 0.27 mCi of radioactivity, or roughly 0.771 nCi g^{-1} and that the cold trap contained 0.02 mCi after 3.3 hours of flow at 0.25 L min^{-1} resulting in 20 nCi L^{-1} [62]. These numbers are 13.61 years old, or roughly one year longer

than the half life of tritium, 12.32 years, and had to be re-evaluated. Through the decay equation

$$A(t) = A_0 e^{-\lambda t}, \tag{4.2}$$

where A is the activity, $\lambda = \ln(2)/t_{1/2}$, and t is the decay time, it was determined that the total activity as of April 2013 was 0.13 mCi. The University of Wisconsin received 57.4 kg of salt, or roughly 16% of the tritium analyzed batch, therefore the current activity of the University of Wisconsin salt was theoretically found to be approximately 0.021 mCi at 0.359 nCi g^{-1}. Analysis performed by the University of Wisconsin reactor lab concluded that the total inventory was 0.0157 mCi or 0.3 nCi g^{-1}, a lower than expected value.

The radioactive nature of the salt required special inquiry to gauge the spread of tritium and insure disposal of radioactivity during any operation was legal. To evaluate this, all worst case scenarios were envisioned. It was found that volumetric radioactivity of the salt was low enough that in the case of a spill the salt could be disposed of down the drain in accordance to chemical safety advice while meeting requirements of 10 CFR Part 20. If the tritium was able to become gaseous it could be released in two ways: in a gas form during sparging, or with the salt as a spill. If all the tritium in the 57.4 kg of flibe was released in gas form and expelled out of the room by the overhead fan through the exhaust system, the tritium concentration would be 7×10^{-10} mCi mL^{-1} over a full purification cycle, which is within release guidelines in accordance to 10 CFR Part 20. If all of the sparged off tritium dissolved in the 26 L carboy water bath the concentration of tritium would be 8.08×10^{-7} mCi mL^{-1} which could be disposed of by sanitary sewer. Through this worst case scenario evaluation it was found that regardless of the route, tritium would be disposed of within guidelines due to its low activity in the salt.

4.2.3 Transfer of MSRE Salts

The stainless steel MSRE canister was retrofitted with two, 16', 240 VAC tape heat zones. These were wrapped sparsely on the top and denser on the bottom. Each heat zone thermocouple was attached with a hose clamp in order to avoid welding on a surface which could host beryllium particles. Insulation was done through the standard kaowool wrap followed by three Pyrogel XT wraps. For pressurization, the first orifice in the MSRE canister was attached to argon gas through a regulator. The second coupling Swagelok was left for the transfer tube. The last Swagelok outlet was used for pressurization equalization and isolation. This was accomplished through a manual ball valve attached through half-inch line connected to each vessel through a tee fitting. The last port on the tee was connected to the pre-existing carboy exhaust system. This is shown in figure 4.7. The MSRE can sat upon three layers of firebrick with a layer of Pyrogel XT underneath it.

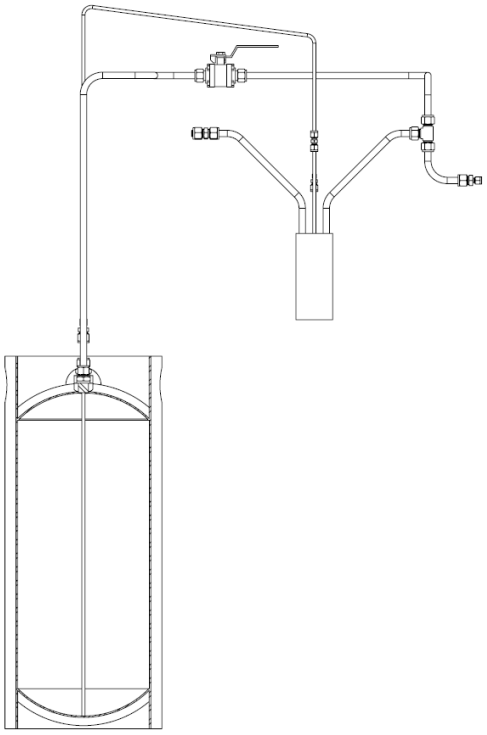

Figure 4.7: The transfer setup for the MSRE flibe.

This was done to minimize the distance required to connect the small nickel purification vessel.

Lastly, to measure the amount of salt moved, the small nickel purification vessel was placed upon a very accurate scale.

The transfer began by heating the salt. A day into the heating the temperature increase slowed down greatly. Two extra layers of Pyrogel XT were added to fix this. In all, it took two days melt and reach the transfer temperature of 550°C. Salt is always transferred at 100°C above its melting point in order to minimize the risk of a freeze due to a cold spot. Once the salt reached temperature, full PPE was donned, the middle Swagelok port was opened, and the transfer tube was inserted to nearly the bottom. The 316 stainless steel, 1/4" outer diameter transfer tube was around 85" tall and extended to roof the room before snaking in at an angle to the available port on the half inch tube. Quarter-inch line was chosen to restrict the flow of salt which would increase the accuracy of salt mass transferred. It was trace heated with three lengths of nichrome wire and insulated with one wrap of kaowool and two wraps of Pyrogel XT. To secure the transfer tube, a Swagelok fitting was used on the MSRE canister side and the small nickel purification vessel side. These Swageloks were not trace heated.

Once the transfer tube was attached and tightened in, the half-inch ball valve was set to closed, the argon inlet on the MSRE canister was switched to the carboy system exhaust, and the small nickel vessel was pressurized to a few PSI with argon. This forced argon to bubble through the transfer dip tube in the MSRE canister. By bubbling, the salt would mix and the temperature would become more uniform. Additionally, the line can be felt vibrating as the bubbles are produced, proving that the salt is molten and the line isn't clogged.

After bubbles were confirmed, the transfer line and purification vessel began heating to 550°C. At the same time, the argon pressure was reapplied to the MSRE canister, the tee outlet on the small purification vessel was reattached to the carboy exhaust system, and the half-inch ball valve was opened. Simultaneously, both unheated Swagelok fittings which connected the transfer tube were heated with blowtorches on and off for fifteen minutes. While not under fire they were and kept wrapped in kaowool.

The actual transfer was the shortest part of the process. The small purification vessel's scale was tared to account for thermal expansion, the half-inch ball valve was shut, and the MSRE canister was pressurized to around 4 pisg. Almost immediately the scale started to reflect the moving salt. After one minute, 550±25 g of salt was transferred in the nickel vessel and the half-inch ball valve was opened, equalizing the pressure between the two vessels, causing residual salt to clear the line.

After transfer the salt was completed the tube was removed. One Swagelok had leaked salt, while another was oxidized closed. The leaked Swagelok was carefully removed and covered while the oxidized Swagelok required forceful removal. The entire transfer tube was laid on the ground to cool and double bagged for removal at a later date. The MSRE canister was then closed with a constant purge of fresh argon as it cooled to counteract pressure changes.

4.2.4 Purification Process

Before the transfer began 0.1 g of B-26-D grade, 99.5% by metals basis, beryllium from Materion was dropped into the small nickel purification vessel to serve as a redox agent during melting and purification. Usually, the redox is used as a last step in the storage, but there was no capability to do this in the single purification vessel.

The gas sparge came after the transfer. The salt was remelted from top to bottom and heated up to 550°C. Once the salt was significantly above the melting point the sparge preparation began. All hydrogen fluoride lines were purged with argon multiple times. Then, the hydrogen fluoride gas bottle was opened one full turn, allowing the gas to diffuse into the lines. After opening, the bottle and trace lines were heated slowly to around 38°C to pressurize the hydrogen fluoride. Once at temperature, an actuated valve was opened and the hydrogen fluoride was fed into the vessel. Hydrogen flow was placed at 1.13 L m^{-1} to prevent corrosion of the nickel vessel while purifying salt.

Hydrogen fluoride flow lasted for around thirty minutes before behaving erratically, bouncing

from no flow to max flow several times per minute before ceasing. To troubleshoot the lack of flow several things were tried. First, the temperature of the hydrogen fluoride bottle was turned up to around 43°C. Additionally, all hydrogen fluoride trace heat lines were turned up to around 60°C. Pressures increased, but flow did not resume. Next, the flow controller was heated with a hot air gun to clear any condensed hydrogen fluoride in the line. This caused an artificial increase in flow–the mass flow controller uses thermocouples to measure flow–after heating the flow stayed at zero. Since condensation wasn't an issue, it was assumed that in this thirty minutes the mass flow controller had corroded. The hydrogen was left on all night and inspected the following morning.

The next morning, the hydrogen was found to be flowing according the mass flow controller, but the first carboy in the effluent stream neutralizer had ballooned up and appeared to have pressurized. Pressure was released and the dip tubes which neutralized the hydrogen fluoride were examined. It was found that the first dip tube had clogged. Upon clearing the clog the hydrogen fluoride would flow again. It is thought that this was from the production and crystallization of sodium fluoride in side of the tube. In further runs larger diameter Teflon tube will be used.

4.2.5 Purified Salt Contents and Appearance

Samples produced for MIT testing were made by pouring molten flibe into a nickel tray inside of a glovebox at roughly 600°C. The salt did not wet to the nickel as it solidified. The final cooled sheet of purified salt was a translucent to white color as shown in Figure 4.8. The sheet was smashed with a pestle into manageable pieces and stored for further use in an container sealed in a inert atmosphere. In comparison to flibe produced by other methods, the cleaned MSRE was much whiter in color. Salt produced without purification has ranged in color from gray to yellow-white and is shown in Figure 4.9

Visual results are important for qualitatively assessing the salt. A cleaner salt will be whiter. Once a salt is colorless, there can be variation in fluorine potential and metals concentrations which

Figure 4.8: Close up of flibe in a 1cm diameter vial.

Figure 4.9: A comparison of University of Wisconsin flibe and MSRE flibe. From left to right: re-purified MSRE flibe, salt melted in open atmosphere from raw components, salt melted in a glove box from raw components.

can go unnoticed by the eye. These must be measured by instruments.

4.3 ICP-OES and ICP-MS Purity Measurements

Two modern techniques have been commercialized since the end of the molten salt reactor program, Inductively Coupled Plasma-Optical Emission Spectroscopy (ICP-OES) and Inductively Coupled Plasma-Mass Spectrometry (ICP-MS). Both techniques rely on the ionic nature of plasmas to characterize and sort samples. In the case of ICP-OES, samples are atomized and then ionized in an argon plasma. Each element gives off a characteristic wavelength of light. The intensity of this light can be converted into a concentration on up to sixty elements per run. ICP-MS works off of the same principle except the plasma is sorted through and electric field.

In order for ICP-OES and ICP-MS to be viable options, the sample must be completely dissolved within a solution for analysis. The concentration of the solution must be known so that the technician performing analysis can dilute the sample to the proper concentration. Dissolving fluoride salts presents a unique challenge in that main components and corrosion products are never all soluble. Of the most severe challenges for analysis are salts containing LiF and ZrF_4. Both of these fluorides are highly insoluble, as shown in Table 4.2. To dissolve these salts, a mixture of

Table 4.2: Solubility limits of key cations. Salts are listed by their anion. Temperatures in °C are in parenthesis. Special conditions are noted when relevant.

Species	Solubility in Water (g/L)			
	Fluoride	Nitrate	Chloride	Sulfate
Li^+	1.34 (25)	900 (28)	550 (20)	349 (25)
Be^{2+}	very soluble	1660	151 (20)	305 (30)
Zr^{4+}	13.2	-	hydrolysis	525 (tetrahydrate)
K^+	1020 (25)	3160 (20)	3440 (20)	1110 (20)
Cr^{2+}	767	810 (20)	very soluble	anhydrous insoluble
Fe^{2+}	1650	1500	685 (20)	256 (anhydrous)
Ni^{2+}	40	942 (20)	642 (20)	650

hydrochloric acid, nitric acid, and potentially sulfuric acid have to be used in a bomb calorimeter at elevated temperatures. Care must be taken when using concentrated sulfuric acid, as its affinity for water is so great that it can absorb it from other acids and liberate the acidic component, such as hydrogen chloride or nitric acid gas. With some salts, such as flinak, accurate results have yet to be achieved through dissolution and ICP-OES. It seems the strong alkali fluoride bonds prevent the anions from being converted, even in the presence of acids. On the other hand flibe, lends itself towards analysis at the right analysis concentrations. Success has been achieved with raw flibe at the Wisconsin Occupational Health Laboratory, where flibe was digested with aqua regia, a mixture of nitric and hydrochloric acid. As compared to ideal LiF-BeF_2 (66-34 mol%), Wisconsin salt

Table 4.3: Analysis of two batches of flibe produced at the University of Wisconsin, one melted in air, one melted in a glove box. MSRE Flibe was repurified at the University of Wisconsin, but prepared during the MSRE. The MSRE Flibe Thoma data is from batch 161 of the flush and coolant salts. Lithium and beryllium values are shown as determined at ORNL [8].

	Li		Be	
	Measured (%)	Error	Measured (%)	Error
Open Air Melt Flibe	14	0.2	8.9	2.3
Glovebox Melt Flibe	14	0.2	9.3	2.0
MSRE Flibe	14%	0.2	9.8	7.5
MSRE Flibe Thoma	13.2	5.9	9.8	7.5

is closer in composition than the flush and coolant values reported by Thoma [8]. However, these measurements do nothing to indicate the purity and quality of the salt–they only show the salts composition by metals basis. These numbers can be used to determine how close the completely purified salt would be to the ideal composition.

4.4 Neutron Activation Analysis

Some elements in the salt cannot be measured as accurately as needed when the main constituents exist in such high concentrations. For example, Cr, Fe, and Ni all lie in the ppm range after purifi-

cation and therefore will have relatively small intensities in ICP-OES as compared to beryllium or lithium, at all dilution ranges. Therefore, to measure these values, a new technique has to be used. Neutron activation analysis (NAA), lends itself to these measurements easily.

Neutron activation analysis is a ultra precise measurement technique which uses thermal neutrons, usually from a nuclear reactor, to bombard the nuclei of a sample material. At this energy range, neutrons can be absorbed by the nuclei, transmuting them into a new element while simultaneously exciting them. These new, excited nuclei de-excite with a characteristic gamma ray. This characteristic gamma ray will have the same energy for each initial nuclei. By performing a count of the irradiated sample with a energy sensitive detector, a intensity versus energy spectrum graph can be created with peaks corresponding to the nuclear composition of the sample. The intensity of these peaks indicates the concentration of the nuclei in question. Through comparison with a control of known concentration, the concentration of nuclei in a sample can be routinely determined with accuracy into the ppm level and occasionally the ppb level.

Certain nuclei do not lend themselves towards recognition with NAA. These nuclei are neutron transparent, having small thermal cross sections. Sometimes the nuclei produced through activation have quick decay times, on the order of seconds. A coolant for a nuclear reactor must have the first property, transparency, and therefore measurement the elemental composition of a coolant in a reactor would be nearly impossible through NAA. However, due to the absence of huge peaks normally found in chemical techniques, the most subtle impurities can be measured.

Table 4.4 shows the results of NAA performed at MIT on both open air salt produced from raw components and sampled salt from the secondary coolant loop in the MSRE. The secondary loop coolant, which has been stored and remelted in a stainless steel canister, has a decent amount of chromium and iron in it, both surpassing the purity specifications listed by Shaffer [5]. The 'Open Air Melt' was performed in a pure nickel vessel in a normal atmosphere, which most likely released some hydrogen fluoride and corroded the nickel slightly. This explains the presence of nickel in the salt, and the absence of iron and chromium.

Table 4.4: NAA of 'Open Air Melt Flibe' vs the ORNL 'MSRE Flibe', identical to those shown in Table 4.3. Nickel could not be measured due to more interference.

Element	MSRE Standards (ppm)	UW-Madison Average Concentration (ppm)	UW-Madison Calculated σ (ppm)	ORNL Average Concentration (ppm)	ORNL Calculated σ (ppm)
Cr	**25**	2.42	0.12	**66**	1.3
Fe	**100**	12.7	1.4	**215**	29
Ni	25	63.6	10.1	-	-

By using both NAA and ICP-OES, it seems a salt can be nearly completely characterized, except for oxygen, carbon, and water content.

Chapter 5

Nitrogen Trifluoride Analysis

5.1 Selection of Salt for Reactor Use

Initial experiments attempted to heat flinak in a Netsch thermal gravimetric (TG) instrument was used to investigate the degree of creep flinak would exhibit at temperatures between 500 and 800 °C. The instrument allowed for larger sample sizes (10 g), than the Seiko instruments (50 mg) described further below. At 800 °C, for instance, 0.5 g of flinak under a 200 mL min^{-1} purge of argon completely voided the nickel sample pans and corroded both the interior and exterior of the pan on its passage. The initial silvery nickel exterior was a dark rust color. The platinum thermocouples were fused to the nickel pan and were destroyed.

It was decided to observe the individual behaviors of heating the pure hydroxides that comprise. These reactions were initially attempted with the Seiko thermal gravimetric equipment to measure creep behaviors just above the melting points of the reactant salts: NaOH, KOH, LiOH.

5.2 Heating the Pure Hydroxides and Reaction with NF_3

Heating of NaOH in argon in a Seiko TG well past its melting point near 318 °C resulted in its dehydration and the formation of sodium peroxide, Na_2O. The material fumed, but was not lost significantly from the sample pan, even at 800 °C.

Heating of pure KOH in argon up to its melting point near 406°C caused significant creep of the hydroxide and consequently loss of mass information.

Upon heating of pure LiOH in argon past its melting point (462 °C) to 500 °C all of the material left the sample pan and fused the sample pan to the balance arms. The sample pans and balance arms were recovered by reacting the fused salts in dilute nitric acid and then water. Fig. 5.1

compares a good (top arm) balance arm without the sample pan and a pan fused to the arm from creep of the molten salt.

Figure 5.1: Creep of heated salts from the Seiko sample pans and fusing/corrosion of sample pans.

The reaction of NaOH and NF_3 initially appeared to be amenable to study in the TG apparatus. However the reaction caused extensive corrosion of the sample balance arms. The corrosion could not be removed and eventually destroyed the balance arms. The reaction was thus not attempted for the potassium or lithium hydroxide.

5.3 Corrosion of the Experimental Setups

The thermal gravimetric apparatus were badly bruised by the use of the fluorinating gases at temperatures exceeding 400 °C and the pure salts such as NaOH, NaF, or the flinak itself. The most susceptible parts were the coated balance arms that house the Pt/Rh thermocouples, which were $3500 to replace. Three pair were destroyed looking for the lowest temperature conditions that the reactions could be run at. It was decided to shift the experimental work to a vacuum line.

The manifold in Fig. 5.2 allows delivery of several fluorinating gases: NF_3, F_2, HF, ClF_3, and other gases O_2, H_2, Ar, He. At the Pacific Northwest National Laboratory a procedure and Chemical Use Documentation are required to safely test and use such equipment. There was a

Figure 5.2: Dual manifold for gas delivery to vacuum line: NF_3, F_2, HF, ClF_3, H_2, O_2, Ar, He.

schedule and labor cost associated with setup and writing. Fortunately, some of the corrosion repair and setup costs were shared with other projects that also use the fluorinating gases. The setups are shown in Fig. 5.2-5.4 and discussed in the experimental section at the end of this letter.

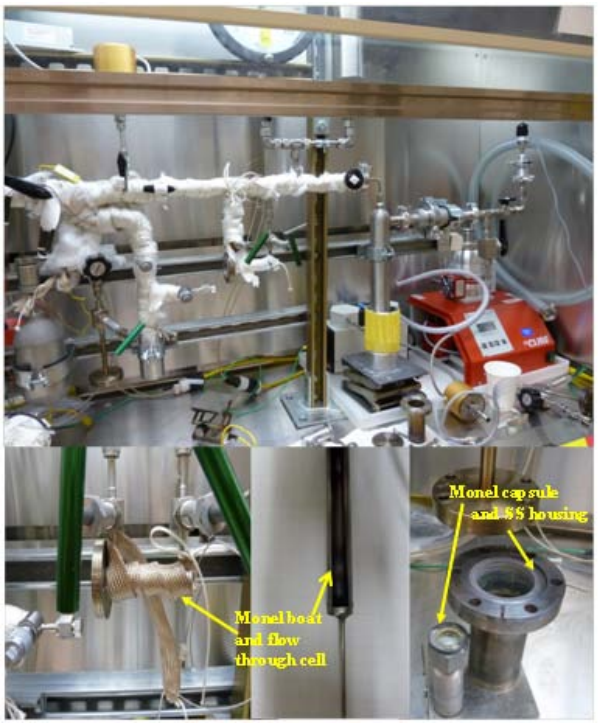

Figure 5.3: A short vacuum line with high temperature/low corrosion functionality.

5.4 Flow-Through Experiments

The small boat-in-a furnace apparatus shown in Fig. 5.3 was constructed to attempt flow through experiments with NF_3 and flinak. The setup best approximated the simplicity of the TG apparatus. The boat was made from Monel and the furnace was made of 316 stainless steel which stands up to fluorination reactions with NF_3 on the vacuum line up to 700 °C. The volume of the boat was 20 mL. The boat was loaded with dry 0.12 g KOH and placed into the furnace and the end flange bolted on. The line and furnace were leak checked at 100 psi. The KOH was heated to 500 °C and then cooled. The KOH was retrieved from the boat on cooling. The experiment was repeated with a static charge of 1 atm of NF_3/Ar in an approximately 50/50 ratio. On cooling, the interior and exterior of the boat was shiney but all of the KOH had crept from the boat as KF and it was recovered from the bottom of the furnace tube. Several more attempts using the boat arrangement indicated again that at a temperature required to melt and react the salts with NF_3, a larger vessel or fully closed system was required.

5.5 Static Experiments in Stainless Steel

More successful and interesting experiments began with the use of a larger volume 316 stainless steel vessel without the use of the Monel capsule. The vessel was loaded directly with about 0.1g of NaOH, KOH, or LiOH. The experiments were repeated using a twofold excess of the molar equivalent of NF_3 to pure hydroxide. For instance the reaction of sodium hydroxide proceeds in the following manner.

$$3NaOH + 2NF_3 = 3NaF + 3HF + 3/2O_2 + N_2(-475.7\ \text{kJ mol}^{-1}\text{Na}) \tag{5.1}$$

The cell was heated to 450 °C with a static pressure of up to 50% NF_3/Ar and a total pressure of 2.5 to 5.0 atm for three hours at first, and later this was reduced to 10% NF_3 and one hour duration.

In the first experiment the reaction vessel was cooled to room temperature. When the vessel was opened the cell floor and walls were a bit corroded and the cell appeared to be dry and free of any white NaF or NaOH. Initially it appeared that the salt had crept out of the vessel and perhaps up into the vacuum line. About 1 mL of water was used to wash the walls and this solution placed into a capped vial. The color of the solution was brown with some iridescent materials clinging to the vial walls. The pH of the water was about six. This was clearly too low for the presence of excess NaOH.

The experiment was the first confirmation that the pure hydroxides had been removed by treatment with NF_3. After a couple of hours, the dampness in the cell had dried. A white precipitate covered the bottom of the cell. The solubility of NaOH in water is quite high (110 g L^{-1}) 1 and that of NaF is lower (40 g L^{-1}) 1. The water wash fortunately had not removed all of the product from the cell. The question is where was the salt product when the cell was first opened? The answer is, it had formed a fine film or had leached into the cell walls on reaction. The water wash leached the salt from the walls. Equation 5.1 suggests that HF vapor is formed during the reaction. The vapor is under pressure (2-5 atm) during the reaction. The vapor pressure would drive material creep and may have acted to force the sample to spread out onto the cell walls.

The water released from the cell walls on heating or perhaps as physisorbed water on the salt materials would also add to the overall vapor pressure in the system.

$$H_2O(l) = H_2O(g) \tag{5.2}$$

$$2NF_3 + 3H_2O(g) = 6HF + N_2 + 3/2O_2 \tag{5.3}$$

The reaction was repeated with KOH and LiOH with similar results. How, colored products were observed for the KOH-NF_3 system, as shown in Fig. 5.4. Because FeF_3, CrF_3, and NiF_3 are green salts, SEM micrographs with their EDAX spectra were acquired. The EDAX spectra in

Fig. 5.5 indicted that each metal was present from corrosion of the walls of the 316 container and that they all appeared to have leached preferentially using KOH, producing the green coloration. The experiments were reproducible in terms of the color as more experience was gained using the apparatus and more pure salts produced. For the reactions of NF_3 with NaOH, KOH, and LiOH, white salts were observed with brown to reddish flakes from the stainless steel vessel and the exposed interior portion of the (sealing gaskets). Because the flakes initially contaminated the salt products, it is not clear from the EDAX spectra of several products what was actually leached versus mechanically mixed.

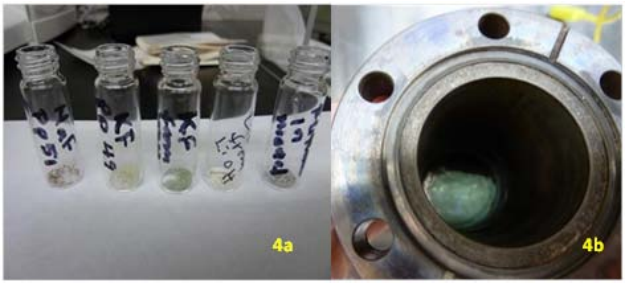

Figure 5.4: 4(a) Colored products from corrosion of stainless steel reaction vessel at 450 °C under exposure to NF_3 and 4(b) the green salt specifically from reaction with KOH and NF_3.

Corrosion of the stainless vessel was expected, however, the preferential leaching of the vessel to produce the green salt was not expected, nor was the behavior being particular to KOH expected. Another look at this is shown in Fig. 5.4b. The reaction of NF_3 and KOH returned about 100% yield of this new green salt by mass. At this time, it is believed that changes in the total pressure at 450 °C and the NF_3/Ar ratio may be responsible for the observed preferential leaching.

Powder diffraction data were collected on the salts produced in the stainless steel vessels but it is thought that the iron content in the salts precluded any signal due to X-ray fluorescence from the iron.

A final note concerning the mixed product salts from reaction of NF_3 with the pure hydroxides. In each case dry salts did not exhibit any deliquescence. EDAX spectra, as shown in Fig. 5.5, of the salts indicated high fluorine concentration and little to no oxygen concentration. The salts were

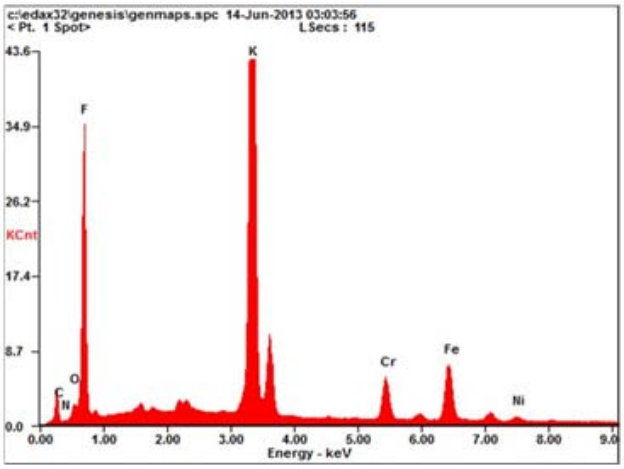

Figure 5.5: EDAX spectrum of the green salt from the reaction of NF_3 and KOH.

dried in air at 150 °C to ensure that free HF was not adhering to the salt. The product salts were then placed in deionized water to observe the pH might be used to indicate the presence of free hydroxide. In no case was free hydroxide present as indicated by the pH data in Table 5.1. In fact in all cases the, pH was lowered from the expected values considerably.

The water chemistry is interesting in light of trying to understand if it might be used as an indicator of the extent of the fluorination reaction.

5.6 Static Experiments in Monel

The reaction conditions were of these salts and flinak were repeated in the Monel capsule arrangement shown at the bottom of Fig. 5.3. The capsule had a sintered filter that allowed the NF_3 gas in, but maintained the creep of material out of the capsule to a minimum. The purpose of the experiments progressed to understand if a graded doping of the flinak with hydroxide could be used to see small changes in the XRD powder pattern of the product salts. Good to theoretical yields of product salt were obtained using the closed capsule and less coloration of the product salts was observed. Additionally, reasonably good XRD data were collected on the product salts.

5.7 XRD Data

XRD powder patterns although not very sensitive to OH- and water concentration (1%) but turned out to be helpful to understanding the reaction of NF_3 with flinak and perhaps some of its corrosive behavior. It should be recognized that in these experiments, a large void volume was accessible for the flinak and its constituent salts to migrate to. This may not be the case if the static volume were completely filled as one would expect in an operational condition. In this case while the surface corrosion would have similar chemistry same the impact on the large volume of flinak would not as extensive . That is only some small volume of the salt would be impacted by the corrosion for short corrosion periods. For long corrosion periods these data might still be relevant.

Figures 5.6-5.11 show the XRD powder patterns from the reaction of NF_3 with flinak constituents and flinak itself under flooding conditions using the worst case scenario product; a "flinak hydroxide". That is, the initial Na, Li, K were used as pure hydroxides as described above. The reactions were done on the vacuum line and using the Monel containment. The hydroxide salts were reacted with NF_3 at 450 °C. The large background at low goniometer angle (two theta axis) is from scattering off the amorphous glass capillary tube that held the sample.

Figure 5.6 and 5.7 show the result for the pure Li and Na hydroxides which were fluorinated to 100% to the sensitivity of the XRD experiment. Hydroxides and water hydrates generally appear at greatest intensity at low angles. The match in both cases is for the pure fluoride, LiF and NaF, respectively. The potassium salt showed the same behavior.

Figure 5.8 and 5.8 show the XRD patterns for pure flinak and flinak reacted with NF_3 at 460 °C. The notable feature of the pure flinak is that it can be described simply as an admixture of the three component fluorides. In the NF_3-reacted spectrum, the prominent features associated with KF have been removed entirely from the spectrum (see ~33.5, and ~49 two-theta) and a new feature near ~42.5 has grown in. The new feature is associated with Ni and Li. It is thought that at this time the KF was visiting the walls of the container and did not revisit the final salt unless it

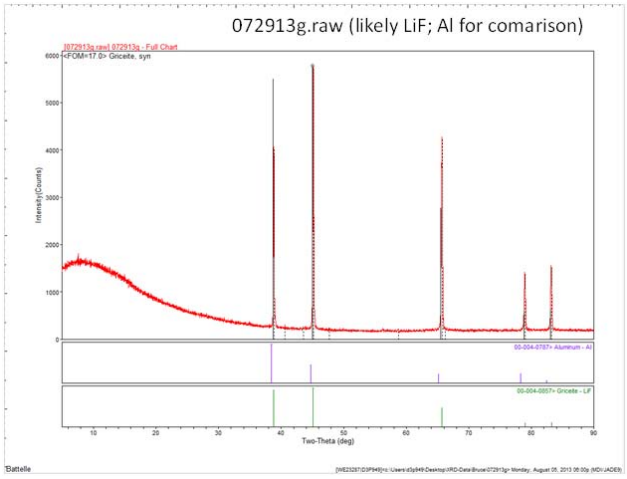

Figure 5.6: XRD powder pattern of the reaction of pure LiOH and NF_3.

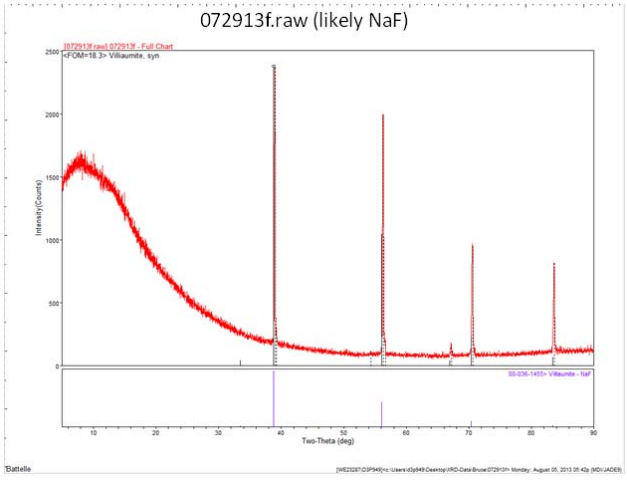

Figure 5.7: XRD powder pattern of the reaction of pure NaOH and NF_3.

was forced to in some fashion. For instance, in previous experiments water was used to wash the walls of the container and that released the potassium as seen in Figure 5.5.

In Figure 5.9, note the background increase at high goniometer angle. This is due to an X-ray fluorescence signal. Here it implies the presence of iron, likely from the Monel container even though it is in Monel at lower percentage. That is, some feature of the reaction, perhaps HF production, has leached iron out of the container walls.

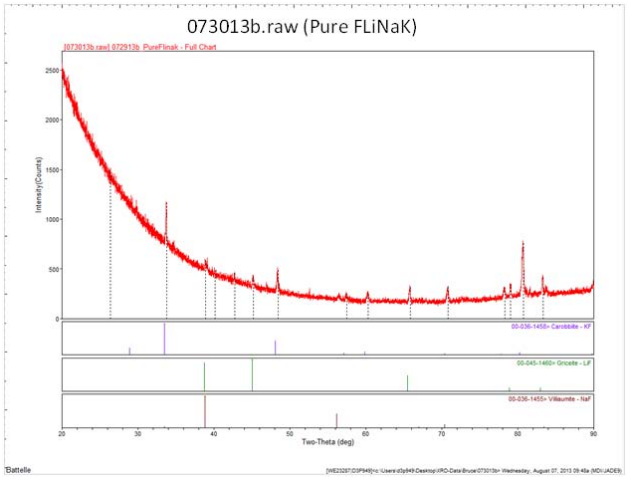

Figure 5.8: XRD powder pattern of pure flinak.

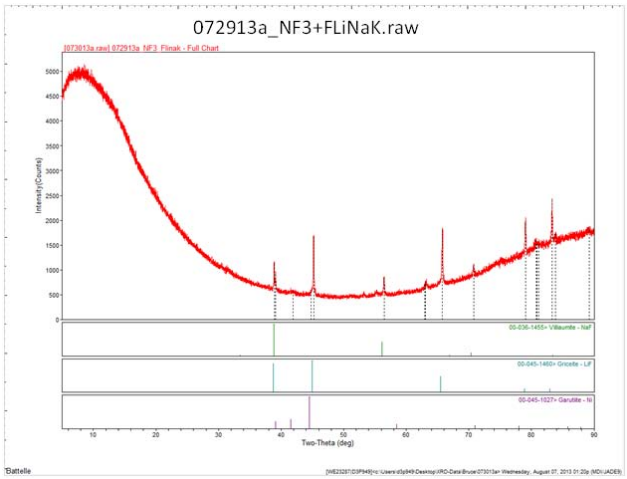

Figure 5.9: XRD powder pattern of the reaction of pure flinak and NF_3.

Figures 5.10 and 5.11 demonstrate the effect of added hydroxide on the reaction with NF_3.

A comparison of Figure 5.9, 5.10, and 5.11 indicate that the spectrum does not change much except for an increased fluorescence background at high angle. This and the broad lines relative to Figure 5.9 suggest greater corrosion of the Monel cell walls. Also, in both Figures 5.10 and 5.11, corrosion by added hydroxide acted to reintroduce the potassium fluoride signature near ~33.5 two-theta. The one near ~49 two-theta was initially less intense than the lower angle peak and is very weak here. Along with these, new possible species have broadened the peaks and are consistent with lithium and potassium nickel fluoride. Chromium is likely in the spectrum as well but the broadness of the lines and their low intensity make it difficult to confirm it presence.

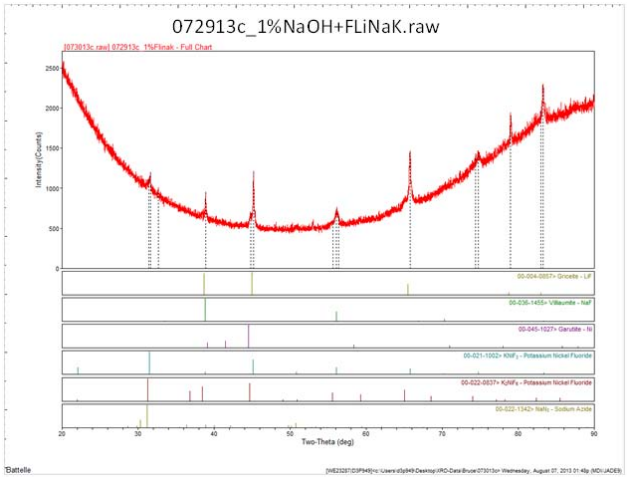

Figure 5.10: XRD powder pattern of the reaction of $NF_3$with 1Wt%NaOH + flinak .

5.8 Analysis of Impurity Hydroxide or Oxide in Water

Intentional hydrolysis of flinak or the components of flinak, for instance the strong electrolytes NaF, KF, and LiF each dissociate in water:

$$NaF = F^- + Na^+ \tag{5.4}$$

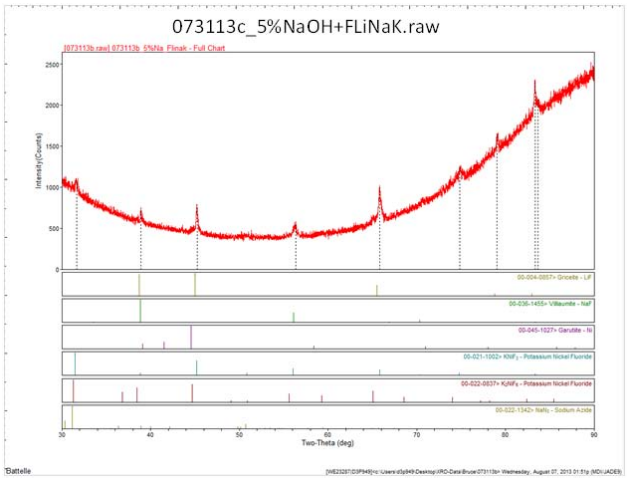

Figure 5.11: XRD powder pattern of the reaction of $NF_3$with 5Wt%NaOH + flinak.

The Na, K, or Li cations do not react with water but the fluoride ions do to some extent:

$$F^- + H_2O = HF + OH^- \tag{5.5}$$

The pH data collected in Table 5.1 indicate the extent of the hydrolysis. A 0.05 M KF or NaF salt solution dissociates to give about the same pH. For more dilute solutions, the pH decreases and for added hydroxide the pH of the dilute solutions responds to small additions of hydroxide. The flinak salt likely dissociates to similar extent as NaF and KF but it appears from Table 5.1 that a higher concentration of it is required to establish weakly basic conditions. This suggests that an impurity may be present in the as received flinak sample to begin with. The effect of impurities is discussed below.

The data suggest an approach to measuring the free hydroxide concentration in the product salts in water. If the fluoride concentration is low, as was desired, one measures in solution a weakly basic solution with pH between 8 and 9. Consequently, if excess OH- were present a sharp increase in pH would be measured in solution. If 0.001 mol NaOH was added to 1L of a non-buffered solution, the pH change would be from near 8 to above 11.

If the fluoride concentration were higher, a buffer solution would form. A pH change due

Table 5.1: pH response of test solutions of pure fluorinated substances in water and with addition of free hydroxide.

Pure Substance	Mass (g)	Salt (M)	pH	pH 0.02M NaOH	pH 0.052 M NaOH	pH 0.083 M NaOH
NaF	0.0051	0.041	8.357		10.347	
NaF	0.0097	0.077	8.675			11.209
NaF	0.022	0.175	8.887	9.698	10.173	
NaF	0.0496	0.395	9.273		10.413	
NaF	0.0499	0.397	9.277			11.141
NaF	0.05	0.398	9.195			11.745
NaF	0.0514	0.409	9.28			
NaF	0.1	0.796	9.4			11.78
NaF	0.1066	0.848	9.525			
KF	0.0505	0.402	9.494	9.542	9.601	
LiF						
Flinak	0.0028	0.011	6.55			
Flinak	0.011	0.042	7			
Flinak	0.1	0.378	8.58		9.12	11.5

to the presence of base would be difficult to measure until the buffering capacity of the solution was exceeded. In effect, hiding the very effect which was being examined. Consequently, a test solution should be dilute and the presence of free hydroxide measurable. Inspection of Table 5.2 indicates, however, something else was occurring when dilute solutions of the product salts were prepared. Instead of basic solutions as the test cases in Table 5.1 suggest, acidic ones were obtained. Additionally, it was observed that the solutions acted as a buffer to the addition of the same quantity of NaOH. Thus, the base hydrolysis in Equation 5.2 appears to be dominated by some other process most likely one that results in acidic hydrolysis.

Nevertheless, the buffering effect appears quite regular and might still be used for measurement of the extent of the fluorination reactions if a model of the solution chemistry were developed.

Table 5.2: pH response of solutions of pure fluorinated substances in water and with addition of free hydroxide.

Product	Mass, (g)	pH	pH 0.02M NaOH	pH 0.052 M NaOH
$NaOH/NF_3$	0.0207	6.369	6.456	6.575
KOH/NF_3	0.02	5.112	5.181	5.268
KOH/NF_3	0.0185	4.907	5.002	5.078
$LiOH/NF_3$	0.0199	5.252	5.332	5.503
Flinak $/NF_3$	0.001	4.35		
Flinak $/NF_3$	0.0125	4.76		
Flinak $/NF_3$	0.0215	4.985	5.044	5.112

The presence of corrosion products in the reacted salt for instance presents one such chemical wrinkle. If contaminant salts were M = Cr, Fe, or Ni as expected, each of these behaves in a slightly different manner with regard to their hydrolysis. In general, it is expected that their hydrolysis would result in formation of covalent hydroxides that are more acidic thus lowering the pH and likely creating the buffering effect posed by the data in Table 5.2.

$$M(H_2O)_6^{3+} + H_2O \leftrightharpoons M(OH)(H_2O)_5^{2+} + H_3O^+ \tag{5.6}$$

The low solubility of CrF_3, FeF_3, or NiF_3 may or may not play a factor in the hydrolysis measurement of hydroxide, as their fluorination in the presence of hot water vapor or hot HF could produce known compounds such as $[Cr(H_2O)_6]F_3$, which is thermally stable to 1200 °C and is soluble in water.2

$$Cr_2O_3 + 6HF + 9H_2O \rightarrow 2[Cr(H_2O)_6]F_3 \tag{5.7}$$

Regardless of the chemistry, it appears that a well-defined empirical pH data set acquired from the response of the reacted molten salt to hydroxide and acid could be modeled and the model used to calculate excess hydroxide perhaps to an order of magnitude lower than surface and other spectroscopic measurements.

Finally, the cost of a sensitive mass measurement of hydrogen was examined as an approach to measure free hydroxide as water in the fluorinated salt. In general, the mass measurements of water and hydrogen are confounded by the presence of water in most measurement systems. A special H_2/ He mass spectrometer was available at PNNL to attempt a low level water analysis. In this experiment, water vapor from the heated fluorinated molten salt would be heated and converted through a metal reduction reaction to hydrogen gas. The gas would be collected and analyzed in the hydrogen mass spectrometer. The cost of understanding the details of quantification of water conversion to hydrogen and collection and finally its overall efficacy led us to not attempt the approach.

5.9 Flinak Evaluations

Powdered flinak was used as received from the University of Wisconsin - Madison. Pure hydroxide salts and flinak were reacted with NF_3 a nickel sample pans. The salts were exposed to 10% NF_3/Ar at 200 mL min^{-1} in a Seiko 3200 series thermal gravimetric (TG) apparatus housed in a fumehood. The TG instrument, adapted and modified for radiological and fluorination studies, has been reported elsewhere [63].

A Netsch thermal gravimetric (TG) instrument that allowed for large sample size up to 10 g was used to investigate the degree of creep flinak would exhibit at temperatures between 500 and 800 °C. The instrument allowed for larger sample sizes (10 g), than the Seiko instruments (50 mg) described further below. Pure nickel pans (10 mL) were prepared from house stocks of nickel.

Flinak was doped with NaOH by adding the 0.1 g flinak to 1 mL of an appropriate concentration of hydroxide by weight (0.5, 1, 5 Wt%) in water. The suspension was stirred and the liquid evaporated slowly to avoid spatter of the solids.

The gas manifolds in Fig. 5.2 were attached to a short vacuum line with high temperature functionality as shown in Fig. 5.3. The manifolds delivered a range of gases; NF_3, F_2, HF, ClF_3, H_2, O_2, Ar, He, for fluorination and other uses. The vacuum line as shown in Fig. 5.3 was wrapped in heat tape for materials transport up to temperatures of 700 °C. High temperature and corrosion resistant valves were used as required. A corrosion resistant pump preceded a turbo pump and a solids filter cartridge removed corrosive by-products that were not trapped in the coolant trap. Two small attachments are indicated on the line, which allowed reactions of gases with the salts in 1) atmospheric flow-through mode and 2) in high pressure, static mode. The flow through cell shown at the bottom left of Fig. 5.3 housed a small Monel boat that contained the heated salts and was sealed with a conflat flange using a Ni or Cu gasket. For the static, higher pressure setup, a small, sealable Monel capsule, shown at the bottom right of Fig. 5.3, contained the heated salts but allowed gases in and out through a sintered nickel filter. The capsule was positioned inside a high pressure, 73 mL container that was sealed with a conflat flange using a Ni or Cu gasket. The threads of the Monel capsule were enlargened to prevent thread seizure from high temperature use.

X-ray powder patterns were acquired using a Rigaku Ultima IV X-ray diffractometer to aid in determination of the stoichiometry of the fluorinated products. Milligram quantities of the samples were placed in 7-mm capillary (Charles Supper Co, Natick, MA) tubes and epoxied closed. The capillary tubes were encapsulated in polyester heat shrink tubing (Salem, NH). Data was acquired between 2 and 60 degrees 2-theta on a capillary attachment with spinner capability. X-ray

tube operating conditions were 40 kV and 44 mA. Phase identification was conducted using JADE MDI search match routines using the ICDD database 2009. Samples were rotated at 40 RPM . The morphology and elemental content of reacted salts were characterized using scanning electron microscopy (SEM) coupled with energy dispersive X-ray spectroscopy (EDX) and transmission electron microscopy (TEM). A pipette containing a small amount of methanol was used to extract a few particles. These were then deposited on a sticky carbon tape, coated with conductive carbon and analyzed with an FEI (Hillsboro, OR, USA) Quanta250 field emission gun scanning electron microscope equipped with an EDX (EDAX Inc., Mahwah, NJ) compositional analysis system running GENESIS analysis software. Microscopic images were obtained under secondary and backscattered electron imaging conditions, single point, line scans, and X-rays maps were collected.

Chapter 6

Modeling of Fluoride Salts

6.1 Introduction to Modeling

While there have been extensive thermo-kinetic properties of molten salts obtained in the 1960s, there continues to be a need to model of molten salts, both to validate the experimental data where there is significant scatter and also to generate the data when no experimental measurements were made. For these reasons, classical interatomic potential molecular dynamics (IPMD) has been used for modeling of various molten salt systems including the flibe (FLiBe; Li_2BeF_4) and flinak (FLiNaK; eutectic LiF-NaF-KF) salts [64, 65, 66, 67, 68, 69, 70, 71]. Although there has been a slight variation in the forms of interatomic pair potentials used, the Tosi-Fumi (or Born-Huggins-Meyer) type potential was typically used to model most of the molten salt systems [72, 73, 74]. Parameters in these interatomic potentials were determined primarily by fitting the experimental and/or first-principles data.

In this project, instead of using interatomic potentials and IPMD, we employ first-principles molecular dynamics (FPMD) (also referred to as ab-initio molecular dynamics, or AIMD) directly to model the molten fluoride salt at high temperature. Due to the rapid growth of computer performance, FPMD can now be practically used in modeling of various liquid systems, and has previously been applied to the flibe salt [75, 76, 77, 78, 79, 80, 81]. This previous work on flibe salt was conducted using the Car-Parrinello method, which is different with Born-Oppenheimer MD used in this study, and primarily focused on the diffusion at a fixed volume of 2 g cm^{-3} [82]. FPMD has several advantages over IPMD, including the accuracy of full quantum mechanical calculation of the forces, the flexibility to study any system without needing to first fit potentials, and the ability to study electronic properties (e.g., spin state) that are not accessible to potentials.

In this project, two representative fluoride salts for nuclear application were studied by using FPMD, with goals of both assessing FPMD for these salts and enhancing our knowledge of key thermodynamics and kinetic properties of the salts. The salts are flibe, which is considered as a primary coolant or fuel salt, and flinak, which is a candidate as a secondary coolant in fission reactor designs. Firstly, details of computational methods to model the molten fluoride salt systems through FPMD are addressed. Basic thermo-kinetic properties were calculated and compared with the experimental measurements to validate the FPMD modeling of fluoride salts. Then we focused on the modeling of the chromium solute interactions within the salt which is a major corrosion product of structural materials in fluoride salts at high temperature.

6.2 Details of First-Principles Molecular Dynamics Simulation

Initialization of the FPMD follows the approach from Bengtson et al. [80]. Initial configuration of ions for molecular dynamics was prepared by packing ions randomly in the simulation cell using Packmol package [83]. Then, IPMD simulation with the LAMMPS simulation package was performed to obtain a reasonable input configuration of ions for FPMD [84]. This step ensures the system to be at equilibrium before the FPMD simulation. Interatomic potential parameters for pure flibe and flinak were obtained from previous IPMD studies without taking Tang-Toennies dispersion damping term which can be replaced by a constant value of 1.0 [66, 70, 85]. The potential parameters between solute ions and constituent elements of flibe and flinak salts were approximated following the method detailed in Larsen et al. [86]. We should note here that the IPMD simulation was merely employed as a preprocessing step to set up the initial configuration prior to the FPMD simulation, and thus the approximation of potential parameters should not affect the final results. Detailed procedures for geometry optimization using IPMD was addressed in the previous study [80]. After the IPMD runs, the molten state of the salt was verified by analyzing the radial distribution function (RDF) of atoms in the simulation cell. The RDF were compared with

those reported in the literature data [67]. We consider simulation cells for flibe comprised of 28 Li atoms, 14 Be atoms, and 56 F atoms (total 98 atoms) and flinak comprised of 23 Li atoms, 6 Na atoms, 21 K atoms, and 50 F atoms (total 100 atoms). The cell sizes are expected to be adequately converged with respect to the properties evaluated in this work based on a similar study on the Li-K-Cl system [80].

The FPMD simulations for molten fluoride salts have been performed with density functional theory (DFT) as implemented in the Vienna Ab-Initio Simulation Package (VASP) version 5.3.2 [87, 88, 89]. The molecular dynamics simulations are done in a statistical ensemble of fixed particle number, volume and temperature (NVT) using a Nose-thermostat [90]. The Perdew-Burke-Ernzerhof (PBE) exchange-correlation functional was implemented in the generalized gradient approximation (GGA) [91, 92]. Dispersion forces are included using the vdW-DF method with the optB88 functional [93]. The calculations used projector augmented wave (PAW) technique and a plane wave basis set with an energy cutoff of 600 eV [89, 94]. A 1×1×1 k-point mesh was chosen to be used in FPMD simulations, yielding an error of less than 1 meV/atom with respect to k-points. Time step for the FPMD simulations were chosen at 0.001 ps (1 fs) to ensure an energy drift less than 1 meV/atom-ps for pure salts and 2 eV/atom-ps for solute systems.

FPMD simulations were performed for pure molten fluoride salts (flibe and flinak) at multiple simulation temperatures (T=973 K, 1223 K, 1423 K) to obtain a temperature dependent thermo-kinetic properties. To study the behavior of solute ions in the salt, solute fluoride was introduced in the pure salt to simulate the behavior of solute ions. For example, Cr atom, CrF_2 and CrF_3 molecules were introduced in the pure salt to simulate the behavior of Cr^0, Cr^{2+} and Cr^{3+} ion, respectively. When solute ion is introduced into the salt, spin polarized calculations were conducted to accurately describe the effect of solute system. The pressure of the system at a finite temperature was determined by taking the sum of the external pressure and the kinetic pressure from the output of the VASP-MD. The standard error of the mean from correlated molecular dynamics data was determined from the auto-covariance function as can be found in the work of Alexopoulos [95].

6.3 Evaluation of Thermo-Kinetic Properties from FPMD

The equation of state (EOS) analysis was conducted to determine pressure (P) vs. volume (V) for a series of volumes at a given temperature which were calculated from the FPMD simulations. The P(V) dependence is then fit to a third-order Birch-Murnaghan equation of state to obtain equilibrium volume, density and bulk modulus [96, 97]. From the temperature dependence of the density, coefficient of thermal expansion (CTE; α) was calculated using Eq. (6.1).

$$\alpha \equiv \frac{1}{V}\left(\frac{dV}{dT}\right)\Big|_P = -\frac{1}{\rho}\left(\frac{d\rho}{dT}\right)\Big|_P \tag{6.1}$$

where V is the volume, T the temperature, and $\rho$the density. The error in each property was estimated according to the standard error propagation method during the EOS analysis.

The self-diffusion coefficient was calculated from the slope of the mean squared displacement (Eq. 6.2 of the center of mass of atoms of the same type as a function of time, according to the well-established Einstein relation presented in Eq. 6.3.

$$MSD = \left\langle \frac{1}{N}\sum_{i=0N}\left(r_i(t_0+dt) - r_i(t_0)\right)^2 \right\rangle = \frac{1}{N\cdot n_t}\sum_{i=0N}\sum_{j=0n_t}\Big(r_i(t_j+dt) - r_i(t_j)\Big)^2 \tag{6.2}$$

$$D = \frac{1}{6}\lim_{t\to\infty}\frac{d}{dt}\left(MSD\right) \tag{6.3}$$

In order to calculate the self-diffusion coefficient of constituent elements of fluoride salt, FPMD simulations were conducted at the equilibrium volume for more than 12,000 time steps (total 12 ps simulation) with about 100-atom simulation cell (98 atoms for flibe and 100 atoms for flinak) at the temperatures of 973 K, 1223 K, and 1423 K. Four equal size of blocks were used to estimate the standard error of the mean diffusivity using the block averaging method [98]. Details of this methods are addressed in the previous study [80].

The self-diffusion coefficient of solute ion in fluoride salts was also calculated from the FPMD

simulations at 973 K. Unlike the case of the solvent constituents of the molten salts, the accuracy of the diffusion coefficient of solute can be quite limited as in this case there is only one solute introduced into the simulation cell. Therefore, a longer simulation is necessary to isolate the effect of oxidation states on diffusivities in the salts. For longer simulations, we reduced the size of the cell to 63 atoms for flibe (18 Li, 9 Be, and 36 F atoms) and 52 atoms for flinak (12 Li, 3 Na, 11 K, and 26 F atoms). These systems sizes are small enough that one must be concerned with periodic cell size effects influencing the predicted solute diffusivity. However, testing with IPMD showed that the effect of the reduced system size is negligible on the calculated solute diffusion coefficients.

For solutes detailed local structural studies were performed. The radial distribution function analysis was conducted from the FPMD trajectory to study the local structure surrounding solute ions in the fluoride salts. The first-shell coordination number of solute ion with the surrounding F anions was estimated by integrating the radial distribution function from zero to the first minimum. We refer to the integral of the RDF as the neighbor function (Eq. 6.4)

$$N_{\alpha\beta}(r') = 4\pi \cdot \rho_\beta \cdot \int_{0r'} r^2 g_{\alpha\beta}(r)\, dr. \tag{6.4}$$

where $g_{\alpha\beta}(r)$ is the RDF between species α and β, and $\rho_\beta$the average number density of species β.

6.3.1 Effect of XC-Functional and Dispersion

In DFT calculations, the exchange-correlation functional (xc-functional) is used to calculate the electron-ion interaction. It is known that the LDA (local density approximation) xc-functional underestimate the lattice constant of solid system about 1% and GGA overestimate the lattice constant about 1% [99]. In this study, three exchange-correlation functionals were tested, initially without introducing the dispersion interactions. Firstly, GGA/PBE without dispersion was used to estimate the equilibrium volume of molten salt at multiple temperatures and it overestimates the

equilibrium volume by about 9% (18%) compared to the experimental V_0 from Janz (Ignat'ev et al.) (Fig. 6.1) [100, 101]. Although the difference is quite large compared to errors in solids, this difference can be explained by low bulk modulus of liquid salt (~10GPa), which means that even small errors in energy can yield large errors in volume. The LDA without dispersion interaction was also tested at 973K and it gives an estimate of V_0 lower than any of the experimental data, as shown in Fig. 6.1. Only one simulation at 973K was conducted with the LDA xc-functional because introducing the dispersion will lower the estimation of V_0 further and LDA was already predicting a significantly too low a volume. The PBEsol exchange-correlation, which usually shows a good estimation of the lattice constant for solid systems, especially for alkali metals and alkali halides, was also tested without dispersion [102]. PBEsol gives a better estimation of the volume at multiple temperatures (about 3% (11%) larger than the V_0 from Janz (Ignat'ev et al.) [100, 101].

For the accurate prediction of thermo-kinetic properties, van der Waals (vdW) dispersion interaction was included in the FPMD modeling of molten salt systems. Although general density functional theory cannot describe the van der Waals dispersions, several methods have been developed to be used in first-principles modeling [93, 104]. For the VASP-MD simulations, currently (VASP version of 5.3.2) two different methods can be used to include the dispersion interaction. Those are the DFT-D2 of Grimme [105, 106] and vdW-DF of Langreth and Lundqvist et al [93, 104]. The DFT-D2 method adds a semi-empirical dispersion term, which can be described from a simple pair-wise force field, to the DFT energy. Parameters (C6 dispersion coefficient and vdW radii) used in this force field were empirically determined and provided for the elements up to the atomic number of Xe (atomic number = 54). The vdW-DF method, on the other hand, uses a non-local energy term which approximately accounts for the nonlocal electron-electron correlations. Fig. 6.1 also shows a comparison between two dispersion methods for flibe system with GGA/PBE functional at multiple temperatures. Although both methods are within the range of experimental measurements, we decided to use the vdW-DF method instead of DFT-D2 in this study, because the

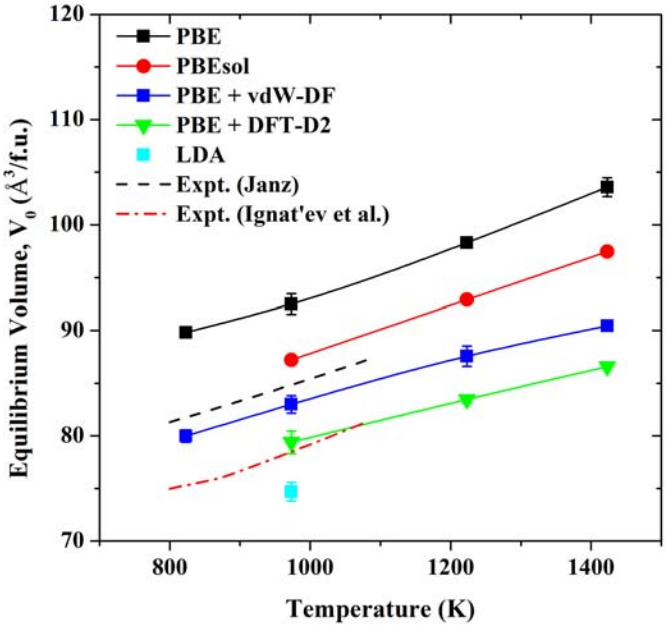

Figure 6.1: Calculated equilibrium volume of flibe from the FPMD simulations as a function of temperature with different exchange-correlation functionals and with different dispersion methods. Experimental correlations for density of Janz and Ignat'ev et al. for flibe salt from literature are shown together for comparison [100, 101, 103]. Error bars represent two sigma standard error of the mean.

vdW-DF method is a non-empirical method and hence can describe elements without specifying pre-determined parameters.

By employing the van der Waals dispersion between atoms in FPMD simulations, the system pressure is decreased by more than 1GPa in flibe system and hence the equilibrium volume is decreased by about 9-13% compared to the V_0 estimates without dispersion interaction. Therefore, PBEsol and LDA with the dispersion interaction will give a poor estimation of equilibrium volume for molten fluoride salts. This trend with dispersion interaction is also observed in molten LiCl-KCl system [80]. In this study, therefore, the vdW-DF method with PBE functional is used in FPMD modeling of molten fluoride salts. For the vdW-DF method, several different optimizations of exchange functional have been made up to date. Among these optimizations, the optB88 functional is chosen to be used to study the molten fluorides, because it provided a good estimate for the lattice constant for solid alkali halides in previous literature [93].

6.3.2 Thermodynamic Properties of Pure Fluoride Salts

The aim of this section is to benchmark the FPMD simulations against known molten fluoride salt thermodynamic properties to the extent possible and also provide additional new thermodynamic data where experimental values are missing or unreliable.

Equilibrium Volume, Density and Bulk Modulus

The density is an essential and very useful thermodynamic property for fluoride salts. Several correlations for density vs. temperature for flibe and flinak have been developed from experimental measurements [103]. In order to obtain a correlation for density (density vs. temperature) from purely first-principles, equilibrium volumes (V_0) of molten salt system at various temperatures were determined from EOS calculations. Fig. 6.2 shows an example of the EOS analysis for flibe at 973K used in this study, performed as described in the Methods Section. The comparison of

the EOS fit and the experimental data of Janz and Ignat'ev et al. shows that the predicted V_0 is within the range of the experimental measurements [100, 101]. The same procedure was applied to molten flibe and flinak salt systems at three different temperatures (T=973 K, 1223 K, 1423 K) and additionally at T = 823 K for flibe.

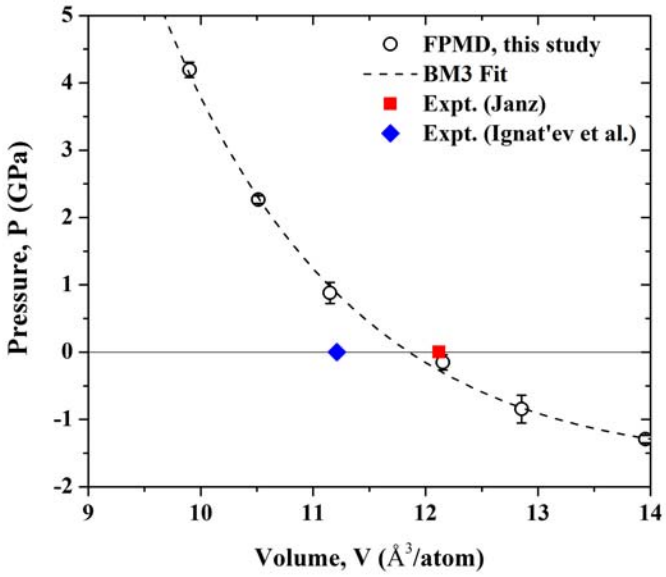

Figure 6.2: The third-order Birch-Murnaghan equation of state fit of pressure-volume data of flibe at 973 K which was obtained from the FPMD simulations. Experimental V_0 are also shown for comparison. Error bars represent one sigma standard error of the mean.

Fig. 6.3(a) and (c) show the equilibrium volume of flibe and flinak, respectively, including error bars as a function of temperature. Experimental equilibrium volumes for flibe were predicted from the correlation for density of Janz and Ignat'ev et al. (800K–1080K) from the literature [100, 101, 103]. For flinak, the three experimental correlations for density of Grele et al. (d1), Vriesema et al. (d2) and Janz et al. (d3) given within Sohal et al. are shown in the figure for comparison [103, 107, 108, 109, 110, 111, 112]. In addition, one correlation for density (d4) of flinak obtained from IPMD simulation is also included for comparison [70].

From the predicted V_0, correlations for density of flibe and flinak were determined and com-

pared with the experimental correlations for density as shown in Fig. 6.3(b) and (d), respectively. The linear fit of the density versus temperature in Fig. 6.3(b) suggests a correlation for density of pure flibe from FPMD simulations for the temperature range from 823 K to 1423 K of

$$\rho \ \ [\mathrm{kg/m3}] = 2374 - 0.3967 \cdot T[\mathrm{K}] \tag{6.5}$$

where ρ is the density, and T the temperature in Kelvin. The correlation for density of pure flinak from the FPMD simulations for the temperature range from 973 K to 1423 K is

$$\rho \ \ [\mathrm{kg/m3}] = 2477 - 0.4895 \cdot T[\mathrm{K}] \tag{6.6}$$

As shown in Fig. 6.3(b) and (d), calculated densities of flibe and flinak from the FPMD simulations at 973K are in good agreement with the experiments. However, at higher temperature at 1423K, calculated densities seem to be slightly overestimated, because of the smaller density decrease as the temperature increases compared to the experiments. Detail discussion on the slope of density vs. temperature is addressed in following section.

From the third-order Birch-Murnaghan fit of pressure-volume data, bulk moduli as a function of temperature also can be predicted. Fig. 6.4 shows the trend of bulk modulus as a function of temperature. A decrease of bulk modulus with increasing temperature, which is the typical trend of bulk modulus for solid salt, is observed [113]. Although experimental data for pure flibe does not exist, the bulk modulus of a $LiF^{-}BeF_2$-ThF_4-UF_4 mixture, which was estimated from the experimental compressibility-temperature correlation, is used for comparison instead [114]. Predicted bulk modulus from the FPMD modeling is within the experimental error range of the $LiF^{-}BeF_2$-ThF_4-UF_4 mixture.

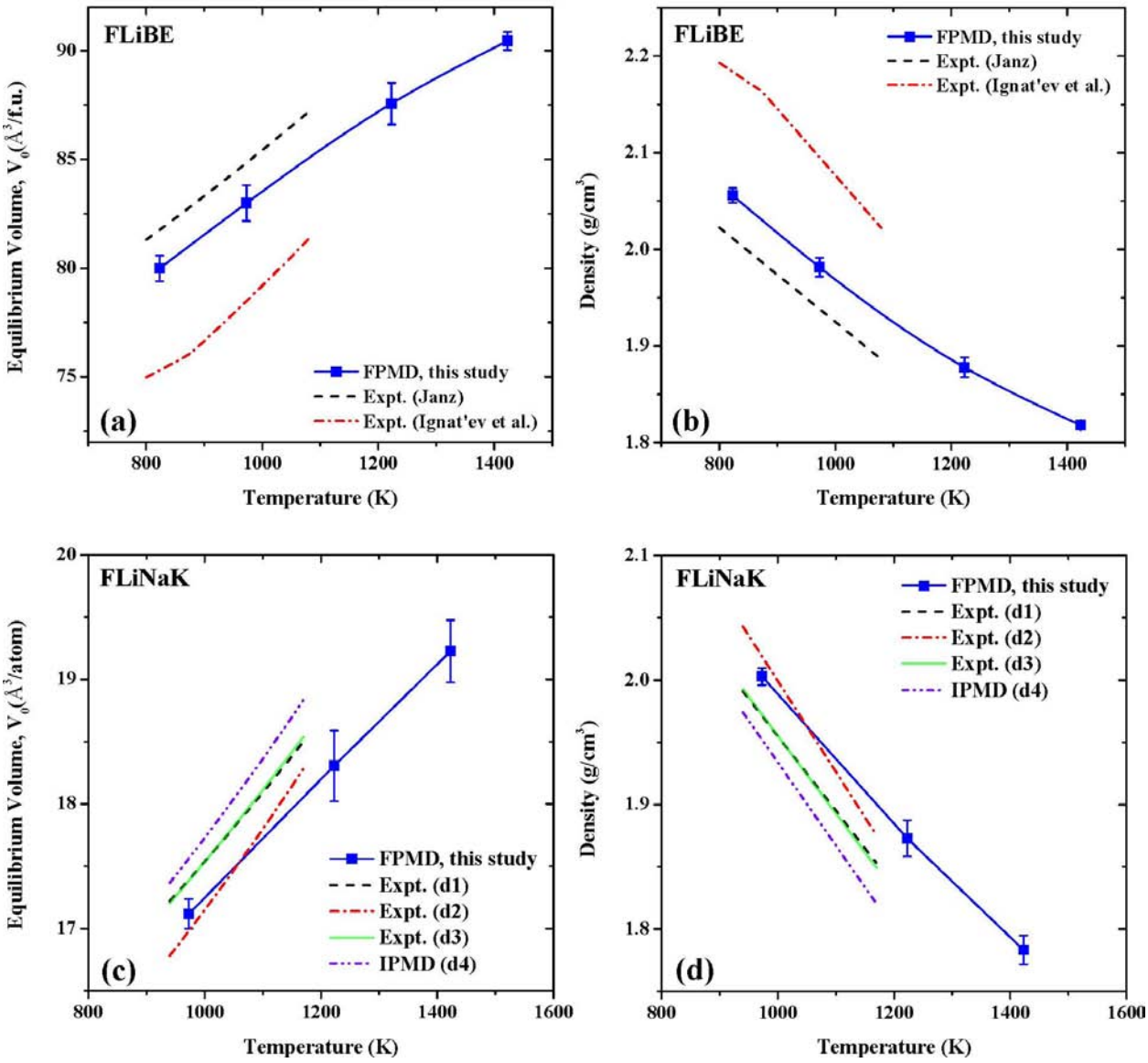

Figure 6.3: Comparisons of the estimated equilibrium volume for (a) flibe and (c) flinak from the FPMD simulations with the experimental data and converted correlations for density for (b) flibe and (d) flinak. Experimental correlations for density of Janz and Ignat'ev et al. for flibe, and Grele IPMD density model for flinak (d4) was added for comparison [70]. Error bars represent two sigma standard error of the mean.

Coefficient of Thermal Expansion

The calculated CTE of flibe at 973 K from the FPMD simulations is 2.00 ± 0.14 $\times 10^{-4}$ (1/K). Experimental CTE values, which are calculated from the experimental correlations for density of

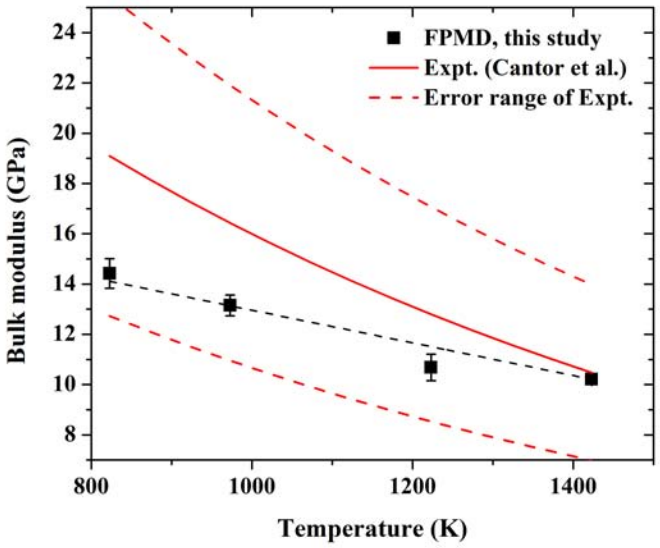

Figure 6.4: Predicted bulk moduli (B) of flibe with errors at multiple temperatures. Bulk moduli were obtained from EOS fits as described in the Methods Section. Experimental bulk moduli were estimated from the compressibility-temperature correlation for $LiF^{-}BeF_2$-ThF_4-UF_4 mixture [114]. Error bars represent one sigma standard error of the mean.

Janz and Ignat'ev et al., are 2.52 $\times 10^{-4}$ (1/K) and 3.28 $\times 10^{-4}$ (1/K), respectively [100, 101]. The calculated CTE of flinak at 973 K from the FPMD is 2.45 $\pm$ 0.10 $\times 10^{-4}$ (1/K). Experimental CTE values of flinak, which are calculated from the correlations for density from previous references within Sohal et al., are summarized in Table 6.1 [103]. In general, the CTE values from the FPMD simulations are slightly smaller than that from the experiments. The source of this discrepancy is not clear but a smaller value of CTE compared to experiment when applying FPMD has also observed by Woodward et al. for different liquid system[79].

6.3.3 Kinetic Properties of Pure Fluoride Salts

SelfF^{-}diffusion coefficients of Li^{+}, Be^{2+} and F^{-} ions in flibe and Li^{+}, Na^{+}, K^{+} and F^{-} ions in flinak were analyzed from the FPMD simulations. The estimated self-diffusion coefficient of Li^{+}, Be^{2+} and F^{-} ions in flibe are shown in Fig. 6.5. This figure shows the temperature dependence as

Table 6.1: Estimated coefficient of thermal expansion (CTE) of flibe and flinak at 973 K from FPMD simulations and comparison with the CTEs from literature.

	FPMD, this study ($1/K \times 10^{-4}$)	From literature ($1/K \times 10^{-4}$)	References
CTE of flibe	2.00 ± 0.14	2.52	Janz [100]
		3.28	Ignatev et al. [101]
CTE of flinak	2.45 ± 0.10	3.04	(d1) [108, 109]
		3.62	(d2) [107, 110, 111]
		3.16	(d3) [112]
		3.43	(d4) [70]

described by the Arrhenius equation. Diffusivity of Li+ and F^- in flibe were measured experimentally in a relatively low temperature range by Iwamoto et al. and Ohmichi et al. [115, 116]. The Arrhenius equations for Li^+ and F^- diffusion are taken from the above references and plotted in the same figure for comparison. Due to the lack of experimental data of diffusivity in flibe, diffusivity of Li and F ions in flinak is added for comparison and discussion (Umesaki et al.) [117]. The estimated self-diffusion coefficients for constituent ions of fluoride salts at multiple temperatures are summarized in Table 6.2.

In case of the Li^+ diffusion in flibe, the calculated diffusion coefficients are lower than the experimental value from Iwamoto et al. [115]. However, it should be noted that experimental diffusion coefficient of Li and F in flibe has an error range due to the spread of measured values and the FPMD results for Li diffusion in this study are close to the lower bound of the experimental Li diffusion in flibe [115, 116]. Although the measured diffusivity of Li in flibe and flinak differs in magnitude, the activation energies (slope of the Arrhenius plot) for the diffusion of Li in both flibe (solid line) and flinak (dashed line) are almost identical, and the activation energy from our

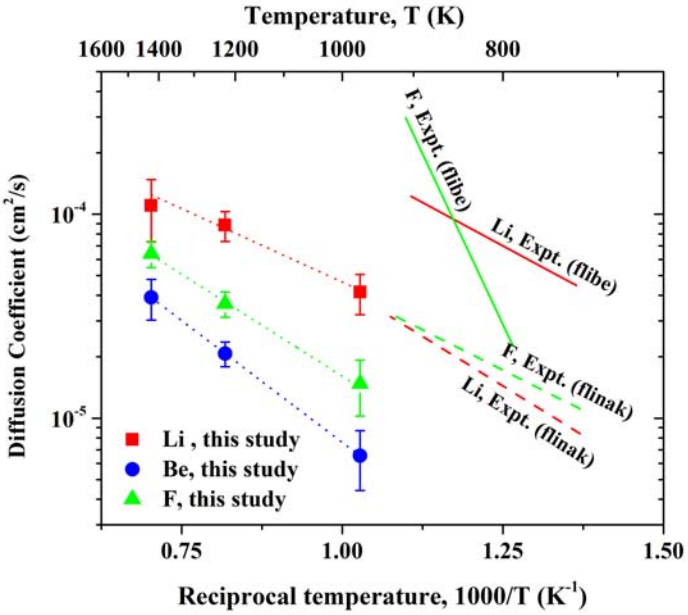

Figure 6.5: Temperature dependence of self-diffusion coefficients of Li+, Be2+ and F- in flibe with error bar. Data points were obtained from the FPMD calculations at the temperatures of 973, 1223, and 1423K. Experimental diffusivity for Li and F are shown together for comparison [115, 116, 117]. Error bars represent one sigma standard error of the mean.

Table 6.2: Estimated self-diffusion coefficients for constituent ions of flibe and flinak salt at multiple temperatures from the FPMD simulations. Error bars represent one sigma standard error of the mean.

Salt	Ions	Self-Diffusion Coefficient ($cm^2/s \times 10^{-5}$) 973 K	1223 K	1423 K
Flibe	Li^+	4.14 ± 0.92	8.84 ± 1.48	11.1 ± 3.74
	Be^{2+}	0.65 ± 0.21	2.07 ± 0.29	3.91 ± 0.88
	F^-	1.48 ± 0.45	3.64 ± 0.52	6.41 ± 0.93
Flinak	Li^+	2.82 ± 0.19	7.47 ± 0.39	9.17 ± 0.46
	Na^+	2.89 ± 0.64	7.76 ± 0.82	8.87 ± 0.89
	K^+	3.20 ± 0.26	7.78 ± 0.64	9.18 ± 0.57
	F^-	3.07 ± 0.21	7.77 ± 0.42	9.83 ± 0.31

study for Li diffusion is also very similar. Overall, this comparison suggests that our Li diffusion results are in good agreement with flibe and trends from flibe and flinak.

Unlike the Li case, the measured F^- diffusion in flibe shows much larger activation energy compared to that of F^- diffusion in flinak and the FPMD value of F^- diffusion in flibe. Ohmichi et al. suggested either the exchange of fluorine atoms between neighboring beryllate anions diffusion by means of a neutral ion pair (LiF) as a possible mechanism of F^- diffusion in flibe to explain the large value of the fluorine diffusion coefficient [116]. However, the apparently extraordinarily high measured diffusivity of F ions in flibe has not yet been clearly explained. Because another measurement of F diffusion in flibe has not been made, it is difficult to conclude if the experiments might have an error. However, given the success of the FPMD for Li^+ in flibe, there is no reason to expect a significant error form the FPMD for F^- diffusion. Furthermore, the values for F^- diffusivities from FPMD are similar in both magnitude and activation energy to those in flinak (shown in Fig. 6.5) and NaF-AlF_3 (not shown) [118]. These results, taken together, suggest that the values for F^- seen by Ohmichi, et al. may contain errors and should be reevaluated [116].

Klix et al. used the Car-Parrinello MD to study the tritium diffusion in molten flibe and calculated the diffusion coefficients of lithium and fluorine [81]. The magnitude of the diffusion coefficients and the activation energies (slope of the data points) are consistent with the values from this study.

Diffusivities of Li^+, Na^+, K^+, and F^- ions in flinak were also determined in this work by FPMD, as shown in Fig. 6.6. The experimental diffusivities of constituent ions in flinak from Umesaki et al. are plotted in Fig. 6.6 for comparison [117]. The values of activation energy for each ion are difficult to compare quantitatively to those obtained from experiments due to the relatively large error bars of each data point. In particular, since only six atoms of Na exist in the 100-atom cell for flinak, the error on the diffusivity of the Na ion is understandably greater than the others. However, estimated diffusivities of Li^+, Na^+, K^+, and F^- in flinak from FPMD simulations are in general agreement with those from the experimental results, especially at lower temperatures (note that the

y-axis range in Fig. 6.6 is only about one order of magnitude).

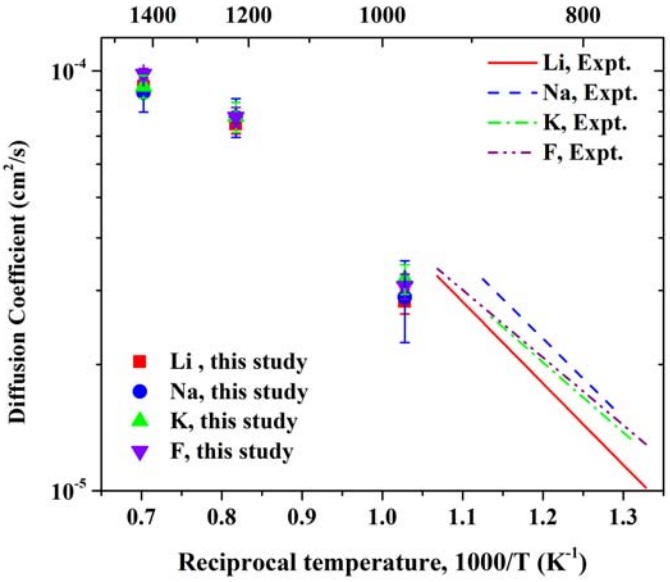

Figure 6.6: Temperature dependence of self-diffusion coefficient of Li^+, Na^+, K^+ and F^- ions in flinak with error bar. Data points were obtained from the FPMD calculations at the temperatures of 973 K, 1223 K, and 1423 K. The experimental values are added for comparison [117]. Error bars represent one sigma standard error of the mean.

As shown in Table 6.2, estimated diffusion coefficients of constituent ions of flinak (Li^+, Na^+, K^+, and F^-) were similar to each other within the error bars. In contrast, the diffusivities of Li^+ and F^- in flibe, which are common elements in both salts, show quite a significant difference between each other, with Li^+ being the fastest ion. It is possible that in flibe Be^{2+}, which has a higher valence state than any cations in flinak, interacts with the F^- and effectively forms a fluoro-beryllate anion (BeF_4^{2-}) which consequently slows the diffusion of the fluorine in flibe.

6.4 FPMD Modeling of Solutes in Fluoride Salts

The first principles molecular dynamics (FPMD) modeling of solute Cr, Fe and Zr impurities in fluoride salts at 973K (700°C) was conducted. The Cr and Fe are chosen because these elements are major constituents of the supporting steel structures. The Zr (ZrF4), on the other hand, was

investigated as a salt constituent to be mixed into the salt because it stabilize the acidic component (ZrF_6^{2-}) and decrease in the chemical activity [119]. FPMD simulations for solute containing systems were conducted with relatively smaller system sizes than the pure salts (63 atoms for flibe (18 Li, 9 Be, and 36 F atoms) and 52 atoms for flinak (12 Li, 3 Na, 11 K, and 26 F atoms)) in order to enable longer simulations.

6.4.1 Diffusion of Solute Ions in Fluoride Salts

It is well known that chromium has two dominant oxidation states when it is dissolved in the salt. In cases when the Cr is dissolved in flibe, Cr(II) is the predominant oxidation state, but when the Cr is dissolved in flinak, Cr(III) is more stable [119]. Therefore, we considered both oxidation states of solute Cr in the salt. To assess the effect of different oxidation states of Cr solute, we introduced Cr, CrF_2 and CrF_3 into the salt to yield Cr^0, Cr^{2+} and Cr^{3+} solutes, respectively, within the salt. Similarly, Fe, FeF_2, FeF_3, Zr, and ZrF_4 were introduced into the salt to yield Fe^0, Fe^{2+}, Fe^{3+}, Zr^0 and Zr^{4+} solutes, respectively,

To obtain reliable statistical averages of the self-diffusion coefficient of the solute ion in the salt, nine independent FPMD simulations for 8ps were performed for each solute system. Then, the slopes of nine independent MSDs for each ion were averaged to determine the diffusion coefficient of solute ion. The error in the solute diffusivity was obtained by evaluating the standard error of the mean from these nine independent simulations. As shown in Fig. 6.7, FPMD is sensitive to the role of charge state of solute ions in flibe. The neutral atom moves faster than the charged solute ion, which interact more with the surrounding F^- ions, except the solute Li case. It seems that diffusivities of Li^0 and Li^+ ion are similar due to the fact that Li^+ ion has a weaker bonding with surrounding F- ions. In flibe both the Fe^{3+} and Cr^{3+}, which exhibits a stronger bonding with surrounding F^- ions, shows a smaller diffusion coefficient than that of the Fe^{2+} and Cr^{2+} ion, respectively, as expected. However, this trend is not clear in flinak, where the diffusion of Cr^{2+} and

Cr^{3+} are not distinguishable within the error bars of our present calculation. The reason that the expected trend of lower diffusivity with higher valence is found with Cr in flibe but not in flinak is not clear at this time.

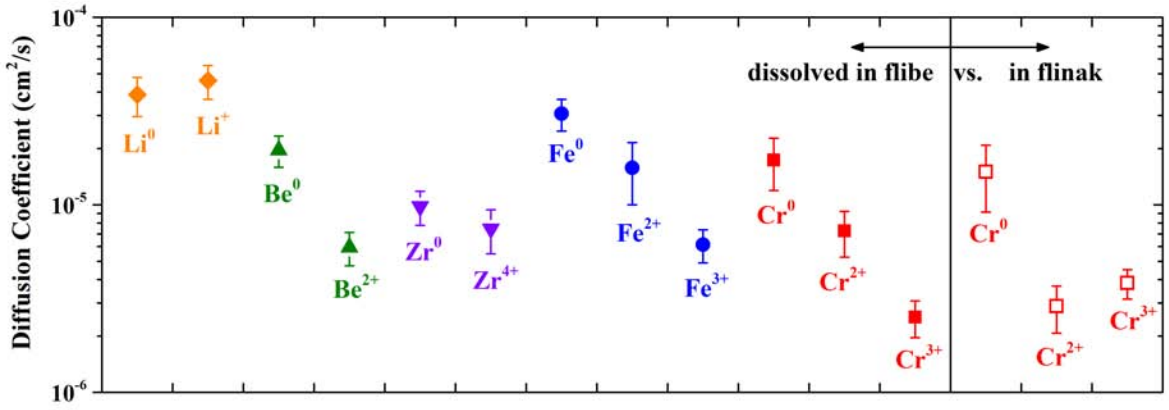

Figure 6.7: Self-diffusion coefficients of solute Li, Be, Zr, Fe, and Cr ions in flibe and flinak at 973 K. Error bars represent one sigma standard error of the mean.

Table 6.3: Estimated self-diffusion coefficients for solute ions in flibe and flinak at 973 K from the FPMD simulations.

Salt	Ions	Self-Diffusion Coefficient ($cm^2/s \times 10^{-5}$)
Flibe	Li0	3.87 ± 0.91
	Li^+	4.60 ± 0.94
	Be^0	1.96 ± 0.37
	Be^{2+}	0.59 ± 0.12
	Zr^0	0.98 ± 0.20
	Zr^{4+}	0.75 ± 0.20
	Fe^0	3.07 ± 0.59
	Fe^{2+}	1.58 ± 0.58
	Fe^{3+}	0.61 ± 0.12
	Cr^0	1.73 ± 0.54
	Cr^{2+}	0.73 ± 0.20
	Cr^{3+}	0.25 ± 0.06
Flinak	Cr0	1.50 ± 0.58
	Cr^{2+}	0.29 ± 0.08
	Cr^{3+}	0.38 ± 0.07

The self-diffusion coefficient of Fe^{2+} (5×10^{-6} cm^2/s) in flibe at 773 K was measured and provided in the reference [118]. Although it is hard to compare this measurement directly with the calculated diffusivity of Fe^{2+} (1.58×10^{-5}) in flibe at 973 K from FPMD, due to the change in temperature between the modeling and the experiments. However, the effect of the temperature on the diffusion can be studied by comparing the values. If we assume that both measured and calculated Fe^{2+} diffusivities are accurate, the activation energy of Fe^{2+} ion in flibe is about 36.4×10^3 J/mol-K. This values is comparable with the calculated activation energies for the diffusion of Li, Be and F ion in pure flibe in this work (31.9, 43.3 and 34.1 J/mol-K, respectively). Unfortunately, there is no experimental or computational data to compare with for other solute ions.

6.4.2 Structure Surrounding Solutes in Fluoride Salts

Structure Surrounding Dissolved Cr

Fig. 6.8 shows the radial distribution function (RDF) of flibe with Cr (solid lines), CrF_2 (dash-dot lines) and CrF_3 (short-dash lines), and calculated first-peak distances and first-shell coordination numbers for Cr^0, Cr^{2+} and Cr^{3+} in flibe and flinak are shown in Table 6.4. RDF curves between Be-F and Li-F are similar for all Cr valence states and the RDF between Be and Be (green lines) are affected only slightly by changing Cr valence. However, the Cr-F RDFs (orange lines) vary considerably due to the change in the valence state of Cr in the molten salts. When comparing the Cr^0-F, Cr^{2+}-F, and Cr^{3+}-F RDFs it is seen that the first peak increases and occurs at a small radius with increasing Cr charge. This trend indicates that the Cr ion has stronger bond with F ion when the Cr has a higher oxidation state, as expected. This trend is also supported by evaluating the first-shell coordination number of Cr with the surrounding F anion which can be estimated by integrating the radial distribution function (gray lines in Fig. 6.8) from zero to the first minimum. Similar trends to those observed here are also found in flinak.

The local structure of Cr solute in flibe salt was studied by analyzing the first-principles molec-

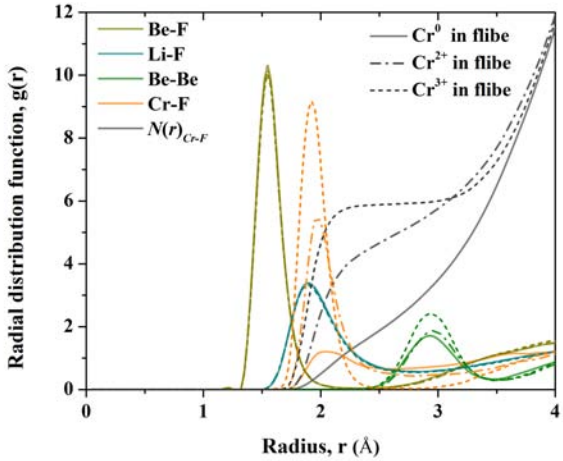

Figure 6.8: Radial distribution functions (RDF) of flibe with Cr, CrF_2 and CrF_3. Solid lines denote the RDFs when Cr^0 is introduced into flibe. Dash-dot lines and short-dash lines denotes when CrF_2 and CrF_3 is introduced into flibe, respectively. Neighbor function, $N(r)$, between $Cr^0/Cr^{2+}/Cr^{3+}$ and F^- (gray lines) are shown together.

ular dynamics simulation trajectory. The VMD program was used to visualize the trajectory of FPMD simulation. Fig. 6.9 shows snapshots of FPMD trajectory of flibe system with the dissolved Cr solute [120]. Both Fig. 6.9(a) and Fig. 6.9(b) were captured from the FPMD trajectory of flibe with Cr^{2+} system. For the Cr^{2+} ion one can observe various coordination polyhedral, such as a distorted square-planar (Fig. 6.9(a)) and octahedral (Fig. 6.9(b)) first-neighbor F^- shell. However, the Cr^{3+} ion in flibe makes a more stable octahedral Cr and F bonding structure, as can be seen in Fig. 6.9(c). This trend is also supported qualitatively by the slope of the $N(r)$ curves in Fig. 6.8, where the stable first-neighbor F- shell for Cr^{3+} leads to an $N(r)$ with a clear plateau while the less stable F^- shell for Cr^{2+} leads to an to an $N(r)$ that never levels out. The first neighbor shell can be evaluated quantitatively by the coordination number between Cr and F in Table 6.4, which shows the value of 5.9 for Cr^{3+}, a value within the simulation uncertainties of the perfect octahedral coordination value of 6. The stability of more octahedrally coordinated Cr when in 3+ vs. 2+ state is consistent with its smaller size and larger valence, which is likely to attract F^- more strongly. The same analysis as performed for flibe was performed for the Cr^{2+} and Cr^{3+} in flinak

and it shows a similar trend as for flibe.

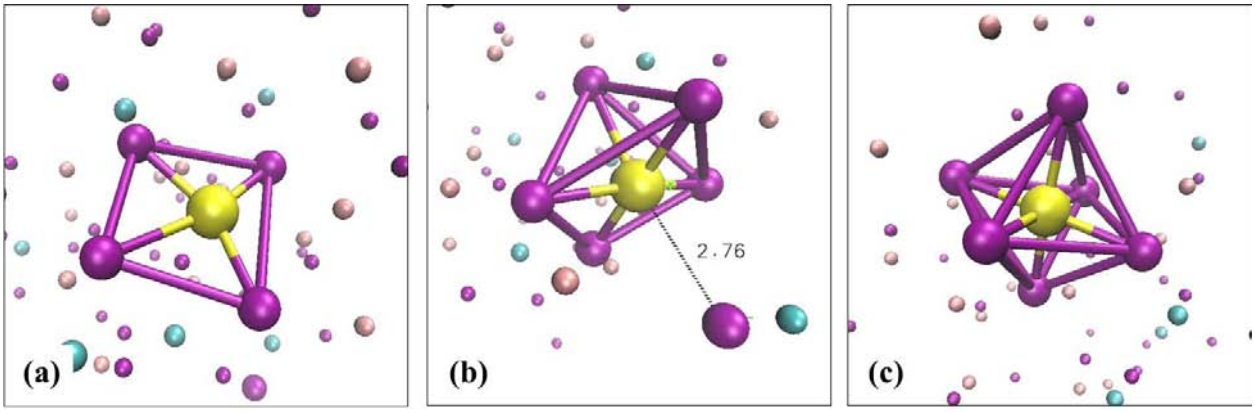

Figure 6.9: Snapshots of FPMD trajectory for flibe with the solute Cr. Yellow ball is chromium ion and purple balls are fluorine ions. Pink balls and cyan balls are Li and Be, respectively. (a) FPMD snapshot of flibe with CrF_2 showing flat bonding between Cr and F; (b) FPMD snapshot of flibe with CrF_2 showing unstable octahedral structure of Cr and F; (c) FPMD snapshot of flibe with CrF_3 showing stable octahedral structure of Cr and F.

Table 6.4: First-peak radius and first-shell coordination numbers for solute ions and F^- pairs in flibe and flinak. First shell coordination numbers are determined by the integral of the RDF up to its first minimum.

Salt	Ion Pair	First-Peak Radius (Å)	Coordination Number
Flibe	Zr^0 F^-	2.23	4.8
	Zr^{4+} F^-	2.07	7.1
	Fe^0 F^-	2.05	2.1
	Fe^{2+} F^-	1.97	5.2
	Fe^{3+} F^-	1.94	5.9
	Cr^0 F^-	2.05	2.1
	Cr^{2+} F^-	1.97	5.2
	Cr^{3+} F^-	1.93	5.9
Flinak	Cr^0 F^-	1.97	2.7
	Cr^{2+} F^-	1.96	4.9
	Cr^{3+} F^-	1.94	5.9

The spin state of the Cr^{2+} and Cr^{3+} ions in molten salts were monitored during the FPMD simulations. Cr^{2+} and Cr^{3+} are d^4 and d^3 ions, with 4 and 3 d-orbital valence electrons, respectively. In fluoride salts, solute Cr^{2+} and Cr^{3+} have magnetic moments of four and three, respectively, which

are the expected moments for their high spin states.

Structure Surrounding Dissolved Fe and Zr

Local structure of Fe and Zr ions in flibe salt were also studies by analyzing the FPMD simulation trajectory. Fig. 6.10 shows radial distribution functions (RDF) of flibe with Fe/FeF_2/FeF_3 and Zr/ZrF_4. Solid lines denote the RDFs between solute ion and surrounding F- ions, while dash lines are neighbor function, N(r). The first neighbor shell was evaluated quantitatively by the coordination number between ions and F and summarized in Table 6.4. Comparing the first-peak radii and coordination numbers for $Fe^{0/2+/3+}$-F^- with the values for $Cr^{0/2+/3+}$ -F^-, it is seen that behavior of Fe ions in flibe is similar with Cr ions in flibe. In case of the Zr, it exhibits a stronger bond with the F^- ions and hence larger coordination number. Zr shows various local structures having 6 – 8 bonds with surrounding F^- ions, with an average coordination number of ~7 F^- in its first neighbor shell.

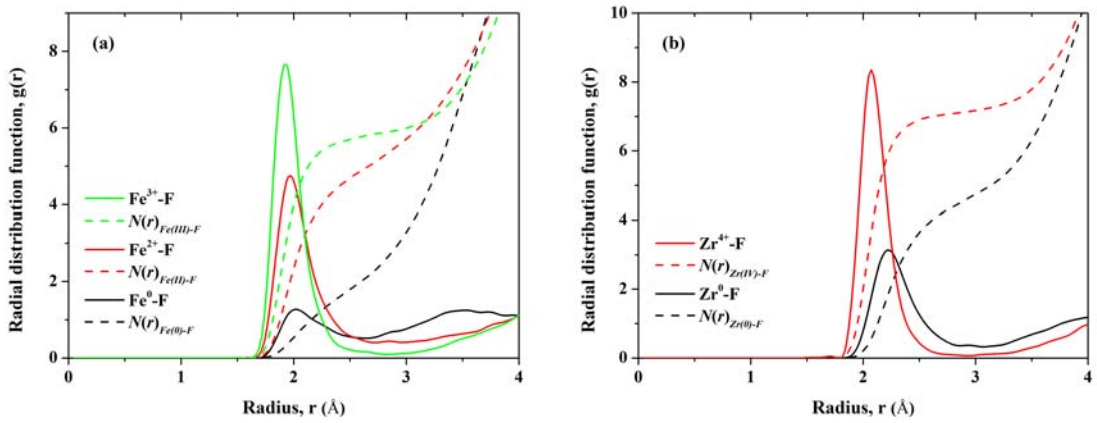

Figure 6.10: Radial distribution functions (RDF) of (a) flibe with Fe (black lines), FeF_2 (red) and FeF_3 (green) and (b) flibe with Zr (black), ZrF_4 (red). Solid lines denote the RDFs between solute ion and surrounding F^- ions, while dash lines are neighbor function, $N(r)$.

6.4.3 Standard Redox Potential for Solutes in Molten Flibe Salt

Corrosion behavior of structural materials in fluoride salt is governed mainly by fluorine potential [121]. Stability of fluoride and oxide compound of structural constituents in salt is also affected by electrochemical corrosion potential of the system (i.e. fluorine potential). The standard redox potential of various redox couples (Li(I)/Li(0), Be(II)/Be(0), Zr(IV)/Zr(0), Fe(III)/Fe(II), Fe(II)/Fe(0), Cr(III)/Cr(II), and Cr(II)/Cr(0)) in flibe at 973K (700 C), which is an operating temperature of fluoride-salts-cooling reactor systems, has been calculated from FPMD modeling of solute systems.

We formulate the equation to calculate the redox potential from FPMD based on the redox reaction. For example, corresponding chemical reactions for the redox couple of Cr(III)/Cr(II) is shown below;

$$2CrF_3(d) = 2CrF_2(d) + F_2(g) \tag{6.7}$$

Based on the above reactions, we estimate the redox potential for Cr(III)/Cr(II) using Eq.6.8,

$$\langle V_{redox} \rangle_{\ CrF_3/CrF_2}(vs.\ F_2/F-) = -\frac{[\langle E(CrF_3 + MS)\rangle - \langle E(CrF_2 + MS)\rangle - 0.5 \cdot G(F_2)] + C^S}{1 \cdot e} \tag{6.8}$$

where <*E*> is the ensemble average of total energy as calculated from FPMD, *e* the absolute value of the electron charge, $G(F_2)$ the free energy of a fluorine gas, and C^S the entropy correction term [122, 123, 124]. C^S is shown in Eq. 6.9,

$$C^S = -(T \cdot S_{CrF_3 pure} - T \cdot S_{CrF_2 pure})/F \tag{6.9}$$

where T is the temperature and F the Faraday constant. This term is the entropy term for the dissolved fluorides because the energy from the FPMD does not include the entropic contributions in it.

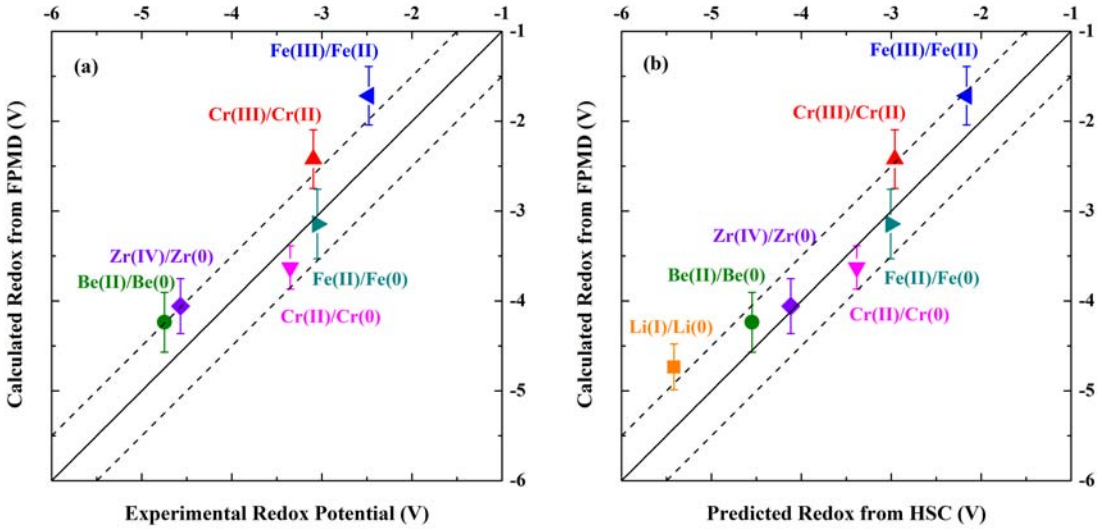

Figure 6.11: (a) Comparison of calculated redox potential of several redox couples in molten flibe salt at 973 K by FPMD (y-axis) with the (a) experimental redox potential and the (b) predicted redox potential from the thermodynamic database for pure solid form of fluorides [124]. Dashed lines are showing ± 0.5 V range from the guide line. The error bars represent the two sigma standard error of the mean.

Fig. 6.11 shows the comparison of calculated redox potential of several redox couples in molten flibe salt at 973 K by FPMD with the (a) experimentally measured redox potential (vs. F_2/F^- reference) and the (b) predicted redox potential from the thermodynamic database for pure solid form of fluorides [124]. Table 6.5 summarizes the calculated values of redox potential for those couples in molten flibe salt at 973K from FPMD simulations with the predicted redox from HSC Chemistry and Experimentally measured redox data [125]. However, it should be noted that experimentally measured redox potentials needed some processing to be comparable to the FPMD results. Specifically, the processed experimental data shown in Fig. 6.11 and Table 6.5 was calculated from a Ni(II)/Ni(0) reference, which was measured in molten LiF-BeF_2-ZrF_4 (65.6-29.4-5.0 mol%) at 773 K, by converting the values to a F_2/F^- reference and compensating temperature effects theoretically. In order to convert to our temperatures and the F_2/F^- reference it was necessary to make a few assumptions. The first assumption which was made is that the effect of 5mol% of ZrF_4 in standard redox potentials in flibe is negligible. The second is that the *emf* (electromotive force) of

Ni(II)/Ni(0) (vs. F_2/F^-) at 773K is -2.778 V, which was calculated from the HSC Chemistry for the reduction reaction of NiF_2 (i.e. NiF_2 = Ni +F_2(g)). The last assumption was that the temperature effect on redox potentials can be estimated thermodynamically from the solid fluoride reactions.

Table 6.5: Calculated redox potential (vs. F_2/F^- reference) of several redox couples in molten flibe salt at 973K with the predicted redox potential from the thermodynamic database [124].

Redox Couples	Prediction from HSC [124] (V)	FPMD (This Study) (V)	FPMD 2 Std. Error (V)	Experimental Redox 1 [125] (V)
Li(I)/Li(0)	-5.417	-4.734	0.254	
Be(II)/Be(0)	-4.549	-4.236	0.332	-4.749
Zr(IV)/Zr(0)	-4.119	-4.058	0.306	-4.57
Cr(III)/Cr(II)	-2.961	-2.421	0.326	-3.352
Cr(II)/Cr(0)	-3.385	-3.627	0.24	-3.095
Fe(III)/Fe(II)	-2.07	-1.716	0.325	-3.051
Fe(II)/Fe(0)	-3.054	-3.144	0.387	-2.479

[1]

As the predicted redox potential is obtained from the fluorination of pure solid phase substance, the values can be different with the actual measurements of redox reaction in the molten salt. However, these predicted redox values are useful for comparison because they are generally quite close to the potentials measured in the salt.

Although calculated redox potential for solutes are not perfectly matched with the measurements and the prediction, most of the calculated redox potentials are within the range of ±0.5V from the experimental data. Various reasons can be proposed to explain the difference between the calculation and references (measurements or prediction), including DFT errors, statistical issues in FPMD, and several approximations that we have made in the approach to keep the study practical. More specifically, in this work, we took energy from the FPMD simulations instead of enthalpy in the redox formulation (this is equivalent to assuming P=0). And it was assumed that the entropy

[1]Experimentally measured redox potentials were calculated from reference [125], which were measured in molten LiF-BeF_2-ZrF_4 (65.6-29.4-5.0 mol%) at 773K using Ni(II)/Ni(0) reference, by converting the values to a F_2/F- reference and compensating temperature effect theoretically.

difference between solutes (X) in flibe and fluorides (XF_n) in flibe is same with the difference of entropy between solid phase X and solid phase XF_n. We believe that further refinement is possible with exploration of additional first-principles exchange-correlation functionals as well as more extensive simulation employing larger simulation cells, longer simulations, more sampling of simulation runs, and running simulation at the most accurate equilibrium volume for solute systems.

6.5 Conclusions

First-principles molecular dynamics (FPMD) modeling was employed to predict thermo-kinetic properties of two types of molten fluoride salts, flibe and flinak, and to assess solute (Cr, Fe, Zr, Li and Be) behavior within the salts. The GGA/PBE exchange-correlation-functional (xc-functional) was used in the FPMD modeling, taking into account the van der Waals (vdW) dispersion interaction. The selection of the exchange-correlation functional and the method for the vdW dispersion was found to have a large influence on the equilibrium properties of the molten salt system.

The thermo-kinetic properties of pure fluoride salts such as the equilibrium volume, density, bulk modulus, coefficient of thermal expansion, and self-diffusion coefficient were predicted and compared to the experimental data or computational data. The predicted thermo-kinetic properties were generally in good agreement with the previous experimental literature, supporting the validity of FPMD simulation in modeling the fluoride salts at high temperatures. The FPMD was also used to generate data to validate the experimental data in cases where the data had a large scatter (e.g., different correlations for density vs. temperature, and F^- diffusion in flibe and flinak) and where no experimental measurements were available (e.g., bulk modulus, Be^{2+} diffusion in flibe, and Cr ions diffusion in flibe and flinak).

The FPMD modeling is well suited to studying impurities, as no potential fitting is needed to include them in the model. The self-diffusion coefficients for solute ions were shown to be dependent on the oxidation state of the dissolved solute ions, with higher valence solute ions generally

move slower. Further structural analysis on the Fe and Cr ions showed that 3+ ion was generally surrounded by ~6 F^- ions in a nearest-neighbor octahedral-like cage, while 2+ ion is located in various local structures including distorted square planar and octahedral type environments, with an average coordination number of ~5 F^- in its first neighbor shell. A formulation for predicting standard redox potentials (vs. F_2/F^- reference) for solvent and solute species was developed and used to predict a number of redox values for flibe. Agreement with experimental data was generally within 0.5 V and the source of error is likely a compound effect of having to process the experimental data for comparison, DFT inaccuracies, and simulation limitations.

In this project, we demonstrated the FPMD can be used as a versatile tool to model fluoride molten salts and to study the behavior of dissolved solutes with varying valence states. Overall, by using FPMD, we have been able to provide new insights into the thermo-kinetic properties of flibe and flinak fluoride salts and solute ions in these salts.

Chapter 7

Systems Engineering for Salt Systems

7.1 Introduction to PB-FHR Constraints

The design and appropriate location of a chemistry control system for the Pebble Bed Fluoride High Temperature Salt Cooled Reactor (PB-FHR) depends on surface areas of the various materials in the primary coolant loop, and the coolant temperatures that these materials are exposed to. Key parameters to increase the lifetime of the PB-FHR core components are temperatures of the coolant that graphite blocks are exposed to in the core for durability of graphite reflectors and fuel temperature distribution for fuel performance and durability of the fuel elements. Temperatures of the coolant in contact with metallic structures is also key for durability of these structures (essentially heat exchangers in the current baseline design). The University of California - Berkeley (UCB) has developed models and design elements to address related issues, as described here.

7.2 Experiment Design Parameters

The 900 MW_{th} PB-FHR has been used as the primary reference to establish temperatures and other parameters for the cleaning, passivation, and corrosion experiments performed under this project. Subsequent work is now also generated similar information for the new 236 MW_{th} Mk1 PB-FHR design being developed under a new NEUP Integrated Research Project. For the primary loop, experiments matched ratios of surface areas of different materials, including graphite, which has been observed to play a potential role in fluoride salt corrosion, as well as a potentially important sink for removal of tritium. Figure 7.1 shows the geometry of the 900 MW_{th} PB-FHR annular core and Table 7.1 is a summary of graphite and metal surface areas in the core. The surface of the fuel and blanket pebbles is graphite, therefore a critical parameter is the total surface area of pebbles in

the core, which greatly exceeds the surface area of the graphite reflector blocks, as seen in Table 7.1.

Table 7.1: Graphite and Metal Surface Areas in the 900 MW_{th} PB-FHR Annular Core.

Parameter	Value
Inner graphite reflector surface area	47.2 m^2
Outer graphite reflector surface area (core side)	100.1 ^{2}
Outer graphite reflector surface area (downcomer side)	157.2 ^{2}
Reactor vessel surface area	189.2 ^{2}
Pebbles surface area	10,286.8 ^{2}

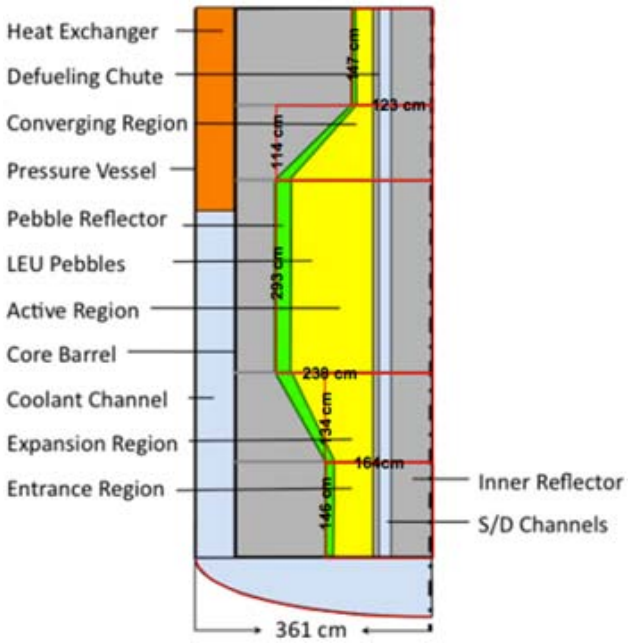

Figure 7.1: Geometry of the 900 MW_{th} PB-FHR Annular Core.

UCB has developed thermal hydraulic models for the PB-FHR using the COMSOL Multi-physics code. The detailed design of the PB-FHR core can be used to estimate FHR-relevant operating condition parameters for corrosion and degradation analysis. Power distribution in the core, for steady-state operation, was obtained using MCNP5. Figure 7.2, Figure 7.3 and Figure 7.4 present the bulk coolant temperature, fuel temperature and pressure distributions in the 900 MW_{th} PB-FHR core, respectively.

As shown in Figure 7.2, the minimum coolant temperature is 600 °C, and the bulk coolant temperature reaches 769 °C in some regions of the core. However, the average core outlet temperature is 700 °C, and designing the outlet plenum structures for proper mixing will ensure that the coolant reaching the inlet of the heat exchangers out of the reactor vessel is well mixed, at the bulk temperature. The average coolant temperature in the core is 652 °C, slightly higher than the average of the core inlet and outlet temperatures, because of bypass flow around the core.

As a result of a high heat transfer coefficient between the graphite shell of the pebbles and the salt coolant (h$\sim$ 15kWm^{-2}K on average in the core), the temperatures of the pebble surfaces never exceed those of the surrounding coolant by more than a few tens of degrees Celsius.

The average fuel temperature in the PB-FHR core under normal operating conditions is 714 °C, with a minimum value of 600 °C and a maximum value of 1110 °C in a very small region of the core. These results will partly inform fuel performance and potential material degradation of the pebble fuel. Pressure drop across the PB-FHR core is only 52 kPa. This pressure distribution can be used for fatigue analysis of the core components.

The primary coolant temperature distribution at the interface with the core graphite blocks is detailed in Figure 7.5.

Another key element of this work was to develop and validate a design for a coiled tube air heater (CTAH), to provide a method to predict the heater surface area since this is the largest surface area of metal in the primary system. The baseline PB-FHR design has two CTAHs, which transfer heat from the primary salt coolant to compressed air from the gas turbine system. The CTAHs use an annular tube bundle formed by coiled tubes, with air flowing radially outward over the tubes. Figure 7.6 shows a schematic elevation cut-away view of a CTAH, and Figure 7.7 presents a plan view. The CTAHs surface area is the largest area of metal in the system, and thus is the most important to study for stress and corrosion purposes. UCB has constructed a test bundle to validate models for the surface area of these novel heat exchanger designs. CTAH experiments will perform room temperature heat transfer from warm water to air, using prototypical geometry

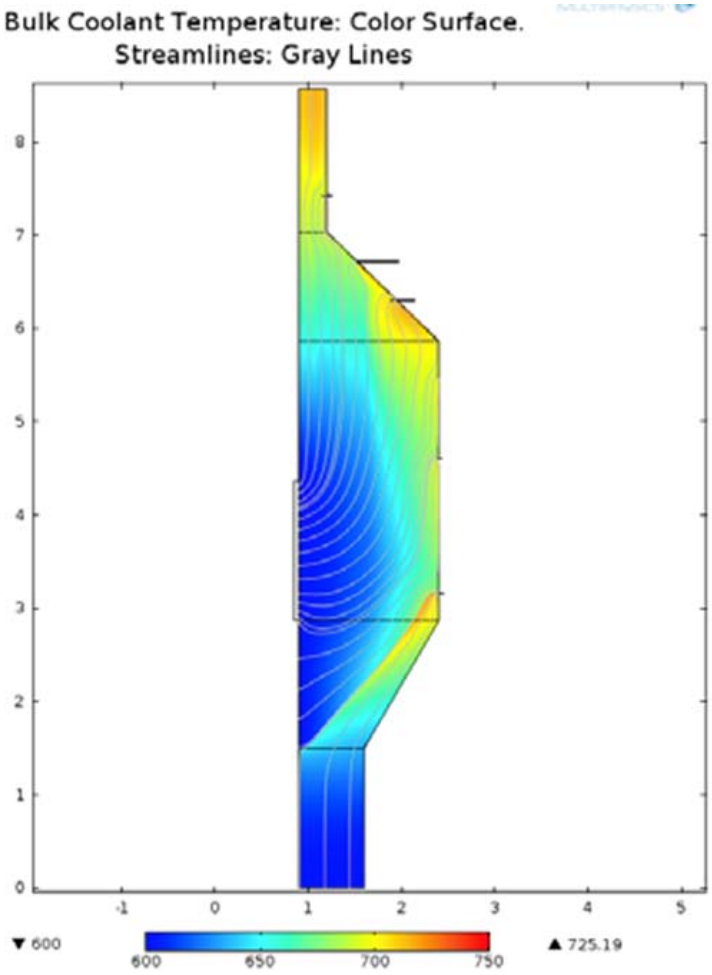

Figure 7.2: Bulk coolant temperature (°C) distribution in the PB-FHR core under normal operating conditions, calculated in COMSOL multiphysics.

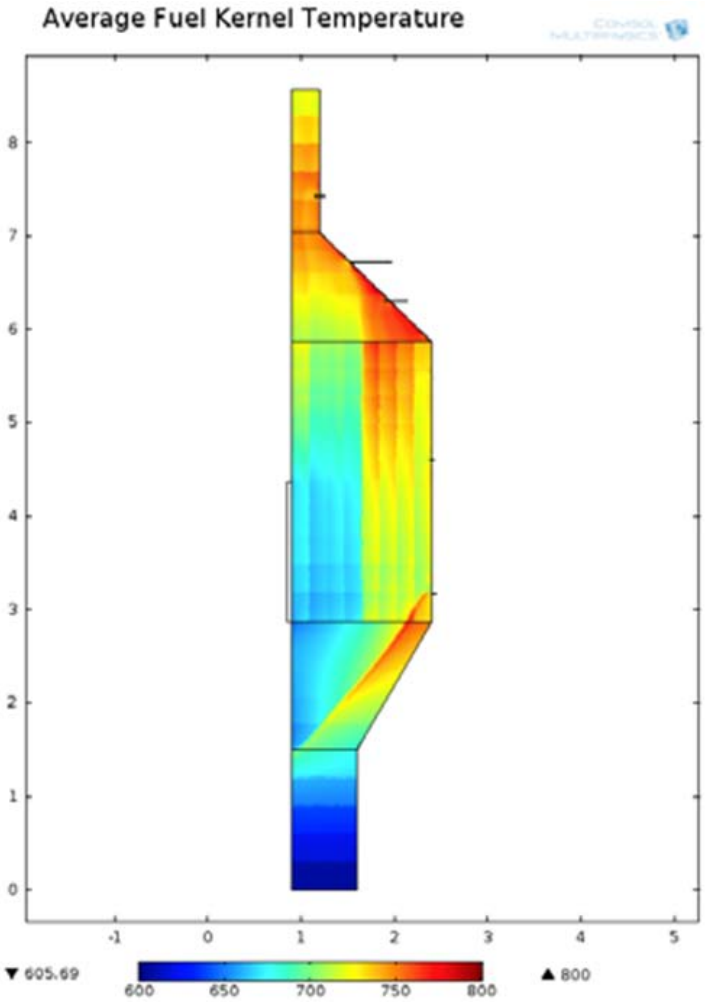

Figure 7.3: Fuel temperature (°C) distribution (average kernel temperature in fuel pebble) in the PB-FHR core under normal operating conditions, calculated in COMSOL multiphysics.

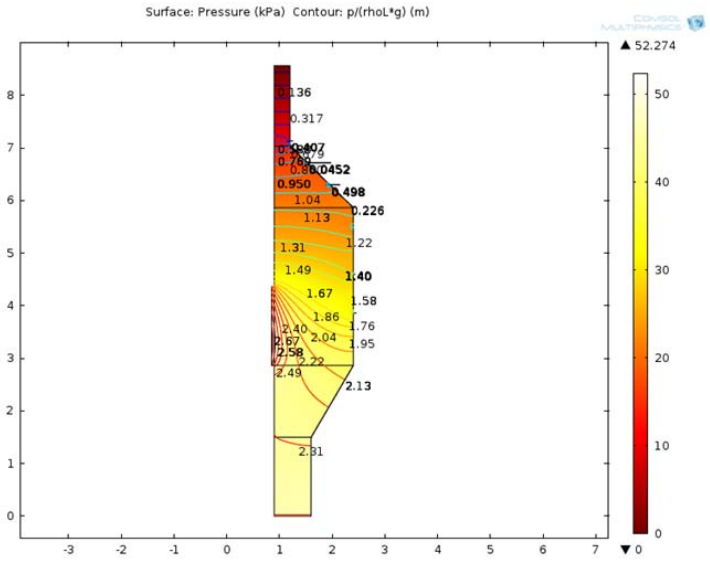

Figure 7.4: Pressure (kPa) distribution in the PB-FHR core under normal operating conditions, calculated in COMSOL multiphysics.

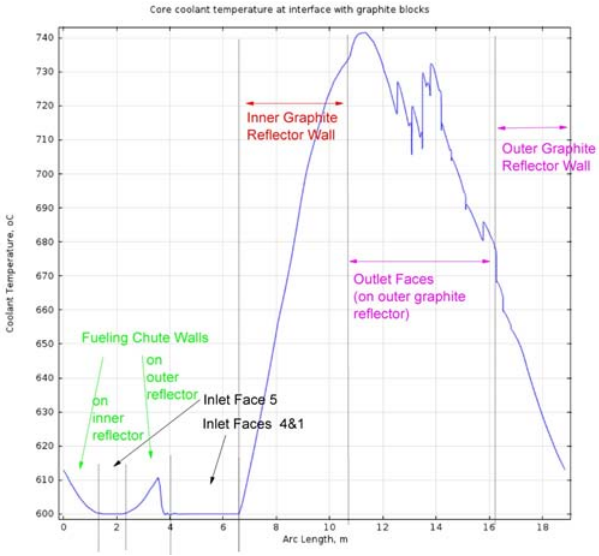

Figure 7.5: Pressure (kPa) Distribution in the PB-FHR core under normal operating conditions, calculated in COMSOL multiphysics.

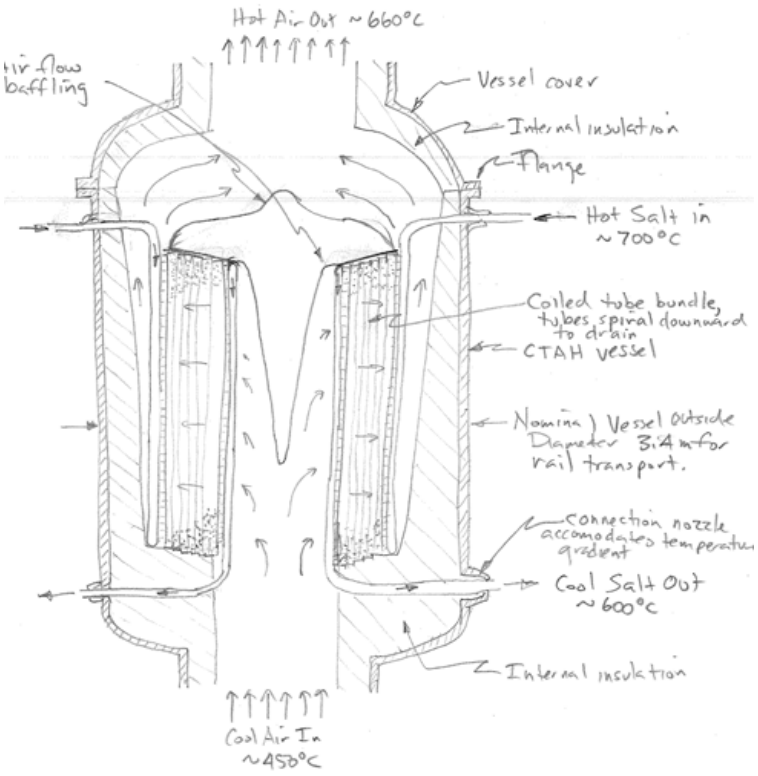

Figure 7.6: Elevation View of the CTAH.

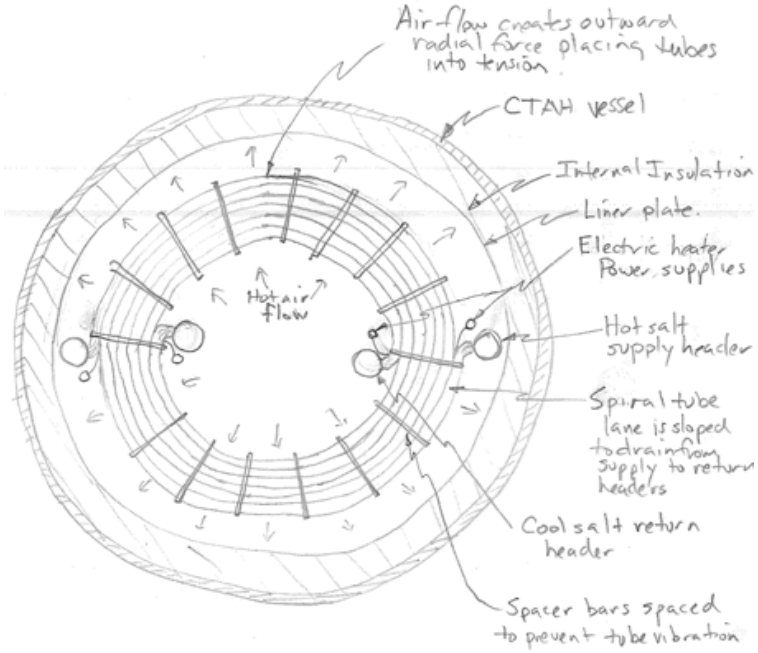

Figure 7.7: Plan View of the CTAH.

and air Reynolds number. A picture of this test bundle is shown in Figure 7.8 and experimental parameters are summarized and compared to FHR prototypical parameters in Table 7.2. These CTAHs are designed to match the 236 $MW_{th}h$ thermal power of the Mk1 PB-FHR design, and thus the areas should be scaled by the thermal power ratio when compared to the 900 $MW_{th}h$ design parameters.

Figure 7.8: Top view of coiled tube bundle (left) and detailed view of tubes support structure (right).

These studies are instrumental in designing the PB-FHR for optimal flow distribution and heat transfer, and more specifically in the design of a chemistry control system to perform redox control and reduce components corrosion, as well as to control and recover tritium.

Table 7.2: Prototypical and experimental CTAH parameters.

	CTAH (Prototype)	CTAH (Model)
CTAH thermal power ($MW_{th}h$)	118	118
Tube-side fluid	Flibe	Water
Tube inner diameter (mm)	4.57	4.57
Radius of curvature to middle of tube bank (m)	1.9	0.38
Height of tube bank (m)	6	0.25
Total tube length (m)	270,065	200
Air Reynolds number	5,902	5,902
Flibe/water Nusselt number	3.66	3.66

7.3 Loop Cleaning and Passivation System Design

The use of NF_3 to reduce oxides and passivate metal layers can have large benefits. A potentially practical approach has been developed to perform this cleaning process prior to loop startup for the primary loop. During startup, the MSRE operated its primary and intermediate loops with helium circulated by the primary and intermediate pumps to maintain constant temperature during loop heating from ambient temperatures. In the FHR, the cleaning process must occur before graphite structures are placed inside the primary loop due to the capability of NF_3 to attack graphite. UCB has verified that the PB-FHR can be designed to enable circulation of helium with NF_3 through the primary system, to remove oxide layers, prior to filling the primary system with salt.

7.4 Loop Chemistry Control and Online Monitoring

Contacting the primary salt with an active metal-carbide (e.g., Be_2C, ZrC, CeC) is one option for redox control and online chemistry control in FHRs. If used, these materials should be placed in a cold trap in the system to avoid transport and deposition of active metal-carbides elsewhere in the loop. A cold trap can be used to precipitate and remove other substances even if other redox control is used (e.g., gas contacting with salt spray in the pump seal bowl). Particulates can also originate from a variety of sources and can be filtered in the cold trap, including dust formed by erosion of graphite surfaces due to pebble motion, crushed pebbles, and releases of graphite and other particles from chemistry control and tritium capture cartridges. Likewise, particulates may be introduced as foreign material during manufacturing, installation, and maintenance of equipment. Small graphite dust particulate is expected to accumulate at the salt free surfaces, particularly around the defueling machine and the hot well, where it can be skimmed. The defueling machines are designed to recover and remove broken pebble fragments. Other particulates are expected to be filtered primarily by tritium removal cartridges in the CTAH vertical manifold pipes.

Cold traps for redox control have been implemented in the pre-conceptual design of the FHR.

Cooled salt exiting the bottom of each CTAH flows in a downward sloping pipe over to a stand pipe, which serves several functions, including providing access to replace redox control and filter cartridges in the cold trap at the bottom of the stand pipe, and providing a flow path to drain the loop to a drain tank, as shown in Figure 7.9. Three potential redox control agents are considered for use: (1) a mixture of cerium carbide (CeC_2) and graphite particles, (2) a mixture of zirconium carbide (ZrC) and graphite particles, and (3) a mixture of beryllium carbide (Be_2C) and graphite particles. These cartidges are designed to be readily removable and replaceable.

Each cold leg has a seal loop, which allows the stand pipe to be drained for maintenance without draining the upper horizontal cold leg section. A gate valve in each stand pipe provides additional capability to isolate each upper horizontal cold leg. Moreover, each main salt loop has a drain tank, connected to the bottom of the cold leg stand pipe by a small diameter line with a freeze valve. The drain tank is equipped with insulation, electrical heating, and additional transfer lines to allow salt to be added or removed using portable transfer containers. If determined to be beneficial during detailed design, the drain tanks may also be lined with nickel so that the salt they contain can be purified by HF/H_2 sparging. Cover gas for the drain tanks is supplied by the cover gas inventory control system. Coolant inventory control is performed primarily by the hot well, which can accommodate coolant volume changes due to temperature changes, as well as volume changes due to level swell at other free surfaces in the loop as pump speeds are changed.

7.5 Major Component Design

This task will use corrosion data and models to develop designs and operations/maintenance approaches for major loop components including heat exchangers, pumps, pipes, vessels, and core internals. Lifetime requirements and replaceability will be considered in recommending whether components should be clad (vessels and pipes may merit cladding). This task will also identify methods for online monitoring and for in-service inspection methods to detect and measure corro-

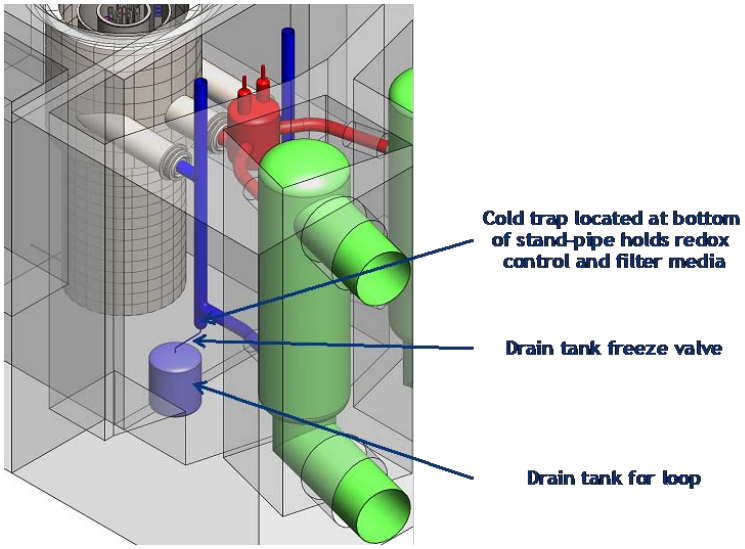

Figure 7.9: Cold leg stand pipe system with lower chemistry control cold trap well and drain line.

sion or corrosion product deposition in major loop components (particularly heat exchangers).

Based upon review of the issues with managing the effects of corrosion, UCB has developed several management methods that it is implementing into the Mk1 PB-FHR design. These include providing stand-pipes for material sample coupons in the reactor center reflector, core barrel, CTAH hot and cold manifold pipes, and DRACS heat exchanger manifold pipes. The design also makes all equipment inspectable and replaceable, including the reactor vessel.

Chapter 8

Path Forward

New nuclear molten salt initiatives face many engineering challenges such as rebuilding the previous molten salt knowledge base and commercialization issues. One of the greatest materials issues is that Hastelloy-N, the alloy used for molten salt containment in the MSRE, is not qualified by the ASME Boiler and Pressure Vessel Code under Sections I, III, B31.1, and B31.3 [126, 127]. To code certify an alloy is a costly and time consuming process. Creep tests have to be performed which evaluate an alloy's ability to retain its form under high temperature and pressure for many years. On top of certifications, the problem of neutronics damage of Hastelloy-N is still open. Current work has shown that even modified versions Hastelloy-N can only withstand 650°C maximum in neutron fluxes [128]. Lastly, the main component in Hastelloy-N, nickel, is very expensive. The time and money issues associated these issues makes investigating the compatibility of existing certified alloys, such as stainless steel 316, 304 or Incoloy 800H, for use with fluoride salts a valid pursuit.

Figure 8.1 shows a list of five alloys which are currently evaluated for long lifetime service in a high temperature environment. Of these alloys, 304 and 316 SS have the highest temperature rating, followed by Incoloy 800H alloy. These three high temperature alloys rely on large portions of chromium in their composition. For instance, 316 stainless steel has between 16-18%, 304 stainless steel has between 17.5-20%, and Incoloy 800H contains between 19-23%. As previously discussed, chromium tends to be the first element thermodynamically attacked by molten fluoride salts. Therefore, it is thought that if any certified alloys were to be used, the one with lowest chromium content would be the best: 304 stainless steel. However, it might be desirable to have the extra strength of 316 stainless steel at higher temperatures and a little extra chromium content. Other alloys, 2.25Cr-1Mo and 9Cr-1Mo-V, are largely iron based and have significantly

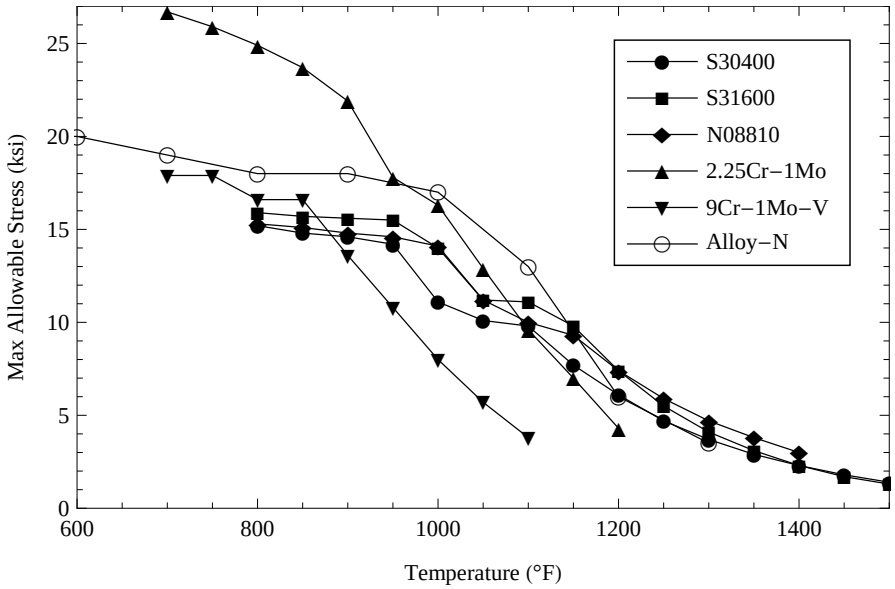

Figure 8.1: The maximum allowable stress as a function of temperature for all Section III Rules for Construction of Nuclear Facility Components - Division 1: Subsection NH - Class 1 Components in Elevated Temperature Service alloys and Hastelloy-N [129, 130]. Hastelloy-N stresses shown are not rated by the ASME and therefore are artificially larger than the other five alloys.

less chromium, however these alloys are rated for a maximum of 600°C and 650°C which is too low for an FHR.

The rest of this chapter will assume the material of construction for the elevated temperature components will be 316 stainless steel and that the reactor design chosen will be the University of California - Berkeley (UC-B) pebble bed FHR design. Special consideration will be given towards chromium and the reactor design itself.

8.1 Fluoride Salts and Code Certified Alloys

Previous work has been conducted with fluoride salts and stainless steel. Most recently, Sellers found that stainless steel and flinak in contact with graphite experienced less than 3 mg cm^2 of weight loss, a number less than more noble alloys studied by Olson [24, 33]. Additionally, Sellers found that zirconium additions in flinak caused all 316 stainless steel samples to gain weight,

rather than lose it [33]. These weight gains were actually in the form of nickel, zirconium, and oxygen based compounds as shown in Figure 8.2. X-ray diffraction found the compounds Zr_3NiO,

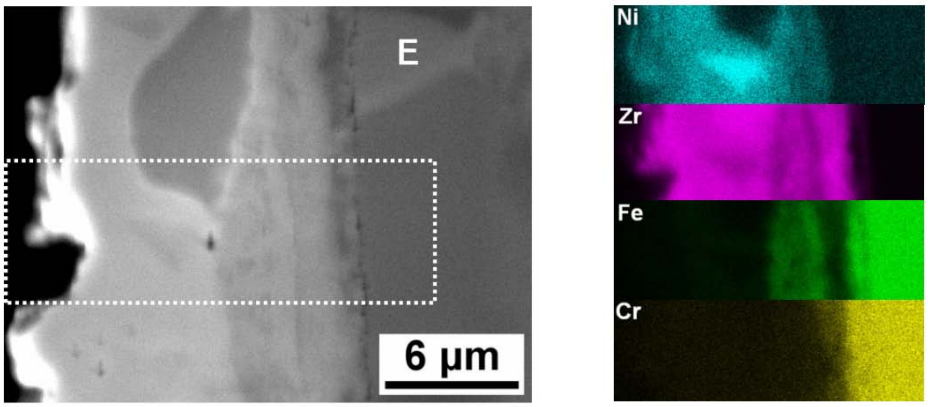

Figure 8.2: EDS cross-sectional micrograph and distribution showing weight gain of 316L stainless steel in the presence flinak and graphite at 850°C for 1000 hours [33].

$NiZr_2$, and ZrO_2. The layers adhered above the layer of iron and chromium as a sort of passivated layer [33]. They were were brittle, and easily fell off the metallic substrate. The brittle nature of the layer meant that changes in thermal expansion from the substrate to the Ni-Zr layer could cause cracking in the coating during thermal shock or cycling [33]. It was eventually concluded that this passivation layer in these conditions would not be viable option to prevent stainless steel corrosion. Additionally, Sellers admits that too much zirconium was added, which contributes to this behavior.

In 1977, Keiser et al. found that flibe and stainless steel experienced low corrosion rates in a dynamic corrosion loop, near the limits of detection, only after the periodic or permanent introduction of beryllium metal [50]. Rates were observed as $10\mu yr^{-1}$ initially and dropped as impurities were consumed [50]. Other reports from Oak Ridge have indicated that stainless steels perform decently in the salt, occasionally experiencing less corrosion than nickel and nickel based alloys [3, 17]. It can be concluded from this data that fluoride salts might be able to be used in nuclear applications with the proper level of fluorine potential control.

Simpson et al. found results similar to Sellers: too much reducing agent can be added to salt

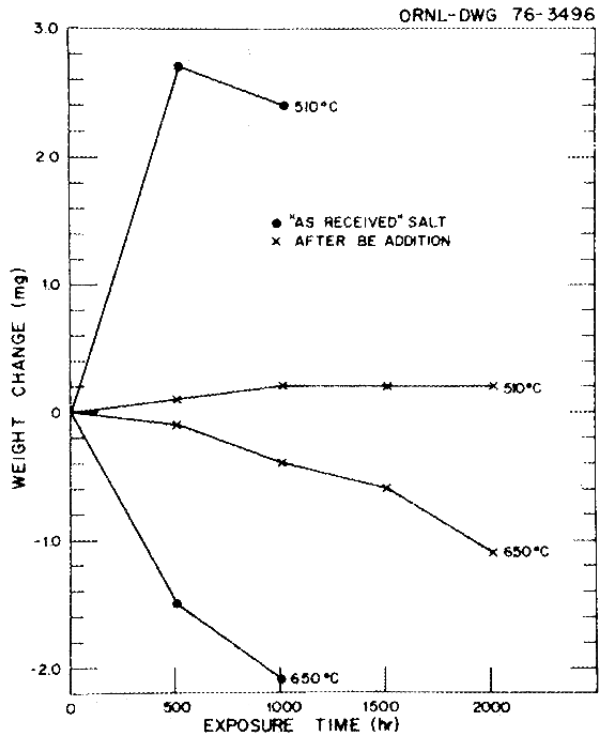

Figure 8.3: Corrosion rate of 316 stainless steel using flibe with and without redox in a natural circulation test loop.

[131]. In a study where beryllium metal was submerged in salt contained in a nickel crucible for 210 hours at 803 K the beryllium was found to lose 25% of its volume. Examination of the nickel crucible found a concentrated beryllium layer of around 60 atomic % with nickel at 25 atomic % [131]. It was concluded that excess reducing agent will corrode galvanically and deposit on other surfaces. This is highly undesirable for reaction operation. Essentially, thermodynamic corrosion is stopped, but galvanic corrosion is encouraged.

It seems natural that the best way to control salt fluorine potential is through a reducing agent which will not experience a galvanic couple or cause necessary deposits. If a redox agent existed like this, too much could never be added–all effects would be thermodynamic, avoiding unwanted alloying of the canisters. One reducing couple which does not experience galvanic coupling is hydrogen gas.

As mentioned in Section 2.5.1 there are three main ways to control fluorine potential: H_2:HF

gas, metal additions, and dissolved metals with multiple oxidation states. The effectiveness of metals depends entirely on the activity, Gibbs free energy of formation, and solubility of that metal. In the case that the metal with proper energetics is poorly soluble or the activity is undesirable, its control of the fluorine potential will be poor. These two quantities are entirely chemically as well, and cannot be manipulated. The hydrogen- hydrogen fluoride couple fluorine potential depends entirely on the ratio of partial pressures of hydrogen and hydrogen fluoride, as seen in Eq. 2.40. These quantities are physical, and while the hydrogen fluoride potential might not be able to be controlled due reactor conditions, hydrogen could always be compensated. However, hydrogen at atmospheric pressure has been shown to be mostly only able to reduce iron and nickel. In salt heavily populated with chromium, reducing agents were used [5]. It is suggested that through the pressurization of pre-cleaned flibe with hydrogen gas through a sparging system, acceptable levels of corrosion could be achieved with alloys with large amounts of chromium.

8.2 Basis for Hydrogen Pressure Redox Control

In order to prevent the formation of CrF_2, a minimum fluorine potential will have to be met. Unfortunately, the reversible nature of many fluoride salt reactions denies a distinct line between corrosion, and no corrosion. Therefore, experimental data must be used in order to determine the corrosion limits, as determined by concentrations of corrosion products in the salt. The salt will move towards this corrosion level at an undetermined rate and will cease corrosion once it is met.

The empirical basis for fluorine potential control comes from Blood, who determined the experimental constants previously listed in Table 2.1. Blood found that it is not necessary the total pressure of hydrogen fluoride and hydrogen, but the ratio of the two pressures, which is also indicated by Olander. Therefore the deciding factor for hydrogen pressure control is the rate of hydrogen fluoride introduction, dependent on radiolysis, gas leakage, sparge gas impurities, and what ratio of hydrogen in what form, bubble or dissolved, is necessary to combat that hydrogen

fluoride. Additionally, the rate of hydrogen fluoride gas removal from the salt is very important. In order for this technique to work for corrosion control, the hydrogen fluoride must be removed to artificially increase the ratio.

8.3 Hydrogen Fluoride Production in a Fluoride Salt Reactor

An operating fluoride salt reactor will produce tritium, and ultimately tritium fluoride, production rate of roughly 29.03 mCi s^{-1}, or 1×10^{-6} mol s^{-1} [132]. This comes from a mixture of several reactions. The first reaction stems from beryllium-9 absorbing a neutron

$$n +^{9} Be \rightarrow^{6} He +^{4} He, \tag{8.1}$$

where helium-6 decays

$$^{6}He \rightarrow^{6} Li + e, \tag{8.2}$$

producing lithium-6 which is able to react and form tritium

$$n +^{6} Li \rightarrow^{4} He +^{3} H. \tag{8.3}$$

The other tritium term is through lithium-7

$$n +^{7} Li \rightarrow n +^{3} H +^{4} He. \tag{8.4}$$

Each one of these reactions preserves the fluorine atom, which will allow any available products to combine with it after the nucleosynthesis if given the chance, thus causing chemical changes to the salt and affecting the fluorine potential. The predominate reactions are

$$2n + BeF_2 \rightarrow TF + F^{-} + 2He \tag{8.5}$$

and

$$\mathrm{n} + \mathrm{LiF} \rightarrow \mathrm{TF} + \mathrm{He}. \tag{8.6}$$

Potentially, some of this tritium will not recombine and will not produce tritium fluoride as shown in Eqs. 8.5 and 8.6 [133]. It has been determined that the large portion is in fact TF [133, 134]. Regardless, the worst case scenario for chemical control would be the production of all tritium fluoride and no tritium. This case will be considered for the chemical control.

8.4 Hydrogen Gas Counterpressure

To calculate the hydrogen gas pressure needed to counteract the hydrogen fluoride terms, data from Section 2.3.4, measured solubilities of Cr, Fe, and Ni in Flibe, can be used. Assuming a stainless steel will be used, chromium will be the most vulnerable towards corrosion, therefore hydrogen pressure should be based off of that element. The production terms of hydrogen fluoride, one of which was discussed in Section 8.3, are from tritium production, hydrogen gas water impurities, and leakage from the atmosphere. Both the leaks and impurities go on to produce HF through hydrolysis. Of these three, two can be mitigated through the use of relatively pure hydrogen gas and by leak testing the system properly. For these calculations the standard of 35 ppm of chromium in the salt will be used. The allowable hydrogen content is then equal to

$$p_{\mathrm{H_2}} = \frac{p_{\mathrm{HF}}^2}{K_N N_{\mathrm{CrF_2}}}. \tag{8.7}$$

Partial pressures can be converted to moles through the use of the ideal gas law

$$n_{\mathrm{H_2}} = \frac{n_{\mathrm{HF}}^2 RT}{K_N N_{\mathrm{CrF_2}} V}, \tag{8.8}$$

where V is the volume of salt in the core. The rate of change of both moles of hydrogen will have to be balanced to preserve the fluorine potential

$$\dot{n}_{H_2} = \frac{\dot{n}_{HF}^2 RT}{K_N N_{CrF_2} V}. \tag{8.9}$$

As mentioned before the HF production rate is just that of the tritium fluoride, atmospheric water leakage, and concentration of water impurity in the hydrogen counter pressure

$$\dot{n}_{HF} = \dot{n}_{TF} + \dot{n}_{leak} + \dot{n}_{impurity} \tag{8.10}$$

Where the term $\dot{n}_{impurity}$ can be replaced by percentage of water in the hydrogen gas, which for ultra high purity hydrogen is around $\gamma = 2 \times 10^{-6}$, multiplied by the rate at which it is introduced, multiplied by the amount of HF produced per mole water which is two. Assuming the leaks can be completely stopped through the use of a helium mass spectrometer the rate of hydrogen introduction is

$$\dot{n}_{H_2} = \frac{(\dot{n}_{TF} + 2\gamma\dot{n}_{H_2})^2 RT}{K_N N_{CrF_2} V}. \tag{8.11}$$

Which yields a solvable quadratic equation for $\dot{n}_{H_2}$. It was found that hydrogen gas impurities are nearly entirely negligible. Hydrogen counter pressures are shown at three temperatures in Table 8.1 Due to the quadratic nature of Eq. 8.7 low partial pressures of hydrogen fluoride allow equally low

Table 8.1: Calculation of hydrogen counter pressures required to keep 10 ppm of chromium in solution assuming $V = 7.2\text{m}^3$ of flibe in the core from the UC-B pebble bed FHR.

Temperature (°C)	K_N (atm)	TF Production (mol s^{-1})	Hydrogen Counter (mol s^{-1})	(L m^{-1})
750	1.92×10^{-4}	1.00×10^{-6}	1.74×10^{-6}	8.16×10^{-4}
800	4.42×10^{-4}	1.00×10^{-6}	7.91×10^{-7}	3.72×10^{-4}
850	1.19×10^{-3}	1.00×10^{-6}	3.07×10^{-7}	1.45×10^{-4}

amounts of hydrogen counter pressure. The thermodynamics however, cannot predict the rate of

removal of hydrogen fluoride from the salt which depends on the solubility of hydrogen fluoride in flibe and diffusion of hydrogen fluoride into hydrogen sparge gas and out of the salt. If all hydrogen fluoride was able to bubble out of the salt, the total amount of hydrogen needed to counteract the hydrogen fluoride would be 1.74×10^{-6} mol s^{-1}, a ratio of roughly 1:2 HF-H_2.

8.5 Gas Solubility in Flibe

The first method of introducing required quantities of hydrogen into flibe could be through application of Henry's Law. Henry's Law dictates that the solubility of a gas in a liquid is proportional to the partial pressure of the gas above the liquid multiplied by an equilibrium factor K_H. This relation exists mathematically as

$$p = K_H c \tag{8.12}$$

where c is the concentration of the gas in the liquid, while p is the partial pressure of that gas above liquid. The law also determines the amount of hydrogen fluoride which can exist in the salt. The values of K_H have been measured at a handful of temperatures in flibe salt for many gases [135, 136, 137]. These properties were mainly measured for chemical purification purposes and to evaluate the effect of gas fission products in the liquid salt. It can be seen that the hydrogen fluoride

Table 8.2: Solubility of hydrogen and hydrogen fluoride per liter LiF-BeF_2 (66-34 mol%) [135, 136].

Temperature (°C)	K_H H_2 (mol L^{-1} atm^{-1})	K_H HF (mol L^{-1} atm^{-1})
500	1.78×10^{-5}	2.09×10^{-2}
600	4.43×10^{-5}	1.30×10^{-2}
700	4.85×10^{-5}	8.90×10^{-3}

gas is roughly 1000 times more soluble than hydrogen at any given temperature. For comparison, the solubility of nitrogen in water is roughly 6.1×10^{-4} mol L^{-1} atm^{-1}, CO_2 is 3.4×10^{-2} mol L^{-1} atm^{-1}. Therefore, it seems that while hydrogen is hard to dissolve in the salt it is not impossible.

Using preliminary calculations from the UC-B FHR design, the pressurization required for hydrogen control using purely dissolved hydrogen can be determined using this data. Flow rates in the hot leg are 0.562 $m^3\ s^{-1}$ and 0.548 $m^3\ s^{-1}$ in the cold leg. Therefore it can be assumed in the core averages around 0.555 $m^3\ s^{-1}$, resulting in a travel time of a little less than 13 seconds through the 7.2 m^3 core. In this time 1.3×10^{-5} moles of tritium fluoride will be produced, requiring a total of 2.93×10^{-4} moles of hydrogen distributed through volume of the core in order to preserve 10 ppm of Cr. Using values from Table 8.2, it can be determined that 8.4×10^{-4} atm of over pressure is required to achieve this concentration of hydrogen gas in the flibe. It is important to realize that these calculations are only valid under the condition that hydrogen fluoride is continuously removed from the salt and that concentrations in the salt are small.

8.6 Corrosion of Pyrolytic Carbon

The UC-B pebble bed FHR uses TRISO fuel which has an outer coating of pyrolytic carbon. Pyrolytic carbon is chemically identical to elemental carbon. Carbon can react in the presence of hydrogen gas to form methane through the reversible process

$$C + H_2 \leftrightharpoons CH_4. \tag{8.13}$$

This process could cause corrosion of the fuel, potentially to the point where the fuel becomes compromised. Interestingly, the reaction becomes reversible around the operating temperature of a fluoride salt cooled reactor. The K_{eq} values, shown in Table 8.3, become less than one around 550°C. This means that the reaction becomes reactant favored at this point. This can be further explained through the set up of the equilibrium equation

$$K_{eq} = \frac{p_{CH_4}}{p_{H_2}^2}, \tag{8.14}$$

Table 8.3: K_{eq} for the reaction $C + H_2 \leftrightharpoons CH_4$ over operation temperatures which might be seen in a fluoride salt cooled reactor.

Temperature (°C)	K_{eq}
500.000	2.176
600.000	4.634×10^{-1}
700.000	1.332×10^{-1}
800.000	4.775×10^{-2}
900.000	2.026×10^{-2}
1000.000	9.801×10^{-3}

where as K_{eq} decreases, the amount of methane required to create equilibrium with the hydrogen and the carbon decreases. Additionally, the amount of methane required to preserve K_{eq} increases quadratically with hydrogen.

In a fluoride salt cooled reactor core, where large amounts of flibe exist in contact with graphite, a mixture of methane and hydrogen could be used according to Eq. 8.14, to allow hydrogen to exist with the carbon with minimal corrosion. The hydromethanation couple is the same concept as the hydrogen, hydrogen fluoride, chromium fluoride couple. However, the effects of having methane, hydrogen, and pure salt together, without graphite present are unknown. Potentially, some methane would decompose into carbon and hydrogen producing carbon particulate in the salt. The common method of removing carbon from salt during the purification process was through a hydrogen sparge. Through this mechanism, it might be possible for excess methane required to keep TRISO fuel intact to decompose in the salt, but be carried away through the hydrogen sparge.

8.7 Tritium Removal from Flibe Salt

As mentioned before, nearly all tritium in the salt exists as the chemical species of tritium fluoride [133, 134]. Some of it forms into T_2 if it corrodes a metal [134]. For instance a reaction with

chromium would be

$$2TF + Cr \rightleftharpoons CrF_2 + T_2. \tag{8.15}$$

This reaction should not occur in a system with excess hydrogen. However, if this tritium is in the in the presence of hydrogen the compound HT can be formed.

$$T_2 + H_2 \rightleftharpoons 2HT. \tag{8.16}$$

These three compounds behave chemically as hydrogen and all have the potential to exist. Another possible reaction with the TF can occur in the salt when it disassociates in the presence of dissolved hydrogen is

$$2T^+ + 2F^- + 2H^+ \rightleftharpoons 2HF + T_2. \tag{8.17}$$

The extent of this reaction is unknown and there exists no chemical basis for estimating its equilibrium. All these tritium reactions must be given special attention, as the form they are in determines if they can be removed before they can migrate through hot heat exchangers. If they are allowed to migrate and find a way out of the reactor a contamination issue could be created [132, 134]. This problem was seen in the molten salt reactor, and is highlighted through the tritium content in the secondary loop coolant salt, which was previously discussed. It would be advisable to remove these compounds before they can meet the heat exchanger, preferably directly after the reactor core produces them.

Oishi et al. was able to determine by using a sweep gas of helium and hydrogen that the tritium fluoride could be removed from irradiated flibe at a exponentially decreasing rate at a temperature of 873K [133]. The liberated tritium fluoride could then be condensed and removed from the sweep gas. After condensing the tritium fluoride, some HT was still in the mixture. To remove this a reaction was performed, most likely burning with oxygen, to produce condensed, tritated water.

8.8 Hydromethanation

It is suggested for the FHR that a slight over pressure of hydrogen be kept in all salt bearing locations. This over pressure of a few psi will prevent oxygen and water from entering the salt while dissolving hydrogen into the salt for chemical control via Henry's Law. As shown before, not much hydrogen is needed for controlling the tritium in the core, as long as all the tritium fluoride can be removed.

Removing the tritium fluoride is very important to preserving the small amount of hydrogen needed for 10 ppm of chromium control. To due this, a sparge of hydrogen or inert gas could be performed after the core. This sparge rate will depend on the effectiveness of tritium fluoride removal by the sparge gas. The overall effectiveness can be measured by comparing the activity of the tritium fluoride removed to the theoretical activity of tritium produced in the reactor. Sparge rates can be increased or decreased dependent of the efficiency of removal. Any leftover gaseous T_2 or HT can be re-introduced into the hydrogen sparge. The amount of this gas is directly related to the corrosion and control of the fluorine potential and should be minimal in a healthy system. This slightly tritium contaminated salt can then be circulated through the rest of the system, including the heat exchangers, with minimal worries about migration. Additionally, since the tritium fluoride was removed, the salt will be minimally corrosive and ready for another round in the core.

To prevent carbon TRISO fuel particles from being corroded, a slight amount of methane is needed, around 0.1 psig for a 3 psig over pressure of hydrogen. This hydromethanantion could help tritium be removed from the reactor while simultaneously provide good corrosion control on the graphite and stainless steel. This methane could be dissolved in the salt can be circulated with the flibe. Unfortunately, numbers on methane solubility in flibe are non-existent, therefore this might change the overhead pressure, it should be within sub atmosphere numbers.

8.9 Potential Experimental Evaluation

In order to test the potential of hydrogen and hydromethanation a series of small scale tests are desired. Tests will be performed in a welded container with a gas sparge tube, salt transfer tube, and outlet. Coupons can be loaded in and then removed at a later date in a glove box. Heating can be performed by tape heaters. A planned initial test matrix is shown in Table 8.4. Since nickel is

Table 8.4: Proposed test matrix for evaluating the effect of hydrogen pressure in a salt.

Crucible	Container	Coupon	Reducing Agent	Time
1	Nickel	316 SS	Added Be	1000 hr
2	Nickel	316 SS	Hydrogen - 1 ATM	1000 hr
3	316 SS	316 SS	None	1000 hr
4	316 SS	316 SS	Hydrogen - 1 ATM	1000 hr
5	316 SS	316 SS	Hydrogen - 2 ATM	1000 hr
6	316 SS	316 SS	Hydrogen - 4 ATM	1000 hr

nearly impervious to corrosion on reasonable time scales to salt, crucibles one and two will use this as their material. Additionally, this will cause free fluorine ions to concentration almost entirely on the chromium in the stainless steel, accelerating corrosion of the coupons. In order to counteract this, both crucibles will have a redox agent. Crucible one will use a preloaded chunk of beryllium, while crucible two will use a hydrogen sparge to see if this is comparable.

The 316 SS tests should be more extensive. First, a control should be used which shows the effect of salt on the stainless steel without redox. In fresh flibe the corrosion should be minimal. The next three tests will test the effect of hydrogen sparge and pressurization on the salt. Of interest is the difference between pressurization tests and therefore dissolved hydrogen. If the hydrogen sparge and pressurization works, it will be evaluated to what extent using SEM on the coupons and NAA on the salt. From there, the proper test matrix can be set up to test graphite and stainless steel together.

Purity in these tests is the most important parameter. All tests, and coupons will have to be

flushed with flibe before hand and secured under an inert atmosphere until the test flibe is put in. At no time can the canister be opened to air or water. It is suggested a daisy chained filling system straight from the purification system be used in order to accomplish this daunting task. A test matrix for the hydromethanation tests would use all 316 SS in the event that the corrosion can be controlled to reasonable rates with the 316 SS. In the event that stainless steel proves unworthy in the initial tests, it is proposed that a nickel based alloy be used to evaluate carbon, methane, hydrogen, and flibe together.

Bibliography

[1] H. G. MacPherson. The Molten Salt Reactor Adventure. *Nuclear Science and Engineering*, 90:374–380, 1985.

[2] Alvin M. Weinberg. *The First Nuclear Era: The Life and Times of a Technological Fixer*. Springer, 1994. ISBN 978-1563963582.

[3] L.S. Richardson, D.E. Vreeland, and W.D. Manly. Corrosion by Molten Fluorides. Technical Report ORNL-1491, Oak Ridge National Laboratory, 1953.

[4] Jackson Harvey DeVan. *Effect of Alloying Additions on Corrosion Behavior of Nickel-Molybdenum Alloys in Fused Fluoride Mixtures*. PhD thesis, University of Tennessee, Oak Ridge, 1969.

[5] James H. Shaffer. Preparation and Handling of Salt Mixtures for the Molten Salt Reactor Experiment. Technical Report ORNL-4616, Oak Ridge National Laboratory, 1971.

[6] H. G. MacPherson. Report of the Fluid Fuel Reactors Task Force to the Division of the Reactor Development. 1959.

[7] Paul N. Haubenreich and J. R. Engel. Experience with the Molten-Salt Reactor Experiment. *Nuclear Applications and Technology*, 8, 1970.

[8] Roy E. Thoma. Chemical Aspects of MSRE Operations. Technical Report ORNL-4658, Oak Ridge National Laboratory, 1971.

[9] U.S. DOE Nuclear Energy Research Advisory Committee and Generation IV International Forum. A Technology Roadmap for Generation IV Nuclear Energy Systems. Technical report, 2002.

[10] J. J. Duderstadt and L. J. Hamilton. *Nuclear Reactor Analysis*. John Wiley and Sons, 1976.

[11] Piyush Sabharwall, Matt Ebner, Sohal Manohar, Phil Sharpe, Mark Anderson, Kumar Sridharan, James Ambrosek, Luke Olsen, and Paul Brooks. Molten Salts for High Temperature Reactors: University of Wisconsin Molten Salt Corrosion and Flow Loop Experiments - Issues Identified and Path Forward. Technical Report INL/EXT-10-18090, Idaho National Laboratory, 2010.

[12] Manohar S. Sohal, Matthias A. Ebner, Piyush Sabharwall, and Phil Sharpe. Engineering Database of Liquid Salt Thermophysical and Thermochemical Properties. Technical Report INL/EXT-10-18297, Idaho National Laboratory, 2010.

[13] D. F. Williams. Assessment of candidate molten salt coolants for the NGNP/NHI Heat-Transfer Loop. (June), 2006. URL https://inlportal.inl.gov/portal/server.pt/gateway/PTARGS_0_2_3310_277_2604_43/http;/inlpublisher;7087/publishedcontent/publish/communities/inl_gov/about_inl/gen_iv___technical_documents/ornl_tm_2006_69_htl_salt.pdf.

[14] Per F. Peterson. The Pebble-Bed AHTR Liquid Salt Cooled Reactor. In *Forum on Small and Medium Reactors (SMRs): Benefits and Challenges*, University of California, Berkeley, 2010.

[15] Charles W. Forsberg, Per F. Peterson, and Picard S. Pickard. Molten-salt-cooled advanced high-temperature reactor for production of hydrogen and electricity. *Nuclear Technology*, pages 1–25, 2003. URL ftp://liblice2008.ujv.cz/Liblice2008/Literature/lit06/new-gif/hydrogen/AHTR.Nuclear.Technology.Article.May20.2003.pdf.

[16] Charles W. Forsberg. Fluoride-Salt-Cooled High-Temperature Reactors for Power and Process Heat, 2011.

[17] D. F. Williams, L. M. Toth, and K. T. Clarno. *Assessment of Candidate Molten Salt Coolants for the Advanced High-Temperature Reactor (AHTR)*. Number March. 2006. ISBN 1800553684.

[18] W. R. Grimes, D. R. Cuneo, F. F. Blakenship, G. W. Keilholtz, H. F. Poppendiek, and M. T. Robinson. Chemical Aspects of Molten Fluoride Salt Reactor Fuels. In *Fluid Fuel Reactors*, pages 569 – 594. Addison-Wesley, 1958.

[19] R. B. Briggs. Molten-Salt Reactor Program: Semiannual Progress Report for Period Ending July 31, 1964. Technical report, 1964.

[20] H. G. MacPherson, L. G. Alexander, D. A. Carrison, J. Y. Estabrook, B. W. Kinyon, L. A. Mann, J. T. Roberts, F. E. Romie, and F. C. VonderLage. A Preliminary Study of Molten Salt Power Reactors. Technical Report 57, Oak Ridge National Laboratory, 1957.

[21] R. C. Robertson. MSRE Design and Operations Report Part I Description of Reactor Design. Technical Report ORNL-TM-0728, Oak Ridge National Laboratory, 1965.

[22] D F Williams and L M Toth. Chemical Considerations for the Selection of the Coolant for the Advanced High-Temperature Reactor. 2008.

[23] DR Olander, GT Fukuda, and CF Baes. Equilibrium pressures over BeF2/LiF (flibe) molten mixtures. *Fusion science and technology*, pages 141–150, 2002. URL `http://cat.inist.fr/?aModele=afficheN&cpsidt=13495762`.

[24] Luke C. Olson. *Materials Corrosion in Molten LiF-NaF-KF salt*. PhD thesis, University of Wisconsin - Madison, January 2009. URL `http://allen.neep.wisc.edu/docs/dissertation-olson-luke.pdf`.

[25] J. D. Mackenzie. Structure of Glass Forming Halides. I. Liquid Beryllium Fluoride. *The*

Journal of Chemical Physics, 32(4):1150, 1960. ISSN 00219606. doi: 10.1063/1.1730864. URL http://link.aip.org/link/JCPSA6/v32/i4/p1150/s1&Agg=doi.

[26] L. M. Toth, A. S. Quist, and GE Boyd. Raman spectra of zirconium (IV) fluoride complex ions in fluoride melts and polycrystalline solids. *The Journal of Physical Chemistry*, 155 (1971), 1973. URL http://pubs.acs.org/doi/abs/10.1021/j100630a014.

[27] Theodore L Brown, H Eugene LeMay, and Bruce Edward Bursten. *Chemistry: The Central Science*. Prentice Hall, 1997. ISBN 0135334802. URL http://www.amazon.com/dp/013218642X.

[28] D. Olander. Redox condition in molten fluoride salts Definition and control. *Journal of Nuclear Materials*, 300(2-3):270–272, February 2002. ISSN 00223115. doi: 10.1016/S0022-3115(01)00742-5. URL http://linkinghub.elsevier.com/retrieve/pii/S0022311501007425.

[29] A. K. Misra and J. D. Whittenberger. Fluoride salts and container materials for thermal energy storage applications in the temperature range 973 to 1400 K. Technical report, National Aeronautics and Space Administration, Cleveland, OH (USA). Lewis Research Center, 1987. URL http://www.osti.gov/energycitations/product.biblio.jsp?osti_id=6051706.

[30] C. M. Blood. Solubility and Stability of Structural Metal Difluorides in Molten Fluoride Mixtures. Technical Report ORNL-TM-760, Oak Ridge National Laboratory, 1964. URL http://www.osti.gov/energycitations/product.biblio.jsp?osti_id=4292638.

[31] A. L. Mathews and C. F. Baes, Jr. Oxide Chemistry and Thermodynamics of Molten Lithium Fluoride-Beryllium Fluoeride by Equilibriation with Gaseous Water-Hydrogen Fluoride Mixtures. Technical Report ORNL-TM-1129, Oak Ridge National Laboratory, 1965.

[32] R. B. Briggs. Molten-Salt Reactor Program Semiannual Progress Report for Period Ending July 31, 1963. Technical Report ORNL-3529, Oak Ridge National Laboratory, 1963.

[33] R. S. Sellers. *Impact of Reduction-Oxidation Agents on the High Temperature Corrosion of Materials in LiF-NaF-KF*. PhD thesis, University of Wisconsin-Madison, 2012.

[34] W. R. Grimes. Chemical Research and Development for Molten Salt Breeder Reactors. Technical Report ORNL-TM-1853, Oak Ridge National Laboratory, 1967.

[35] James H. Shaffer and L. E. McNeese. Removal of Ni, Fe, and Cr Fluorides from Simlated MSRE Fuel Carrier Salt. Technical Report ORNL-CF-68-4-41, Oak Ridge National Laboratory, 1968.

[36] P. Calderoni, P. Sharpe, H. Nishimura, and T. Terai. Control of molten salt corrosion of fusion structural materials by metallic beryllium. *Journal of Nuclear Materials*, 386-388: 1102–1106, April 2009. ISSN 00223115. doi: 10.1016/j.jnucmat.2008.12.292. URL http://linkinghub.elsevier.com/retrieve/pii/S0022311508010659.

[37] James Ambrosek. *Molten Chloride Salts for Heat Transfer in Nuclear Systems*. PhD thesis, University of Wisconsin - Madison, 2011.

[38] AL Mathews and CF Baes Jr. Oxide chemistry and thermodynamics of molten lithium fluoride-beryllium fluoride solutions. *Inorganic Chemistry*, 7(2):373–382, February 1968. ISSN 0020-1669. doi: 10.1021/ic50060a042. URL http://pubs.acs.org/cgi-bin/doilookup/?10.1021/ic50060a042http://pubs.acs.org/doi/pdf/10.1021/ic50060a042.

[39] R. B. Briggs. Molten-Salt Reactor Program Progress Report for Period Ending July 31, 1963. Technical Report ORNL-3419, Oak Ridge National Laboratory, 1963.

[40] R. B. Lindauer and C. K. McGlothlan. Design, Construction, and Testing of a Large Molten Salt Filter. Technical Report ORNL-TM-2478, Oak Ridge National Laboratory, 1969.

[41] R. B. Briggs. Molten-Salt Reactor Program Semiannual Ptogress Report for Period Ending February 28, 1966. Technical Report ORNL-3936, Oak Ridge National Laboratory, 1966.

[42] Gerald Goldstein. Determination of Beryllium by the Photoneutron Method. *Analytical Chemistry*, 554(1):1–4, 1963. URL http://pubs.acs.org/doi/abs/10.1021/ac60204a022.

[43] R. B. Briggs. Molten-Salt Reactor Program Semiannual Progress Report for Period Ending August 31, 1966. Technical Report ORNL-4037, Oak Ridge National Laboratory, 1966.

[44] H. Bisby. Nucleonic instrumentation for the detection and assay of beryllium minerals. Technical Report AERE-R-3021, United Kingdom Atomic Energy Authority, 1959.

[45] R. F. Apple and H. E. Zittel. Amperometric Titration of Chromium in Mixtures of Fluoride Salts. *Analytical Chemistry*, 36(6):983–985, May 1964. ISSN 0003-2700. doi: 10.1021/ac60212a011. URL http://pubs.acs.org/cgi-bin/doilookup/?10.1021/ac60212a011.

[46] L. G. Saywell and B. B. Cunningham. Determination of Iron: Colorimetric o-Phenanthroline Method. *Industrial & Engineering Chemistry*, 9(2):67–69, February 1937. ISSN 0096-4484.

[47] M. T. Kelley and C. D. Susano. Analytical Chemistry Division Annual Progress Report for Period Ending Novemeber 15, 1964. Technical Report ORNL-3750, Oak Ridge National Laboratory, October 1964.

[48] Gerald Goldberg, A S Meyer, and J C White. Determination of Oxides in Fluoride Salts by High-Temperature Fluorination with Potassium Bromotetrafluoride. *Analytical Chemistry*,

32(3):314–317, March 1960. ISSN 0003-2700. doi: 10.1021/ac60159a004. URL http://pubs.acs.org/cgi-bin/doilookup/?10.1021/ac60159a004.

[49] S E Eklund, L M Toth, J Q Chambers, and G Mamantov. Determination of oxide in fluoride salts using an yttria-stabilized-zirconia oxygen pump. *Analytical chemistry*, 71(3):539–43, February 1999. ISSN 0003-2700. doi: 10.1021/ac980830j. URL http://www.ncbi.nlm.nih.gov/pubmed/21662712.

[50] J. R. Keiser, J. H. DeVan, and D. L. Manning. The Corrosion Resistance of Type 316 Stainless Steel to Li2BeF4. Technical Report ORNL/TM-5782, Oak Ridge National Laboratory, 1977.

[51] J. W. Koger. Alloy Compatibility with LiF-BeF2 Salts Containing ThF4 and UF4. Technical report, Oak Ridge National Laboratory, 1972. URL http://scholar.google.com/scholar?hl=en&btnG=Search&q=intitle:Alloy+Compatibility+iwth+LiF-BeF2+Salts+Cotaining+ThF4+and+UF4#0.

[52] Department of Energy. Chronic Beryllium Disease Prevention Program. Technical Report 10 CFR 850, Department of Energy, Washington, 1999.

[53] Materion Brush Inc. Material Safety Data Sheet - No. M12 - Beryllium Fluoride, 2011.

[54] Materion Brush Inc. Potential Health Effects from Exposure to Water Soluble Beryllium Compounds, 2011.

[55] Kenneth A. Walsh. Thermodynamics of Extraction. In Edgar E. Vidal, Alfred Goldberg, Edward N.C. Dalder, David L. Olson, and Brajendra Mishra, editors, *Beryllium Chemistry and Processing*, pages 61–62. ASM International, 2009.

[56] Kristin J. Cummings, Aleksandr B. Stefaniak, M. Abbas Virji, and Kathleen Kreiss. A reconsideration of acute Beryllium disease. *Environmental health*

perspectives, 117(8):1250–6, August 2009. ISSN 1552-9924. doi: 10.1289/ehp.0800455. URL http://www.pubmedcentral.nih.gov/articlerender.fcgi?artid=2721869&tool=pmcentrez&rendertype=abstract.

[57] OSHA. Occupational Safety and Health Guideline for Hydrogen Fluoride, 2012. URL http://www.osha.gov/SLTC/healthguidelines/hydrogenfluoride/recognition.html.

[58] DOE. DOE Beryllium Affected Workers Web Resources, 2012. URL http://www.hss.doe.gov/healthsafety/berylliumaffectedworkers/.

[59] Materion Brush Inc. Airborne Beryllium Exposure Standards. 2011.

[60] Hydrofluoric Acid Recommended Medical Treatment for Hydrofluoric Acid Exposure. Technical report, Honeywell, 2006.

[61] H. Nishimura, T. Terai, M. Yamawaki, S. Tanaka, a. Sagara, and O. Motojima. Compatibility of ferritic steels with Li2BeF4 molten salt breeder. *Journal of Nuclear Materials*, 307-311: 1355–1359, December 2002. ISSN 00223115. doi: 10.1016/S0022-3115(02)01123-6. URL http://linkinghub.elsevier.com/retrieve/pii/S0022311502011236.

[62] D. F. Williams and Fred J. Peretz. Secondary Loop Salt Tritium Analysis. 1999.

[63] B.K. McNamara, R.D. Scheele, A.E. Kozelisky, and M.K. Edwards. Thermal reactions of uranium metal, uo2, u3o8, uf4, and uo2f2 with nf3 to produce uf6. *Journal of Nuclear Materials*, 394:166–173, 2009.

[64] Frederic Lantelme and Pierre Turq. Ionic dynamics in the licl–kcl system at liquid state. *The Journal of Chemical Physics*, 77(6):3177–3187, 1982.

[65] M. Wilson and P. A. Madden. Polarization effects in ionic systems from first principles. *Journal of Physics: Condensed Matter*, 5(17):2687, 1993.

[66] Robert J. Heaton, Richard Brookes, Paul A. Madden, Mathieu Salanne, Christian Simon, and Pierre Turq. A first-principles description of liquid bef2 and its mixtures with lif: 1. potential development and pure bef2. *The Journal of Physical Chemistry B*, 110(23):11454–11460, 2006.

[67] Mathieu Salanne, Christian Simon, Pierre Turq, Robert J. Heaton, and Paul A. Madden. A first-principles description of liquid bef2 and its mixtures with lif: 2. network formation in lifbef2. *The Journal of Physical Chemistry B*, 110(23):11461–11467, 2006.

[68] Bshadrack Jabes, Manish Agarwal, and Charusita Chakravarty. Structure and transport properties of lifbef2 mixtures: Comparison of rigid and polarizable ion potentials. *Journal of Chemical Sciences*, 124(1):261–269, 2012.

[69] Masahiko Matsumiya and Ryuzo Takagi. A molecular dynamics simulation of the electric properties in molten chloride and fluoride quaternary systems. *Electrochimica Acta*, 46(23): 3563–3572, 2001.

[70] Mathieu Salanne, Christian Simon, Pierre Turq, and Paul A. Madden. Heat-transport properties of molten fluorides: Determination from first-principles. *Journal of Fluorine Chemistry*, 130(1):38–44, 2009.

[71] Celine Merlet, Paul A. Madden, and Mathieu Salanne. Internal mobilities and diffusion in an ionic liquid mixture. *Physical Chemistry Chemical Physics*, 12(42):14109–14114, 2010.

[72] Maurice L. Huggins and Joseph E. Mayer. Interatomic distances in crystals of the alkali halides. *The Journal of Chemical Physics*, 1(9):643–646, 1933.

[73] F. G. Fumi and M. P. Tosi. Ionic sizes and born repulsive parameters in the nacl-type alkali halidesi: The huggins-mayer and pauling forms. *Journal of Physics and Chemistry of Solids*, 25(1):31–43, 1964.

[74] M. P. Tosi and F. G. Fumi. Ionic sizes and born repulsive parameters in the nacl-type alkali halidesii: The generalized huggins-mayer form. *Journal of Physics and Chemistry of Solids*, 25(1):45–52, 1964.

[75] Dario Alfe and Michael J. Gillan. First-principles calculation of transport coefficients. *Physical Review Letters*, 81(23):5161–5164, 1998.

[76] H. Z. Fang, W. Y. Wang, Paul D. Jablonski, and Z. K. Liu. Effects of reactive elements on the structure and diffusivity of liquid chromia: An ab initio molecular dynamics study. *Physical Review B*, 85(1):014207, 2012.

[77]

[78] B. B. Karki, D. Bhattarai, and L. Stixrude. A first-principles computational framework for liquid mineral systems. *Cmc-Computers Materials and Continua*, 3(3):107–117, 2006.

[79] Christopher Woodward, Mark Asta, Dallas R. Trinkle, James Lill, and Stefano Angioletti-Uberti. Ab initio simulations of molten ni alloys. *Journal of Applied Physics*, 107(11): 113522–10, 2010.

[80] A. Bengtson, S. Saha, H. O. Nam, R. Sakidja, and D. Morgan. First-principles molecular dynamics modeling of the licl-kcl molten salt system (submitted). *First-principles molecular dynamics modeling of the LiCl-KCl molten salt system (submitted)*, 2013.

[81] A. Klix, A. Suzuki, and T. Terai. Study of tritium migration in liquid li2bef4 with ab initio molecular dynamics. *Fusion Engineering and Design*, 81(17):713–717, 2006.

[82] R. Car and M. Parrinello. Unified approach for molecular-dynamics and density-functional theory. *Physical Review Letters*, 55(22):2471–2474, 1985.

[83] L. Martnez, R. Andrade, E. G. Birgin, and J. M. Martnez. Packmol: A package for building initial configurations for molecular dynamics simulations. *Journal of Computational Chemistry*, 30(13):2157–2164, 2009.

[84] Steve Plimpton. Fast parallel algorithms for short-range molecular dynamics. *Journal of Computational Physics*, 117(1):1–19, 1995.

[85] M. Salanne and P. A. Madden. Polarization effects in ionic solids and melts. *Molecular Physics*, 109(19):2299–2315, 2011.

[86] Bjrn Larsen, Tormod Frland, and Konrad Singer. A monte carlo calculation of thermodynamic properties for the liquid nacl+kcl mixture. *Molecular Physics*, 26(6):1521–1532, 1973.

[87] G. Kresse and J. Hafner. Ab initio molecular dynamics for liquid metals. *Physical Review B*, 47(1):558–561, 1993.

[88] G. Kresse and J. Furthmller. Efficient iterative schemes for ab initio total-energy calculations using a plane-wave basis set. *Physical Review B*, 54(16):11169–11186, 1996.

[89] G. Kresse and D. Joubert. From ultrasoft pseudopotentials to the projector augmented-wave method. *Physical Review B*, 59(3):1758–1775, 1999.

[90] Shuichi Nos. A unified formulation of the constant temperature molecular dynamics methods. *The Journal of Chemical Physics*, 81(1):511–519, 1984.

[91] John P. Perdew, Kieron Burke, and Matthias Ernzerhof. Generalized gradient approximation made simple. *Physical Review Letters*, 77(18):3865–3868, 1996.

[92] John P. Perdew, Kieron Burke, and Matthias Ernzerhof. Generalized gradient approximation made simple [phys. rev. lett. 77, 3865 (1996)]. *Physical Review Letters*, 78(7):1396–1396, 1997.

[93] Jiri Klimes, David R. Bowler, and Angelos Michaelides. Van der waals density functionals applied to solids. *Physical Review B*, 83(19):195131, 2011.

[94] P. E. Blochl. Projector augmented-wave method. *Physical Review B*, 50(24):17953–17979, 1994.

[95] Christos Alexopoulos. A comprehensive review of methods for simulation output analysis, 2006.

[96] Francis Birch. Finite elastic strain of cubic crystals. *Physical Review*, 71(11):809–824, 1947.

[97] F. D. Murnaghan. The compressibility of media under extreme pressures. *Proceedings of the National Academy of Sciences*, 30(9):244–247, 1944.

[98] D.C. Rapaport. *The art of molecular dynamics simulation*. Cambridge University Press, second edition edition, 2004.

[99] John P. Perdew, Adrienn Ruzsinszky, Gbor I. Csonka, Oleg A. Vydrov, Gustavo E. Scuseria, Lucian A. Constantin, Xiaolan Zhou, and Kieron Burke. Restoring the density-gradient expansion for exchange in solids and surfaces. *Physical Review Letters*, 100(13):136406, 2008.

[100] George J. Janz. *Thermodynamic and transport properties for molten salts : correlation equations for critically evaluated density, surface tension, electrical conductance, and viscosity data*. Published by the American Chemical Society and the American Institute of Physics for the National Bureau of Standards, New York, United States., 1988.

[101] V. V. Ignatev, A. V. Merzlyakov, V. G. Subbotin, A. V. Panov, and Yu V. Golovatov. Experimental investigation of the physical properties of salt melts containing sodium and lithium fluorides and beryllium difluoride. *Atomic Energy*, 101(5):822–829, 2006.

[102] Gabor I. Csonka, John P. Perdew, Adrienn Ruzsinszky, Pier H. T. Philipsen, Sebastien Lebegue, Joachim Paier, Oleg A. Vydrov, and Janos G. Angyan. Assessing the performance of recent density functionals for bulk solids. *Physical Review B*, 79(15):155107, 2009.

[103] M.S. Sohal, M.A. Ebner, P. Sabharwall, and P. Sharpe. Engineering database of liquid salt thermophysical and thermochemical properties. Technical report, Idaho National Laboratory, 2010.

[104] Stefan Grimme, Jens Antony, Stephan Ehrlich, and Helge Krieg. A consistent and accurate ab initio parametrization of density functional dispersion correction (dft-d) for the 94 elements h-pu. *The Journal of Chemical Physics*, 132(15):154104–19, 2010.

[105] Stefan Grimme. Accurate description of van der waals complexes by density functional theory including empirical corrections. *Journal of Computational Chemistry*, 25(12):1463–1473, 2004.

[106] Stefan Grimme. Semiempirical gga-type density functional constructed with a long-range dispersion correction. *Journal of Computational Chemistry*, 27(15):1787–1799, 2006.

[107] D.F. Williams and L.M. Toth. Chemical considerations for the selection of the coolant for the advanced high-temperature reactor. Technical report, Oak Ridge National Laboratory, 2005.

[108] Milton D. Grele and Louis Gedeon. *Forced-convection heat-transfer characteristics of molten Flinak flowing in an Inconel X system*. National Advisory Committee for Aeronautics, Washington, DC, 1954.

[109] H. W. Hoffman and L. Jones. Fused salt heat transfer part ii: Forced convection heat transfer in circular tubes containing naf-kf-lif eutectic. Technical report, Oak Ridge National Laboratory Report ORNL-1977, 1955.

[110] D. T. Ingersoll, C. W. Forsberg, and P. E. MacDonald. Trade studies on the liquid-salt-cooled very high-temperature reactor: Fiscal year 2006 progress report. Technical report, Oak Ridge National Laboratory Report ORNL/TM-2006/140, 2007.

[111] B. Vriesema. *Aspects of molten fluorides as heat transfer agents for power generation*. dissertation, 1979.

[112] G. J. Janz and R. P. T. Tomkins. Physical properties data compilations relevant to energy storage: Iv molten salts: Data on additional single and multi-component salt systems. Technical report, National Bureau of Standards Report NSRDS-NBS 61 Part IV, 1981.

[113] J. Garai and A. Laugier. The temperature dependence of the isothermal bulk modulus at 1 bar pressure. *Journal of Applied Physics*, 101(2):023514–4, 2007.

[114] S. Cantor, J.W. Cooke, A.S. Dworkin, G.D. Robbins, R.E. Thoma, and G.M. Watson. Physical properties of molten-salt reactor fuel, coolant, and flush salts. Technical report, Oak Ridge National Laboratory, 1968.

[115] Nobuya Iwamoto, Yoshiaki Tsunawaki, Norimasa Umesaki, Hideo Ohno, and Kazuo Furukawa. Self-diffusion of lithium in molten libef3 and li2bef4. *Journal of the Chemical Society, Faraday Transactions 2: Molecular and Chemical Physics*, 75:1277–1283, 1979.

[116] Toshihiko Ohmichi, Hideo Ohno, and Kazuo Furukawa. Self-diffusion of fluorine in molten dilithium tetrafluoroberyllate. *The Journal of Physical Chemistry*, 80(14):1628–1631, 1976.

[117] Norimasa Umesaki, Nobuya Iwamoto, Yoshiaki Tsunawaki, Hideo Ohno, and Kazuo Furukawa. Self-diffusion of lithium, sodium, potassium and fluorine in a molten lif + naf + kf eutectic mixture. *Journal of the Chemical Society, Faraday Transactions 1: Physical Chemistry in Condensed Phases*, 77(1):169–175, 1981.

[118] G. J. Janz and N. P. Bansal. Molten salts data: Diffusion coefficients in single and multi-component salt systems. *Journal of Physical and Chemical Reference Data*, 11(3):505–693, 1982.

[119] D.F. Williams, L.M. Toth, and K.T. Clarno. Assessment of candidate molten salt coolants for the advanced high-temperature reactor (ahtr). Technical report, Oak Ridge National Laboratory, 2006.

[120] William Humphrey, Andrew Dalke, and Klaus Schulten. Vmd: Visual molecular dynamics. *Journal of Molecular Graphics*, 14(1):33–38, 1996.

[121] D. Olander. Redox condition in molten fluoride salts: Definition and control. *Journal of Nuclear Materials*, 300(23):270–272, 2002.

[122] V. L. Chevrier, S. P. Ong, R. Armiento, M. K. Y. Chan, and G. Ceder. Hybrid density functional calculations of redox potentials and formation energies of transition metal compounds. *Physical Review B*, 82(7):075122, 2010.

[123] Yueh-Lin Lee, Jesper Kleis, Jan Rossmeisl, and Dane Morgan. Ab initio energetics of $labo_3$(001) (b=mn, fe, co, and ni) for solid oxide fuel cell cathodes. *Physical Review B*, 80 (22):224101, 2009.

[124] Hsc chemistry(r) 6.0, 2002.

[125] H. W. Jenkins, G. Mamantov, and D. L. Manning. Electrode potentials of several redox couples in molten fluorides. *Journal of The Electrochemical Society*, 117(2):183–185, 1970.

[126] Henry J. White. Haynes International Capabilities: Hastelloy N Alloy. In *Fluoride Salt-Cooled High Tempearture Reactor Workshop*, Oak Ridge, 2010.

[127] American Society of Mechanical Engineers. Section III Rules for Construction of Nuclear Facility Components - Division 1: Subsection NH - Class 1 Components in Elevated Temperature Service. In *ASME Boiler and Pressure Vessel Code*. 2007.

[128] H. E. McCoy. Status of materials development for molten salt reactors, 1978. URL `http://www.osti.gov/energycitations/product.biblio.jsp?osti_id=5195742`.

[129] American Society of Mechanical Engineers. Section II - Materials: Part D. Properties (Customary): Subpart 1. Stress Tables. In *ASME Boiler and Pressure Vessel Code*. American Society of Mechanical Engineers, 2007.

[130] Haynes International. Hastelloy N Alloy. Technical report, 2002.

[131] M F Simpson, P J Pinhero, M Hara, Y Hatano, R A Anderl, J P Sharpe, T Terai, S Tanaka, D A Petti, and D K Sze. Beryllium Interactions In Molten Flibe Fusion Reactor Materials. In *Twelfth International Conference on Fusion Reactor Materials*, 2006.

[132] Todd Allen, Mark Anderson, Ron Ballinger, Tim Burchell, Edward Blandford, Denis Clark, William Corwin, George Flanagan, Charles Forsberg, Peter Hosmann, David Holcomb, Lin-Wen Hu, John Hunn, Victor Ignatiev, Gordon Kohse, Regis Matzie, Matthew Memmott, Jim Nestell, Michael Patterson, Scott Penfield, Per Peterson, Sam Sham, Lance Snead, Kumar Sridharan, Carl Stoots, Richard Vollmer, David Williams, Dane Wilson, Guoping Cao, Tyler Gerczak, Brian Kelleher, Guiqiu Zheng, David Carpenter, Becky Romatoski, John Dennis Stempien, Anselmo Cisneros, Lakshana Huddar, Raluca Scarlat, and Nicolas Zweibaum. Fluoride-Salt-Cooled High Temperature Reactor (FHR) Materials, Fuels and Components White Paper. 2013.

[133] J Oishi, H Moriyama, S Maeda, and Y Asaoka. Tritium recovery from molten LiF-BeF 2 salt. *Fusion Engineering and Design*, 8:317–321, 1989. URL `http://www.sciencedirect.com/science/article/pii/S0920379689801243`.

[134] P. Calderoni, P. Sharpe, M. Hara, and Y. Oya. Measurement of tritium permeation in flibe (2LiFBeF2). *Fusion Engineering and Design*, 83(7-9):1331–1334, December 2008. ISSN 09203796. doi: 10.1016/j.fusengdes.2008.05.016. URL http://linkinghub.elsevier.com/retrieve/pii/S0920379608000926.

[135] PE Field and JH Shaffer. The solubilities of hydrogen fluoride and deuterium fluoride in molten fluorides. *The Journal of Physical Chemistry*, 56(2):3218–3222, 1967. URL http://pubs.acs.org/doi/pdf/10.1021/j100869a013.

[136] Anthony P. Malinauskas and Donald M. Richardson. The Solubilities of Hydrogen, Deuterium, and Helium in Molten Li2BeF4. *Industrial & Engineering Chemistry Fundamentals*, 13(3):242–245, August 1974. ISSN 0196-4313. doi: 10.1021/i160051a015. URL http://pubs.acs.org/doi/abs/10.1021/i160051a015.

[137] G. M. Watson, R. B. Evans, W. R. Grimes, and N. V. Smith. Solubility of Noble Gases in Molten Fluorides. In LiF-BeF2. *Journal of Chemical & Engineering Data*, 7(2):285–287, April 1962. ISSN 0021-9568. doi: 10.1021/je60013a038. URL http://pubs.acs.org/doi/pdf/10.1021/je60013a038http://pubs.acs.org/cgi-bin/doilookup/?10.1021/je60013a038.